

Cryogenic surface ion traps

Dissertation

zur Erlangung des Doktorgrades an der

Fakultät für Mathematik, Informatik und Physik
der Leopold-Franzens-Universität Innsbruck
vorgelegt von

Dipl. Ing. Michael Niedermayr

durchgeführt am Institut für Experimentalphysik

unter der Leitung von
Univ.-Prof. Dr. Rainer Blatt

July 2015

Abstract

Microfabricated surface traps are a promising architecture to realize a scalable quantum computer based on trapped ions. In principle, hundreds or thousands of surface traps can be located on a single substrate in order to provide large arrays of interacting ions. To this end, trap designs and fabrication methods are required that provide scalable, stable and reproducible ion traps.

This work presents a novel surface-trap design developed for cryogenic applications. Intrinsic silicon is used as the substrate material of the traps. The well-developed microfabrication and structuring methods of silicon are utilized to create simple and reproducible traps. The traps were tested and characterized in a cryogenic setup. Ions could be trapped and their life time and motional heating were investigated. Long ion lifetimes of several hours were observed and the measured heating rates were reproducibly low at around 1 phonon per second at a trap frequency of 1 MHz.

Kurzfassung

Oberflächenfallen bieten eine vielversprechende Fallenarchitektur, um einen skalierbaren Quantencomputer basierend auf Ionenfallen zu realisieren. Ein System aus hunderten oder tausenden Oberflächenfallen kann im Prinzip auf einem einzelnen Substrat angeordnet werden. Dieses System ermöglicht die Arbeit mit einer großen Anzahl von Ionen, die miteinander wechselwirken können. Dazu werden allerdings Fallendesigns und Fertigungsmethoden benötigt, die die Herstellung von skalierbaren, reproduzierbaren und zuverlässig arbeitenden Fallen gewährleisten.

In dieser Arbeit wird ein neuartiges Oberflächenfallendesign präsentiert, das für Tieftemperaturanwendungen entwickelt wurde. Intrinsisches Silizium wird als Substratmaterial für die Fallen verwendet. Die hochentwickelten Mikrofabrikationstechnologien für Silizium werden eingesetzt, um einfache und reproduzierbare Fallen herzustellen. Die Fallen wurden bei tiefen Temperaturen getestet und charakterisiert. Ionen konnten in den Fallen gefangen werden. Dabei wurde eine Verweildauer der Ionen in den Fallen von mehreren Stunden beobachtet. Außerdem wurden die Heizraten der Bewegungsmoden untersucht. Eine niedrige, reproduzierbare Heizrate von ungefähr 1 Phonon pro Sekunde bei einer Fallenfrequenz von 1 MHz wurde gemessen.

Contents

1	Introduction	1
2	Ion trapping fundamentals	5
2.1	Radio-frequency ion traps	5
2.1.1	Operation principle	5
2.1.2	Non-ideal traps	8
2.2	$^{40}\text{Ca}^+$ ion	9
2.3	Laser-ion interaction in a harmonic trap	12
2.4	Cooling and detection	14
2.4.1	Doppler cooling	15
2.4.2	Sideband cooling	16
2.4.3	Detection	16
3	Scalable ion traps	19
3.1	Microtraps	20
3.1.1	Multi-layer traps	21
3.1.2	Surface traps	22
3.2	Motional heating	24
3.2.1	Possible sources	25
3.2.2	Minimizing the heating	26
3.2.3	Heating-rate measurement	27
3.3	Traps in a cryogenic environment	29
3.3.1	Reduced motional heating	31
3.3.2	Vacuum and turnaround time	32
3.3.3	Cryogenic systems	33
4	Experimental setup	35
4.1	Cryogenic system and vacuum chamber	36
4.1.1	Gifford McMahon cryostat	36
4.1.2	Vibration isolation	39
4.1.3	Vacuum chamber	42

4.1.4	Wiring and heater	45
4.1.5	Oven	47
4.1.6	Magnetic fields	48
4.1.7	Cooling down procedure	49
4.2	Trap carrier	50
4.2.1	Trap installation	50
4.2.2	RF Resonator	52
4.2.3	DC Filterboards	53
4.3	Optical setup	54
4.3.1	Lasers systems	54
4.3.2	Ion detection	57
4.4	Experimental control	59
5	Surface trap ‘Yedikule’	63
5.1	Trap geometry	64
5.2	Trap simulations	66
5.2.1	Electrostatic simulations	67
5.2.2	Trapping parameters	68
6	Silica traps	73
6.1	Manufacturing traps	73
6.1.1	Microfabrication	74
6.1.2	Mounting and wire bonding	75
6.2	Trap performance	76
6.2.1	Yedikule-1	76
6.2.2	Yedikule-3	78
7	Silicon traps	81
7.1	Silicon ion traps	81
7.2	Silicon trap design	83
7.3	Manufacturing traps	84
7.3.1	Microfabrication	84
7.3.2	Mounting and wire bonding	88
7.4	RF Resonator performance	89
7.5	Trap performance	91
7.5.1	Trapped ion lifetime	91
7.5.2	Heating rates	91
7.6	Trap improvements	93
7.6.1	Light-induced charging	93
7.6.2	Visions of the future	93

8 Conclusion	97
A Trapping parameters	99
A.1 Multipole expansion	99
B Recipes for trap fabrication	101
B.1 Silica traps	101
B.2 Silicon traps	104

Chapter 1

Introduction

The transistor is a fundamental and ubiquitous building block of modern electronic systems. It is a semiconductor component that can be used as an electric switch. The first patents describing a transistor were independently filed by Julius Edgar Lilienfeld [1] in 1925 and by Oskar Heil [2] 9 years later. The first realization of a transistor was built by John Bardeen and Walter H. Brattain at the Bell Laboratories in 1947 [3].

Transistors based on silicon form the basic component of modern computers. Silicon has several advantages over other semiconductors [4]. Silicon, for example, forms a native oxide which is a good insulator. This oxide can be used to create an isolation layer between the silicon and electrodes required for some types of transistors (field-effect transistor). Furthermore, silicon is the second most common element in the earth's crust (26.3%) which facilitates inexpensive manufacturing. A considerable effort had been made to improve the transistors' fabrication during the last 50 years. In particular, the transistors' physical dimensions have been drastically reduced. On average, the number of transistors per square centimeter in an integrated circuit doubled approximately every two years [5]. In 2014, commercial microprocessors were equipped with transistors with a gate length of 14 nm [6] which corresponds to 26 atomic layers [4]. This fact indicates that the miniaturization of transistors will be limited in the near future simply by the atomic structure of matter. Furthermore, unwanted quantum effects become increasingly relevant with smaller structures [7].

There exists, however, a different approach using a quantum mechanical system instead of transistors to build a completely new type of computer: the quantum computer. The idea was first introduced by Richard Feynman and Paul Benioff in 1982 [8, 9]. While a classical computer based on transistors requires information encoded in distinct values, also called bits (0 and 1), the data in a quantum computer can be any superposition of two states; this is called a quantum bit, or qubit. [10]. In multiple qubit systems the states of the qubits are not necessarily independently defined, but can depend on the states of other qubits. This is known as entanglement. Several quantum algorithms

have been developed which allow mathematical problems to be solved faster. Two of the most famous algorithms are Shor's [11] and Grover's [12] algorithm. Shor's algorithm is an algorithm for integer factorization and runs exponentially faster than its best known classical counterpart. Grover's algorithm is a searching algorithm for an unsorted database and provides a quadratic speed-up compared to the best possible classical algorithm.

Two-level quantum systems that can be used to realize a quantum computer should fulfill some physical requirements. There can be found different formulations of these requirements in the literature [13, 14] and only a brief summary is given here. The system must be scalable physically in order to increase the number of qubits. It must be possible to initialize the state of the system, and read out the state of the system in a qubit specific way. Quantum information is very fragile; the qubits tend to lose their quantum nature and become essentially classical in nature after some characteristic time called the decoherence time. It is important that any logical operations to be performed on the qubits can be done in a time much shorter than this decoherence time. Furthermore, it must be possible to implement a universal set of quantum logic gates. A universal set is the minimum set of gates required to perform any operation possible on a quantum computer. To date a variety of possible candidates of physical quantum systems is under investigation [14]. Among them are solid-state systems such as quantum dots, NV centers, superconducting circuits and nuclear spin systems. Other realizations are based on photons, optically trapped neutral atoms or trapped atomic ions.

Of those systems, trapped ions are one of the preeminent candidates [15]. The ions are confined using a combination of radio-frequency (RF) and static (DC) electric fields due to voltages applied to the electrodes of a so-called ion trap. [16]. The ions' quantum states can be initialized and manipulated by lasers or microwaves. They have been used to demonstrate quantum gates, quantum algorithms and quantum error correction [17]. Importantly, there are no in-principle roadblocks foreseen to scaling ion traps to process hundreds or thousands of quantum bits. However, the technical realization of a such large trapped-ion quantum processor still provides many open challenges.

One promising approach to scaling up ion traps is the use of microfabricated surface traps. In these traps the electrodes providing the electric fields are aligned in one plane. They are usually located on the surface of a substrate material. Hundreds of these traps can be aligned on a single substrate in order to provide arrays of ions which can interact with each other. Typical substrates are dielectrics such as fused silica or sapphire which are used because of their low RF losses. However, the three dimensional structuring of these substrates which is required for more complex trap designs is very difficult. In contrast, there exist well-developed microfabrication and structuring methods for silicon. The high RF losses of silicon at room temperature, though, have limited its application as the substrate of surface traps. The RF losses, however, decrease when the temperature is reduced, and at cryogenic temperatures (<10 K) they are comparable to the losses of

dielectrics.

In this thesis, a novel surface trap design for cryogenic applications based on a silicon substrate is developed and its operation is characterized. The long term goal is to combine ion traps with the sophisticated silicon technologies developed during the last decades.

The thesis is structured as follows. The background information required for this work is covered in chapter 2: A general description of linear radio-frequency ion traps and their working principle are given. To store and manipulate quantum information, certain electronic states and certain motional states of a cold trapped $^{40}\text{Ca}^+$ ion are used which can be manipulated with laser radiation. The atomic properties of $^{40}\text{Ca}^+$ ions are listed, and the interaction of an atom with laser light is discussed in this chapter. Different laser cooling techniques and detection methods of trapped ions are introduced. Chapter 3 starts with a description of different types of microtraps, namely surface traps and multi-layer traps. One key parameter of the traps is the motional heating of the trapped ions, which describes the coupling of the ions with the environment. This heating reduces the quality of the quantum operations performed on the ions and, therefore, should be as small as possible. Unfortunately, the heating increases with reduced trap dimension, which makes quantum operations in microtraps very challenging. Possible sources of the heating and ways to reduce them are given. Methods to measure the heating are listed. In addition, ions in a cryogenic environment and the associated improvements of the trapping performance are discussed. Chapter 4 gives the experimental setup which was designed and built during the course of this work. It includes the vacuum chamber, the optical and electronic setup to trap ions and a cryogenic system which allows the ion traps to be cooled below 10 K. The geometry of the trap electrodes used in the experiments presented in this thesis is given in chapter 5. It is a linear RF surface trap. Its electrode configuration is discussed and simulations of the potential are presented. Ion traps based on silica substrates and their performance are presented in chapter 6. This type of trap is well-known for its good performance [18, 19] and was used to characterize the experimental setup. A novel trap design based on a silicon substrate is introduced in chapter 7. Its design and fabrication are discussed in detail. Furthermore, the trap performance is investigated. In particular, the motional heating of the ions is characterized and found to be very low, both in absolute terms, and relative to typical heating rates observed in other systems. Finally, a summary and a conclusion are given in chapter 8.

Chapter 2

Ion trapping fundamentals

All of the experiments described in this thesis deal with laser cooled $^{40}\text{Ca}^+$ ions confined in a linear Paul trap. This chapter discusses the basic physics of such a situation. Section 2.1 describes ion traps in general and their principles of operation. The energy levels and the optical transitions of $^{40}\text{Ca}^+$ ions are given in section 2.2. The laser-ion interaction is briefly reviewed in section 2.3. Furthermore, basic ion-trapping techniques like cooling and detection are presented in this section.

2.1 Radio-frequency ion traps

The radio-frequency (RF) ion trap or Paul trap was invented by Wolfgang Paul [20, 21]. It provides a way to trap charged particles such as atomic ions using a combination of static (DC) and time-varying (AC) electric fields.

2.1.1 Operation principle

Particles can be, in general, trapped in a three-dimensional harmonic potential. This can be expressed by the following equation

$$U(x, y, z) = \frac{1}{2}(k_x x^2 + k_y y^2 + k_z z^2), \quad (2.1)$$

where k_i is defined as $k_i = \partial_i^2 U$. The associated oscillator frequencies ω_{Ti} of a single trapped particle (e.g. ion) with mass m can be calculated using the formula

$$\omega_{Ti} = \sqrt{\frac{k_i}{m}}. \quad (2.2)$$

Based on eq. (2.1) the following electric potential is necessary for trapping ions with a charge Q in a harmonic trap:

$$\phi(x, y, z) = \frac{U(x, y, z)}{Q} = \frac{1}{2Q}(k_x x^2 + k_y y^2 + k_z z^2). \quad (2.3)$$

However, any electrostatic potential in free space has to satisfy Laplace's equation:

$$\Delta\phi = \frac{1}{2Q}(k_x + k_y + k_z) = 0, \quad (2.4)$$

According to this equation, at least one k_i has to be negative which, in turn, causes an anti-trapping potential in that direction. Consequently, trapping of ions in an electrostatic potential in free space is not possible. A stable trapping potential can be created using an alternating quadrupole potential. A snap-shot of such a potential in two dimensions is shown in fig. 2.1a. This saddle-shaped potential has a trapping component in the y direction and an anti-trapping component in the x direction. If these components are alternating at the right frequency, the ions see a time-averaged potential with trapping components in both directions. This effective potential is thus a pseudopotential and its potential minimum corresponds to the saddle point of the alternating quadrupole potential.

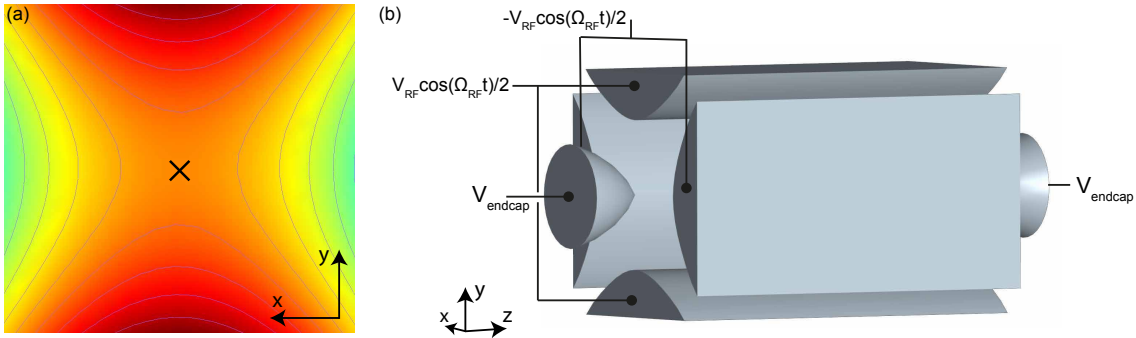


Figure 2.1: (a) Instantaneous electric quadrupole potential in a Paul trap. This saddle-shaped potential alternates at a frequency Ω_{RF} in order to generate the so called pseudopotential. Ions can be trapped at the minimum of the pseudopotential which corresponds to the saddle point of the quadrupole potential (marked). (b) Traditional linear Paul-trap design. To generate a parabolic trapping potential alternating voltages (amplitude $\pm V_{\text{RF}}/2$) are applied to the opposing hyperbolically-shaped electrodes. This provides trapping in the x, y plane. DC voltages applied to the endcap electrodes generate a confinement along the z axis.

It can be generated in the Paul trap as shown in fig. 2.1b. A sinusoidal voltage with an amplitude of $V_{\text{RF}}/2$ is applied to the four hyperbolically-shaped axial electrodes. To produce the quadrupole potential, there is a phase shift of 180° between the two pairs of

2.1 Radio-frequency ion traps

opposing electrodes. The resulting potential can be written as

$$\phi(x, y, z, t) = \frac{V_{\text{RF}}}{2R_0^2}(x^2 - y^2) \cos(\Omega_{\text{RF}}t), \quad (2.5)$$

where $2R_0$ is the closest distance between two opposing trap electrodes. Ω_{RF} is the alternating frequency of the quadrupole potential, also called the trap-drive frequency. Ignoring end effects, the motion of an ion in the quadrupole potential can be described by these differential equations [21]:

$$\ddot{x} - \frac{q\Omega_{\text{RF}}^2}{2} \cos(\Omega_{\text{RF}}t)x = 0 \quad (2.6)$$

$$\ddot{y} + \frac{q\Omega_{\text{RF}}^2}{2} \cos(\Omega_{\text{RF}}t)y = 0 \quad (2.7)$$

$$\ddot{z} = 0. \quad (2.8)$$

These are a special form of Mathieu's differential equation. q is called the stability parameter and is defined by

$$q = \frac{2QV_{\text{RF}}}{mR_0^2\Omega_{\text{RF}}^2}. \quad (2.9)$$

It can be shown that stable trapping in the x and y direction is possible for $0 < q < 0.908$ assuming no additional DC fields are applied to the axial electrodes [22]. In this case the trajectories can be decomposed into two different oscillations.

The frequency of the first oscillation is equal to the trap drive frequency, Ω_{RF} . The associated motion (micromotion) is typically unwanted because it causes atomic level shifts and reduces the laser cooling efficiency [23]. It is smallest when the ion is located at the RF saddle point (pseudopotential minimum), where the electric RF field is zero. Stray fields can push the ion off this point and increase the micromotion. Therefore, compensation voltages are usually applied with the aim to offset the stray fields and minimize the micromotion. This is called micromotion compensation. Exactly how it is implemented is discussed in section 5.2.2.

The second oscillation is lower in frequency and typically larger in amplitude. It is called secular motion and its frequency is (assuming $q^2 \ll 1$)

$$\omega_{\text{T}_{x,y}} = \frac{q\Omega_{\text{RF}}}{2\sqrt{2}}. \quad (2.10)$$

The secular motion can be understood as the motion of a particle trapped in the pseudopotential (pseudopotential approximation), which is given by

$$U_{\text{Pseudo}}(x, y, z) = \frac{Q^2}{4m\Omega_{\text{RF}}^2} |\nabla\phi_{\text{eff}}(x, y, z)|^2. \quad (2.11)$$

$\phi_{\text{eff}}(x, y, z)$ corresponds to the potential $\phi(x, y, z, t)$ with maximum amplitude [i.e. where $\cos(\Omega_{\text{RF}}t) = 1$]. Considering the potential in the Paul trap given by eq. (2.5), the corresponding pseudopotential is

$$U_{\text{Pseudo}}(x, y, z) = \frac{1}{2} \frac{Q^2 V_{\text{RF}}^2}{2m\Omega_{\text{RF}}^2 R_0^4} (x^2 + y^2). \quad (2.12)$$

This represents a stable harmonic trapping potential in two direction (x and y axes, or radial axes). Trapping in the third direction along the z axis (axial direction) can be accomplished by applying a DC voltage to the two endcap electrodes (see 2.1b) which creates a harmonic potential in the z direction. The endcap voltage is usually chosen in a way that the corresponding axial trap frequency is smaller than the radial trap frequencies, $\omega_{\text{Tz}} < \omega_{\text{Tx}}, \omega_{\text{Ty}}$. This enables chains of ions to be trapped aligned along the axial direction.

In a traditional trap used for trapping atomic ions (e.g. [24]) the typical distance between the center of the trap and the electrodes, R_0 , is about 0.5 – 1 mm. The amplitude of the alternating voltage, V_{RF} , and frequency, Ω_{RF} , are about 1 kV and 10-100 MHz, respectively. These frequencies are part of the radio frequency (RF) band. Therefore, the drive frequency and amplitude are called RF frequency and RF voltage, respectively.

Typically, an RF voltage of V_{RF} is only applied to one electrode pair, whereas the second pair is kept at ground instead of applying $\pm V_{\text{RF}}/2$ to both pairs. On the one hand, this simplifies the experimental setup since only one RF source is necessary and no phase lock is required. On the other hand, the working principle of the trap does not change.

2.1.2 Non-ideal traps

The hyperbolically-shaped electrodes in the traditional Paul trap make sure that the entire electric potential inside the trap corresponds to a well-defined quadrupole potential described by eq. (2.5). This potential forms the harmonic pseudopotential with a minimum in the center for trapping [see eq. (2.12)]. However, the trapping potential does not need to be harmonic over the entire volume enclosed by the electrodes. As the ion is generally confined to within a few microns of the trap axis, the potential only needs to be harmonic (to a good approximation) over a small region where the ions are situated. The idealized hyperbolic geometry can be significantly deformed while maintaining a harmonic potential minimum at the trap center. The operation of a generalized non-hyperbolic trap is discussed here, while the details of the kinds of deformations used in practice are discussed in chapter 3.

The physics and equations given in section 2.1.1 can be used to describe the non-hyperbolic trap as well. For the same applied voltage, however, the harmonic term of the potential generated by this trap is smaller than that in a hyperbolic trap of similar dimensions. Therefore, an additional efficiency parameter (ϵ) must be added to accommodate that. The parameter can be understood to describe how much of the applied voltage V_{RF}

2.2 $^{40}\text{Ca}^+$ ion

is contributing to the harmonic component of the potential and how much is going into higher order terms. ϵ is 1 for a hyperbolic trap by definition and $0 < \epsilon < 1$ for most other trap configurations. For surface traps the efficiency parameter is typically around 0.2 – 0.3. To take this into account, the potential used in eq. (2.11) is modified to

$$\phi'_{\text{eff}}(x, y, z) = \epsilon \phi_{\text{eff}}(x, y, z). \quad (2.13)$$

Furthermore, the stability parameter, q' , of a non-hyperbolic trap is

$$q' = \epsilon q. \quad (2.14)$$

As mentioned before, for a stable trap operation it is essential to run the trap within a certain range of q' values. Hence, it is useful to determine ϵ beforehand. Because there is not a general analytical solution for ϵ in an arbitrary trap geometry, ϵ is often calculated using numerical simulations (see section 5.2). From the simulations, the trap frequencies ω'_{Ti} can be retrieved. Comparing them with the trap frequencies of the hyperbolic trap (ω_{Ti}) allows the determination of ϵ in the pseudopotential approximation:

$$\epsilon_i = \frac{\omega'_{Ti}}{\omega_{Ti}} = \omega'_{Ti} \frac{m \Omega_{\text{RF}} R_0^2 \sqrt{2}}{Q V_{\text{RF}}}. \quad (2.15)$$

Here, eq. (2.10) was used to rewrite ω_{Ti} .

It should be noted that R_0 of a hyperbolic trap is explicitly defined as the shortest distance between the trap center and the electrodes [see eq. (2.5)]. Due to the symmetry of this trap design the geometric center of the trap is also the minimum of the trapping potential, and the shortest distance between the center and every electrode is the same for all four axial electrodes. That does not hold for an arbitrary trap configuration: the shortest distance can be different for different electrodes. Therefore, R_0 should be understood as the shortest distance between the trapped ions and the nearest trap electrode. This means that ϵ defined in eq. (2.15) compares an arbitrary trap to a hyperbolic trap with the same minimum ion-electrode distance.

2.2 $^{40}\text{Ca}^+$ ion

Different atom species can be used in quantum computing experiments [25]. There are, however, several requirements that have to be considered. The atoms should be stable and have a relatively simple energy-level structure when ionized, which includes a metastable state that can be used together with the ground state to encode a quantum state (electronic qubit). The relevant atomic transitions should be in or near the optical range and a laser system must be available to address them. The traps presented in this work are operated with $^{40}\text{Ca}^+$ ions. ^{40}Ca is a stable alkaline earth metal. If singly ionized, these atoms

have only one valence electron and, therefore, a simple energy level structure similar to hydrogen. All relevant energy transitions are between 390 nm and 870 nm, and commercial diode laser systems are available to drive them. The lowest energy levels are depicted in fig. 2.2.

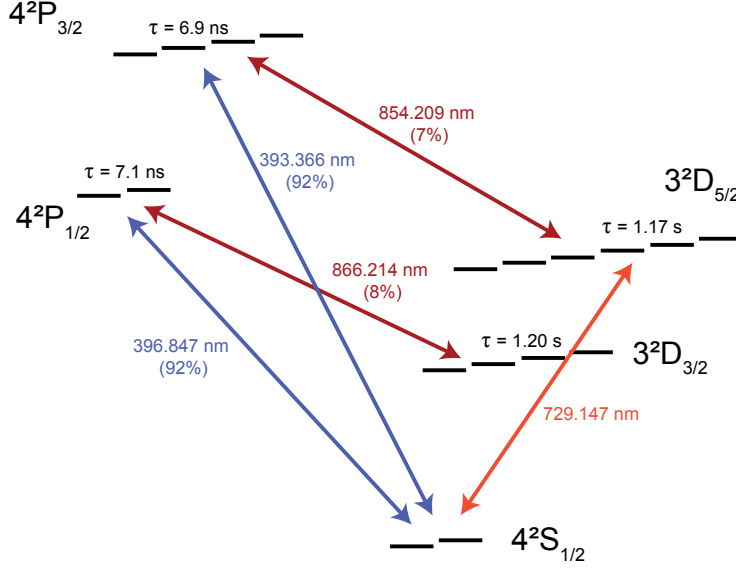


Figure 2.2: The lowest energy levels of the $^{40}\text{Ca}^+$ ion including the Zeeman sublevels. The transition wavelengths, the branching ratios and the natural life times of the excited states, τ , are stated [26–28]. The dipole transition at 397 nm is used for Doppler cooling and state detection. To empty the meta-stable D states repumping lasers at 866 nm and 854 nm can be applied. The quadrupole transition at 729 nm is used for ground-state cooling, heating-rate measurements and encoding the electronic qubit.

At first, only the basic transitions of $^{40}\text{Ca}^+$ are considered, ignoring Zeeman sublevels. The $4^2\text{S}_{1/2}$ state is the electronic ground state of the $^{40}\text{Ca}^+$ ion. The next higher levels are two D-levels ($3^2\text{D}_{3/2}$, $3^2\text{D}_{5/2}$) which are energetically separated due to spin-orbit coupling. The S-D transition is a quadrupole transition and electric-dipole forbidden. The D states have a long life time of about 1 s and are called metastable for that reason. The $\text{S}_{1/2}$ and the $\text{D}_{5/2}$ states are used to encode the electronic qubit. In this context they are also referred to as $|S\rangle$ and $|D\rangle$, respectively. Strong laser light at 729 nm can be used to drive the transition.

$4^2\text{P}_{1/2}$ and $4^2\text{P}_{3/2}$ are the next higher levels. There exist dipole transitions to the 4S and 3D states. The life times of the P state are a few ns. The $4^2\text{S}_{1/2} - 4^2\text{P}_{1/2}$ transition, with a linewidth of 22.4 MHz, can be driven with a laser at 397 nm and is used for Doppler cooling and state detection (see section 2.4). The valence electron can also decay from the $4^2\text{P}_{1/2}$ state to the metastable $3^2\text{D}_{3/2}$ state with a probability of 7.5%. Therefore, a repumping laser at 866 nm is required during Doppler cooling and state detection in order

to suppress the population of the D state. A second repumping laser at 854 nm is used for the state initialization of the electronic qubit. It pumps the population from $3^2\text{D}_{5/2}$ to $4^2\text{P}_{1/2}$ from where it rapidly decays to the ground state.

Having discussed the gross structure above, the following section considers the effect of the Zeeman sublevels. In the absence of an externally applied magnetic field the Zeeman levels are degenerate. To lift this degeneracy in the experiments a magnetic field of several Gauss is applied. This leads to a splitting of 1.68 MHz/G between each of the $3^2\text{D}_{5/2}$ levels and a splitting of 2.80 MHz/G between the $4^2\text{S}_{1/2}$ levels [29]. Due to this Zeeman splitting, there are 10 transitions between the states $4^2\text{S}_{1/2}$ and $3^2\text{D}_{5/2}$, as shown in fig. 2.3.

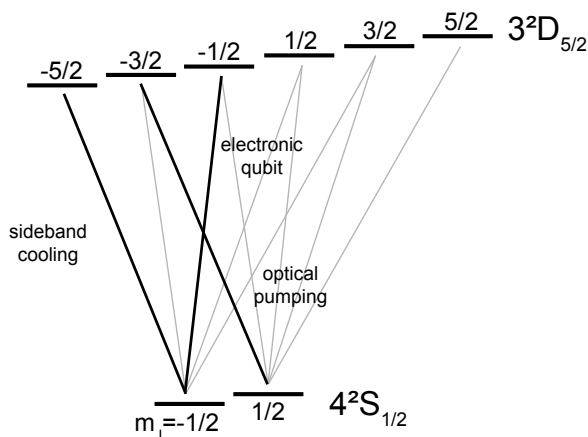


Figure 2.3: Zeeman sublevels of the states $4^2\text{S}_{1/2}$ and $3^2\text{D}_{5/2}$ and the possible quadrupole transitions. The single transitions can be individually addressed by tuning the wavelength and polarisation of the 729 nm laser. Three transitions are highlighted which are used for different procedures during the ion trapping experiments presented in this thesis. Further details on these procedures can be found in the main text.

Three of the transitions are used for special purposes in this work:

- **Sideband cooling**

The transition $\text{S}_{1/2}(m_J=-1/2) \rightarrow \text{D}_{5/2}(m_J=-5/2)$ is employed in the sideband-cooling procedure (see section 2.4.2).

- **Electronic qubit**

The transition $\text{S}_{1/2}(m_J=-1/2) \rightarrow \text{D}_{5/2}(m_J=-1/2)$ is often used to encode the electronic qubit $|S\rangle \rightarrow |D\rangle$ because it is less sensitive to magnetic field fluctuation than other transitions¹. In this work, the motional heating of the ions is measured with this transition (see section 3.2.3).

- **Optical pumping**

To perform sideband cooling and heating rate measurements on the transitions cho-

¹The same is true for the transition $\text{S}_{1/2}(m_J=1/2) \rightarrow \text{D}_{5/2}(m_J=1/2)$.

sen above requires the ion to be in initial state $S_{1/2}(m_J=-1/2)$. This can be achieved by the so-called optical pumping. Thereby, the transition $S_{1/2}(m_J=1/2)-D_{5/2}(m_J=-3/2)$ is used in combination with the repumping laser at 854 nm in order to collect the population of the $S_{1/2}(m_J=-1/2)$ state.

2.3 Laser-ion interaction in a harmonic trap

The quantum mechanical behavior of an ion in a Paul trap is briefly considered in this section. The detailed description is given elsewhere [30]. The ion is treated as a two-level system with ground state $|S\rangle$ and excited state $|D\rangle$, which were already introduced as the electronic qubit states in section 2.2. The energy difference between those states is $\hbar\omega_e$. The ion is trapped in a harmonic potential with trapping frequency ω_T (see section 2.1.1). This is described by the quantum harmonic oscillator. The motion of the ion is quantized with the energy levels $\hbar\omega_T(n+1/2)$, where n indicates the phonon number. The corresponding quantum states are referred to as $|n\rangle$. Because multiple ions in a trap share the same motion, the phonons can be used as a quantum bus to connect the electronic states of different ions. Furthermore, the ion can interact with a laser beam of frequency ω_L . The laser can be either in resonance with the electronic qubit transition or detuned by $\Delta = \omega_L - \omega_e$. It can drive the transition between the two states of the electronic qubit. Depending on the detuning it can also couple the electronic qubit with the motional states of the ion in the trap ($\Delta = \pm\omega_T$).

The total Hamiltonian, H , of this system consists of a time-independent and a time-dependent part. The time-independent part, H_0 , describes the electronic two-level system, H_e , and the ion's motion in the harmonic potential, H_m . The interaction of the ion with the laser H_i corresponds to the time-dependent part:

$$H = H_0 + H_i = H_m + H_e + H_i. \quad (2.16)$$

The Hamiltonian, H_e , of the electronic state can be written as

$$H_e = \hbar\frac{\omega_e}{2}(|S\rangle\langle S| - |D\rangle\langle D|). \quad (2.17)$$

However, it proves beneficial to represent this Hamiltonian in the spin-1/2 algebra using the Pauli spin matrices:

$$H_e = \hbar\frac{\omega_e}{2}\sigma_z. \quad (2.18)$$

The motional Hamiltonian, H_m , can be stated as the sum of the kinetic and potential energy of a harmonic oscillator where the displacement, x , and the momentum, p , are

2.3 Laser-ion interaction in a harmonic trap

replaced by the operators \hat{x} and \hat{p} , respectively:

$$H_m = \frac{\hat{p}^2}{2m} + \frac{m\omega_T^2 \hat{x}^2}{2}. \quad (2.19)$$

It proves again to be useful to rewrite the Hamiltonian. Using the creation and annihilation operators a and a^\dagger eq. (2.19) is modified to

$$H_m = \hbar\omega_T(a^\dagger a + \frac{1}{2}), \quad (2.20)$$

where $a = \sqrt{m\omega_T/(2\hbar)}(\hat{x} + \hat{p} \cdot i/(m\omega_T))$ and $a^\dagger = \sqrt{m\omega_T/(2\hbar)}(\hat{x} - \hat{p} \cdot i/(m\omega_T))$. The interaction term for one dimension can be written as

$$H_I = \frac{1}{2}\hbar\Omega(\sigma^+ + \sigma^-)(e^{i(kx - \omega_L t + \phi)} + e^{-i(kx - \omega_L t + \phi)}). \quad (2.21)$$

where $\sigma^\pm = (\sigma_x \pm i\sigma_y)/2$. In this case the laser beam is aligned parallel to the x axis of the trap and k is its wave number. Ω is the Rabi frequency which is associated with the coupling strength between the ion and the light field. For a better understanding of the interaction, a transformation from the Schrödinger picture into the interaction picture is performed by applying the interaction Hamiltonian, $H_I = U^\dagger H_i U$, where $U = e^{-iH_0/\hbar}$. Furthermore, H_I can be simplified using the so-called rotating-wave approximation²:

$$H_I = \frac{1}{2}\hbar\Omega(\sigma^+ e^{i\eta(\tilde{a} + \tilde{a}^\dagger)} e^{-i\Delta t} + \sigma^- e^{-i\eta(\tilde{a} + \tilde{a}^\dagger)} e^{i\Delta t}). \quad (2.22)$$

In this equation $\tilde{a} = a e^{-i\omega_T t}$ was used and the Lamb-Dicke parameter, η , was introduced

$$\eta = kx_0 = k\sqrt{\frac{\hbar}{2m\omega_T}}, \quad (2.23)$$

where x_0 corresponds to the extension of the wave function of the trapped ion in the ground state. Eq. (2.22) states that the electronic ground state $|S\rangle$ and the motional state $|n\rangle$ can be coupled with the excited state $|D\rangle$ and a different motional state $|m\rangle$ ($|S, n\rangle \leftrightarrow |D, m\rangle$). In the ion's rest frame it can also be understood that the laser frequency ω_L is modulated with the trap frequency, ω_T . By changing the detuning, Δ , the modes which are coupled can be selected. For example if $\Delta \approx (m-n)\omega_T$ the states $|S, n\rangle$ and $|D, m\rangle$ will be coupled. Depending on the detuning the following cases can be distinguished (see fig. 2.4). If $m > n$ ($m < n$) the transition is called a blue (red) sideband transition. If the motional state does not change ($n = m$) the transition is referred to as a carrier transition.

The coupling strength of the different transitions can be described by their Rabi fre-

²This means that the fast-oscillating terms are neglected since they have very small influence on the time evolution.

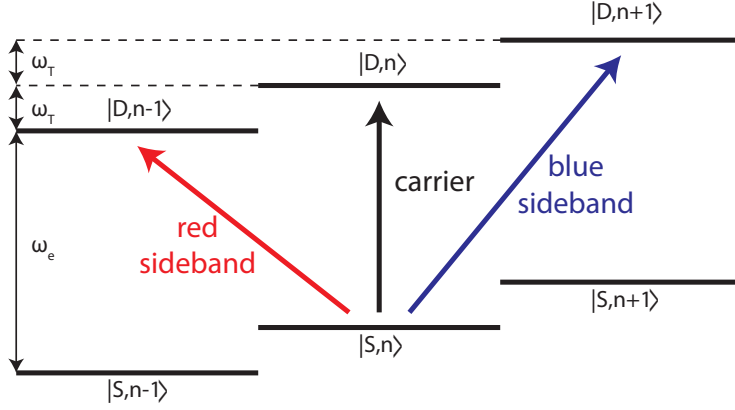


Figure 2.4: Carrier and first-order sidebands of the quadrupole transition. The motion of the ion in the harmonic trap (frequency ω_T) modulates the atomic transition (frequency ω_e) and introduces sidebands. Driving the red sideband reduces the phonon number by one and driving the blue sideband increases it by one. The carrier leaves the phonon number unchanged.

quencies [29]

$$\Omega_{n,m} = \Omega_{m,n} = \Omega_0 |\langle n | e^{in(\hat{a} + \hat{a}^\dagger)} | m \rangle|. \quad (2.24)$$

This expression can be further simplified if the ions are cooled into the Lamb-Dicke regime [$\eta^2(2n+1) \ll 1$]. In this limit the probability of higher order transitions ($|n-m| > 1$) is small and can be neglected. The Rabi frequency of the carrier transition can then be written as

$$\Omega_{\text{car}} = \Omega_{n,n} = \Omega_0(1 - \eta^2 n) \quad (2.25)$$

with the coupling weakly depending on the motional state of the ion. The coupling strength of the first red and blue sideband are

$$\Omega_{\text{red}} = \Omega_{n,n-1} = \Omega_0 \eta \sqrt{n} \quad (2.26)$$

$$\Omega_{\text{blue}} = \Omega_{n,n+1} = \Omega_0 \eta \sqrt{n+1}. \quad (2.27)$$

The Rabi frequencies of these two sidebands vary as a function of the phonon number. This effect can be used to measure the phonon number and the motional heating rate of the trapped ions (see section 3.2).

2.4 Cooling and detection

To measure the heating rate of the trapped ions, the motional sideband spectroscopy method [31] is used in this work which is discussed in detail in section 3.2.3. It basically consists of three steps. First, the ion is cooled. The cooling is switched off and the ion can heat up for a certain time (waiting time). In the last step, the motional sidebands on

2.4 Cooling and detection

the quadrupole transition are investigated in order to retrieve the current phonon number [compare eq. (2.26) and eq. (2.27)]. By varying the waiting time, the heating rate can be determined.

Using motional sideband spectroscopy, the phonon number can be measured with a high resolution (< 0.1 phonons). This, however, requires the ion to be cooled close to its motional groundstate (see section 3.2.3) which can be achieved by combining two laser cooling methods: Doppler cooling [30] and sideband cooling [30, 31]. Both methods are briefly discussed below. First, the ion is cooled down in to the Lamb-Dicke regime by Doppler cooling. Further cooling to the ground state can be accomplished by sideband cooling. Both methods are, in principle, similar but use different atomic transitions. The natural linewidth of the transition used for Doppler cooling is much larger than the trap frequency ($\Gamma \gg \omega_T$). This is called unresolved-sideband or weak-binding regime. For sideband cooling, the linewidth is much smaller than the trap frequency ($\Gamma \ll \omega_T$), and it is called resolved-sideband or strong-binding regime. Both methods are briefly described in this section.

The S-P transition (see section 2.2) which is used for Doppler cooling also provides a way to image the ions and detect their state. Therefore, the fluorescence light created when driving this transition is detected. This procedure is presented in this section too. A detailed description about the cooling methods and the state detection can be found in the PhD thesis of C. Ross [29].

2.4.1 Doppler cooling

In the weak-binding regime the ion can absorb and emit many photons during one oscillation in the harmonic trapping potential. Thereby, its velocity alternates periodically causing a time-dependent Doppler shift. The rate at which the ion scatters photons depends directly on this time-dependent Doppler shift which means that the scattering rate is also velocity-dependent and oscillates in time. The momentum transfer from the photon to the ion during absorption is always in the direction of the laser beam. The emission, however, is in a random direction and its momentum transfer averages out over time. These two effects combined can be understood as a velocity-dependent radiation pressure which cools the ion for red-detuned light and heats it for blue-detuned light. Due to momentum transfer during photon absorption and emission the ion performs a random walk in momentum space, which limits its minimum momentum achieved by Doppler cooling (Doppler limit). The minimum energy in the Doppler limit which is reached for a detuning $\Delta = -\Gamma/2$, is [32]

$$E_D = \frac{\hbar\Gamma}{2}. \quad (2.28)$$

The corresponding mean phonon number of the trapped ion is

$$n_{\min} \approx \frac{\Gamma}{2\omega_T}. \quad (2.29)$$

The optical transition used for Doppler cooling $^{40}\text{Ca}^+$ ions is the $S_{1/2}$ – $P_{1/2}$ transition with a natural linewidth of 22.4 MHz (see fig. 2.2). For typical trapping parameters ($\omega_T = 2\pi \times 1$ MHz, Lamb-Dicke parameter $\eta = 0.07$), the mean phonon number in the Doppler limit is ~ 11 and the Lamb-Dicke regime $\eta^2(2n+1) \ll 1$ can be reached.

To Doppler-cool the motion along all three principal axes of the trap, the laser beam must have a component parallel to each axis. Some trap geometries restrict optical access from certain directions such that this condition is not necessarily easy to meet. Especially in surface ion traps, some modifications may be necessary to enable a proper cooling along the direction of all principal axis. Such modifications are discussed in detail in section 3.1.2.

2.4.2 Sideband cooling

Further cooling beyond the Doppler limit can be achieved by sideband cooling. The quadrupole transition, $S_{1/2}$ – $D_{5/2}$, at 729 nm is used for that. The natural linewidth of this transition (< 1 Hz) is much smaller than the trap frequencies and, therefore, allows frequency resolved addressing of the motional sidebands. The sideband cooling procedure is depicted in fig. 2.5. The cooling laser is red-detuned by $\Delta = -\omega_{T_1}$ to couple the states $|S, n\rangle \leftrightarrow |D, n-1\rangle$ as shown in fig. 2.4. Thereby, the phonon number of the motional state is reduced by one each time the ion is pumped in the $D_{5/2}$ state.

In order to achieve a reasonably high cooling rate, it is necessary to shorten the long lifetime of the metastable D state (~ 1 s). This can be achieved by using laser light at 854 nm which couples the $D_{5/2}$ state to the short living $P_{3/2}$ state. The P state decays predominantly to the S state without changing the phonon number (see fig. 2.2). If $|n=0\rangle$ is reached the coupling strength on the red sideband turns zero and the ion settles in the motional ground state.

2.4.3 Detection

To image the ion in the trap a photomultiplier tube (PMT) and a CCD camera are used. They collect the photons scattered by the ion when the $S_{1/2}$ – $P_{1/2}$ transition is driven by the 397 nm laser. Due to the short life time of the $P_{3/2}$ state photons are scattered at a sufficiently high rate to allow a fast detection of the ion (\sim ms).

This setup is also used to retrieve probabilities of occupancy of the S and D states (electron shelving technique). The S state scatters photons via the S-P transition when illuminated with the detection laser. The D states, however, remains dark. This enables

2.4 Cooling and detection

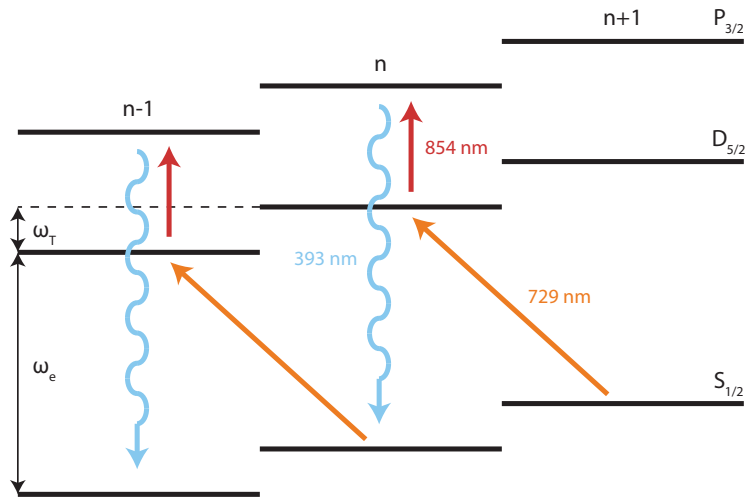


Figure 2.5: Sideband cooling scheme. The laser at 729 nm is detuned to the red sideband coupling $|S, n\rangle$ and $|D, n-1\rangle$. The phonon number is reduced by one every time the ion is pumped into the D state. A repumping laser at 854 nm quenches the life time of the D state by pumping the ion in the P state from where it rapidly decays to the S state. The phonon number is conserved with high probability during this decay in the Lamb-Dicke regime.

state discrimination close to 100% [31]. Repeating the state detection measurement many times on the identically prepared state allows then the reconstruction of the occupation probabilities.

The state detection provides a simple way to read out the state of the electronic qubit defined in section 2.2. It is also utilized for spectroscopy measurements on the quadrupole transition such as motional sideband spectroscopy used to determine the heating rate (see section 3.2.3).

Chapter 3

Scalable ion traps

Ion traps have already been used to demonstrate, in principle, all components necessary for building a quantum computer [17, 33, 34]. This, however, has so far been limited to not more than a few ten ions [35, 36]. To put this number into context, the simulation of quantum systems on a classical computer should be considered. To date, the largest quantum computation system with 42 qubits was simulated on the supercomputer “Jugene” using 262144 CPUs [37]. To create more than 42 qubits and outperform a supercomputer, an ion-based quantum computer only needs 100-1000 well controlled ions. This takes into account that multiple physical qubits (ions) are used for one logical qubit in order to enable quantum error correction.

There exist different approaches to scale ion trapping systems to accommodate hundreds or thousand of individually controllable ions. The most prominent are listed here:

- **Segmented trap/shuttling** - Several linear traps grouped on a single chip form quantum registers. They are linked by shuttling one or more ions from one trap to the next. The shuttling is accomplished by segmenting the DC electrodes and varying the voltages applied to them. This allows quantum communication between the different registers [38, 39].
- **Segmented trap/no shuttling** - Long chains of ions with uniform spacing are trapped in a segmented trap. Transverse phonon modes are used to realize quantum gate operations without the need for single-mode resolution [40, 41].
- **Trap arrays/nearest-neighbor interaction** - An array of individual traps is created on a chip. The distances between the adjacent trapping sites are chosen to be small enough to offer adequate coupling between the individual ions. This enables a nearest-neighbor quantum interaction [42, 43]. The basic scheme has already been demonstrated in a 1D array [44], and there are attempts to generalize it to 2D arrays [45, 122].

- **Modular ion trap quantum-computer** - Individual ion traps form single registers, and they are connected with each other via photonic interfaces. In contrast to the other schemes, it is not necessary that the individual trap registers are located next to each other (on the same chip or carrier) [46].

The work in this thesis is directed at segmented traps. It may, however, be noted that several aspects of the work could find application in the other approaches. These connections will be highlighted in the relevant sections.

To realize the segmented-trap architectures different trap designs can be used. Due to the fact that a large number of segmented electrodes is needed, the trap features such as electrode width have to be chosen to be rather small (< 1 mm). Such traps are typically referred to as microtraps, however, there exists no general definition. Different types of microtrap designs are presented in section 3.1. As the traps are miniaturized - with the electrodes being moved closer to the ion - the ions are increasingly perturbed by sources of noise related to the electrodes' proximity. This causes an increased motional heating which is discussed in section 3.2. The increased heating caused by smaller trap sizes can be offset by reducing the temperature of the trap. Indeed, operation of traps at liquid helium temperatures brings a number of advantages, each of which is discussed in section 3.3.

3.1 Microtraps

In general, microtraps can be divided in multi-layer traps and surface traps. A comparison of the different electrode configurations is shown in fig. 3.1. The pseudo-potentials created by these traps are illustrated in fig. 3.2. The different types of traps are discussed in this section.

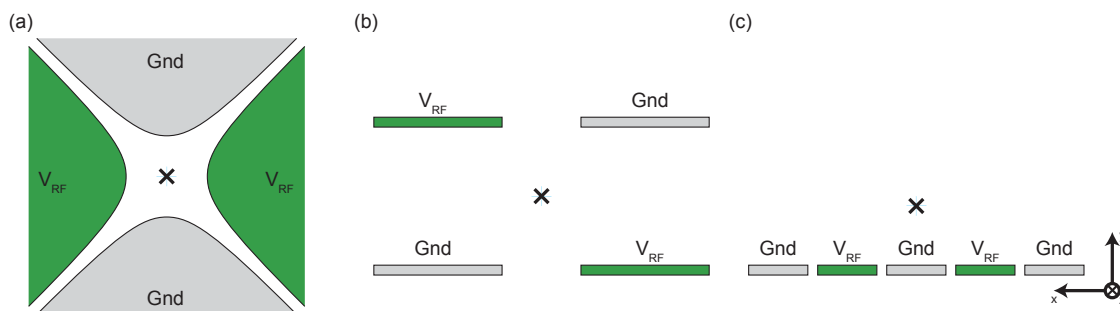


Figure 3.1: Cross-section of different electrode configurations perpendicular to the trap axis. To create a radial trapping potential, RF-voltage is applied to the green electrodes while the gray electrodes are kept at ground. The crosses indicate the trapping position. (a) Hyperbolic trap, (b) two-layer trap and (c) surface trap.

3.1 Microtraps

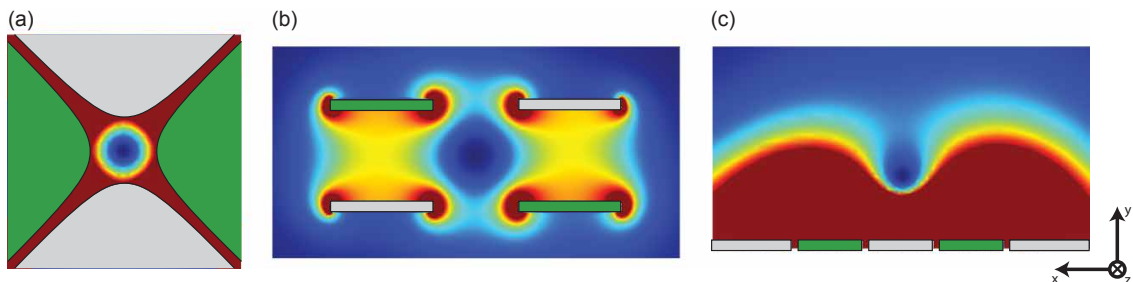


Figure 3.2: Simulated pseudopotential in a plane perpendicular to the trap axis created by the different electrode configurations in fig. 3.1. The potentials were simulated in COMSOL 3.4 (see section 5.2).

3.1.1 Multi-layer traps

Multi-layer traps consist of several electrode layers which are stacked (see fig. 3.1b, fig. 3.2b). Typically, two [47–49] or three layer [50] configurations are used. In the two-layer design RF voltages are applied to two diagonally opposite electrodes, while holding the other electrode pair at RF ground (see fig. 3.1b). This creates a pseudopotential minimum parallel to the RF-electrodes (i.e. parallel to the z -direction), and at the geometric center of the trap in the x - y plane.

The DC electrodes which are held at RF-ground (colored gray in fig. 3.3) are segmented, and a different DC voltage can be applied to each segment. By this means an axially confining potential can be generated. If sufficiently many segments are available, multiple local axial minima can be created. These can be used to independently trap multiple ions or ion strings. Varying the potential applied to the DC electrodes changes the positions of the minima (and so the positions of the trapped ions). This allows shuttling of individual ions or ion strings along the trap axis.

There exist different ways to build multi-layer traps [51]. A very simple and basic method is stacking layers of copper and Kapton stripes [52]. The assembly of the strips has to be done manually and all electrodes have to be individually aligned which makes it time-consuming and limits the alignment precision. Another method is using gold-plated alumina wafers [48, 49]. Gold is partially removed by laser cutting in order to create the individual electrodes on the wafers. Thereby, a more precise alignment of the electrodes on a wafer can be achieved. However, to build a multi-layer trap, several wafers have to be stuck together which is still done by hand. To create a monolithic trap which requires no manual assembly steps, technologies from the semiconductor industry are adopted [53, 54]. This includes optical lithography, plasma etching and physical vapor deposition which enable a sub- μm -resolution.

Different operations which are necessary for a quantum computer based on the shuttling architecture could be already implemented in multi-layer traps. For example, shuttling along a linear trap and through junctions has been shown [50, 55]. Additionally,

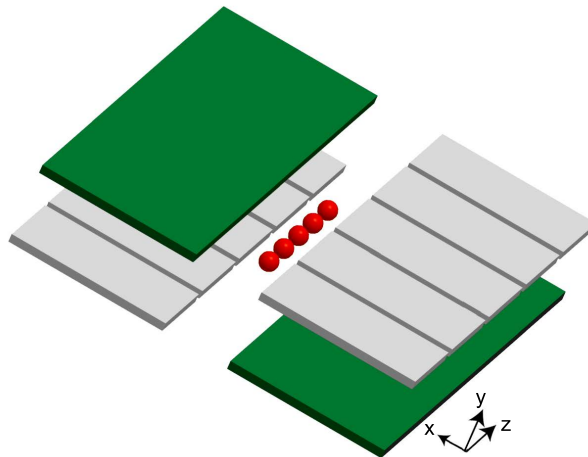


Figure 3.3: Two-layer configuration. RF-voltage is applied to the green electrodes, while the gray electrodes are held at RF ground. This creates a radially (x, y) confining potential along the geometrical center of the trap. The gray electrodes are segmented and DC voltages can be applied to them which enables the generation of a confining potential along the axial (z) direction. The minimum of the confining potential can be shifted along the axial direction by changing the applied DC voltages. This enables axial shuttling of the trapped ions as well as splitting and combining of the ion strings.

splitting and combining of strings has been demonstrated [56]. Each of these operations is possible with the shuttling of the ions causing very little additional motional heating.

3.1.2 Surface traps

In a surface ion trap all DC and RF electrodes are aligned in one plane [18, 47]. The trapping position is located above the surface as depicted in fig. 3.1c. A typical realization of a linear surface trap is shown in fig. 3.4. Two RF stripe electrodes are arranged parallel to an interjacent center electrode on top of a substrate. Segmented electrodes are located on each side of the two RF electrodes. Applying an RF voltage to the RF electrodes while all other electrodes are RF-grounded generates the pseudopotential to trap ions radially (see fig. 3.2c). Similar to the multi-layer traps, DC voltages are applied to the segmented electrodes in order to create confinement along the axial direction. A DC voltage can also be applied to the center electrode which is usually used for micromotion compensation.

The first surface ion trap was tested by Seidelin and co-workers at NIST in 2006 [18]. By means of photolithography, gold structures were created on a quartz substrate in order to form the trap electrodes. Since then, a huge variety of surface traps has been built. In an effort to improve the performance of the traps the materials used were varied. For example, sapphire substrates [57] and superconducting electrodes [58] were tested¹. In addition, attempts were made to combine the trap fabrication with the well established

¹However, no significantly improved trap performance could be observed for trap using these materials.

3.1 Microtraps

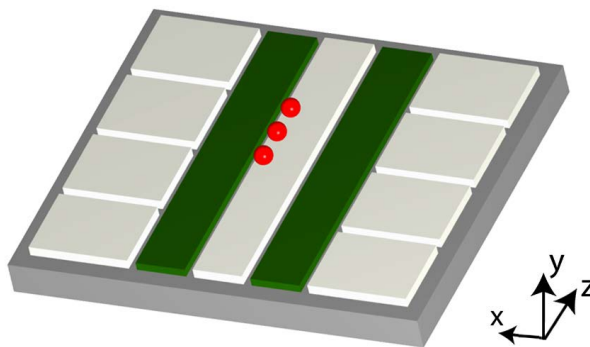


Figure 3.4: Schematic of a linear surface trap. All electrodes are located in a single plane on top of a substrate with ions trapped above the surface. The trap consists of two RF electrodes (green) and multiple DC electrodes (gray) which are RF-grounded. Applying an RF voltage to the green electrodes creates the pseudopotential to trap ions in the $x-y$ plane. DC voltages applied to the segmented DC electrodes generate a confinement in the axial (z) direction.

silicon-patterning technologies. On the one hand, this can help to improve the fabrication resolution. On the other hand, CMOS technology could then be directly implemented on the trap chip in order to control and filter the trapping voltages. Therefore, highly doped silicon-substrates and silicon-electrodes were tested [59]. Furthermore, CMOS compatible metals like aluminium were used as trap electrodes [60, 61], and an entire trap has been fabricated using 90-nm CMOS foundry processes [62].

The basic elements of the shuttling and the nearest-neighbor interaction architecture could already be realized in surface traps. Shuttling of ions along a linear trap and through junctions as well as the separation and recombination of linear ion strings has been shown [39, 63]. Furthermore, the coupling of ions confined in different traps was demonstrated [64].

In comparison to multi-layer traps, the fabrication of surface traps is typically simpler and faster. However, the trap depth - the minimum kinetic energy which an ion requires to exit the trap - is significantly smaller due to the strongly modified electrode configuration compared to the hyperbolic trap (see section 2.1.2). For the same reason, the efficiency parameter in surface traps is smaller ($\epsilon=0.2-0.3$) than the one in multi-layer traps ($\epsilon=0.7-0.8$). For example, a multi-layer trap and a surface trap with the same ion-electrode separation were simulated in the master's thesis of A. Pauli [65]. The trap depth in the surface trap was smaller by factor 30. The efficiency parameters of the surface trap and the multi-layer trap were 0.32 and 0.76, respectively.

Furthermore, addressing and cooling of all motional modes can be more challenging in surface traps. For surface traps, the laser beams are typically aligned parallel to the surface in order to minimize stray light which otherwise handicaps the ion detection by

reducing the signal-to-noise ratio. This, however, precludes the cooling and addressing of the motional mode perpendicular to the surface shown in fig. 3.5a (see also section 2.4.1). There exist different approaches to mitigate this issue. An asymmetric trap design can be used where the two RF electrodes differ in width [66]. The corresponding trapping potential is rotated due the asymmetry, so that none of the principal axes are normal to the plane of the trap (see fig. 3.5b). This means that a single laser beam which is aligned parallel to the surface and non-perpendicular to the trap axis has a projection along all three principal axes. This approach is implemented in the trap design used in this work (see chapter 5). A similar effect can be achieved in a symmetric trap by dividing the center electrode into two [67]. By applying different voltages to the two split electrodes the overall potential will be rotated (see fig. 3.5c). Another approach is a through-wafer slot located in the middle of the center electrode [60]. This enables the alignment of laser beams perpendicular to the trap surface without producing additional stray light (see fig. 3.5d).

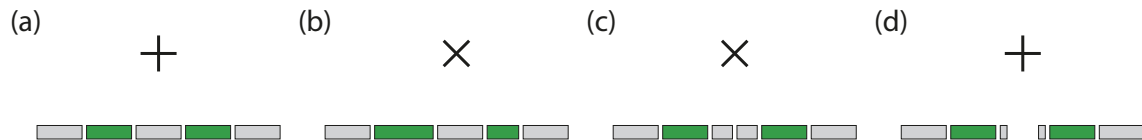


Figure 3.5: Cross-section of different surface-trap configurations perpendicular to the trap axis. The straight lines show the principal axes of the radial modes. (a) Symmetric trap. The motional mode perpendicular to the surface cannot be addressed by a cooling laser parallel to the surface. (b) The motional modes are rotated due to the asymmetric RF electrodes. (c) Different voltages are applied to the split center DC electrodes which rotates the principal axes. In (b) and (c) a laser parallel to the surface can address both radial modes. (d) A slot in the middle of the center electrode enables the alignment of a laser beam perpendicular to the surface without creating stray light.

3.2 Motional heating

One of the important characteristics of an ion trap is its motional heating rate, \dot{n} [68]. This heating rate describes how fast uncooled ions heat up in the harmonic potential due to coupling to the environment. In other words, it is the temporal increase of the phonon number for a certain mode. This is especially important for quantum gate operations with ions. As mentioned before, the modes of common motion - shared by all ions in the trap - are used to couple the electronic quantum state of different ions. To achieve high fidelities on these gate operations, the motional modes used must not appreciably heat up during gate time. For example, the implementation of a Mølmer-Sørensen gate [69] requires a heating rate of less than ~ 100 phonons/s in order to obtain a gate infidelity smaller than 10^{-3} , which is assumed to be the upper limit for fault-tolerant quantum computation [70].

3.2 Motional heating

Different causes of motional heating are discussed in the section 3.2.1. Possible techniques to reduce it are introduced in section 3.2.2, and methods to measure the heating rate are presented in the section 3.2.3.

3.2.1 Possible sources

Motional heating of trapped ions is caused by electric field noise at the position of the ion. The frequency component of the field noise which is resonant with a certain trap frequency ω_{Ti} can incoherently drive the corresponding mode and thereby heat it. For this reason, the noise is usually described by its spectral density $S_E(\omega)$ (unit $\text{V}^2/(\text{m}^2\text{Hz})$). Typically, the trap frequencies are 0.5-5 MHz. Knowing the spectral density of the electric-field noise, $S_E(\omega_{\text{Ti}})$, the related heating rate, \dot{n} , for a single ion can be calculated using the following equation [68, 71]:

$$\dot{n} = \frac{Q^2}{4m\hbar\omega_{\text{Ti}}} S_E(\omega_{\text{Ti}}). \quad (3.1)$$

Q and m are the charge and the mass of the ion, respectively.

The maximum acceptable level of electric field noise consistent with quantum computing is now estimated. Consider a $^{40}\text{Ca}^+$ ion which is trapped in a harmonic potential with a trap frequency $\omega_{\text{Ti}} = 2\pi \times 1 \text{ MHz}$. The heating rate of the ion is assumed to be 100 phonons/s, which corresponds to the upper limit for fault-tolerant quantum computing calculated (see above). According to eq. (3.1) an acceptable spectral density of the field noise is then $< 10^{-12} - 10^{-13} \text{ V}^2/(\text{m}^2\text{Hz})$. The level of noise actually observed in a trap may be significantly above this level. The noise can arise from a number of different sources [68], each of which has different characteristic scalings with frequency, trap size, trap geometry and temperature. Some of the sources which are thought to be important are summarised here.

Electromagnetic interference

Electromagnetic radiation (EMR) propagating through free space is one possible source of electric-field noise. A well-known component of the EMR is black-body radiation. However, its spectral density at room temperature and 1 MHz is only $\sim 10^{-22} \text{ V}^2/(\text{m}^2\text{Hz})$ (irrespective of trap size), and therefore negligibly small [68]. Other sources for EMR can be natural, like thunderstorms [72], or man-made, like power lines [73]. Especially in commercial buildings, where ion trapping experiments are typically performed, EMR can be very high at 1 MHz ($\sim 10^{-10} \text{ V}^2/(\text{m}^2\text{Hz})$) [68, 74].

In addition to the direct interaction of EMR with the ions, the radiation can also couple to the wiring of the ion traps. This can cause voltage fluctuations on the trap electrodes which, in turn, create field noise at the trapping site.

Johnson-Nyquist and technical noise

Johnson–Nyquist noise is the electrical noise which is generated by the thermally induced motion of the charge carriers in an electrical conductor [75, 76]. The electric-field noise at the trapping site caused by the trap electrodes scales with D^{-2} where D is a characteristic trap dimension [68]. The spectral density of electric-field noise can be written as

$$S_E^{(\text{JN})} = \frac{4k_B T R_{\text{JN}}(\omega, T)}{D^2}, \quad (3.2)$$

where k_B is the Boltzmann constant. $R_{\text{JN}}(\omega, T)$ is the frequency- and temperature dependent resistance and T is the temperature of the conductor. It is important to note that R_{JN} does not only consist of the trap electrodes’ resistance but incorporates the whole electrical system consisting of trap electrodes, wiring and voltages sources. The total resistance which is relevant can be reduced by the integration of appropriate filters as discussed in section 3.2.2.

Patch potentials

The surface of an ideal conductor forms a perfect equipotential. However, for real materials, the potential on the surface of an electrode is not perfectly homogeneous. Different crystal orientations and grain structures in the conductor [77] as well as adsorbates and contaminations on the conductor surface can cause patch potentials [68]. If these patches temporally fluctuate they create electric-field noise which can be a further source for motional heating. The absolute magnitude of the field noise produced by the patches depends on a wide variety of parameters like the size of the patches and their density.

3.2.2 Minimizing the heating

There exist several methods which are known to reduce the motional heating. Shielding of the setup and filtering of the wiring helps to reduce noise caused by EMR and Johnson noise. Cleaning of the electrodes’ surfaces can also decrease the motional heating. This might be connected to an reduction of the patch potentials on the surface. These effects are discussed in detail in this section. Besides them, it could be shown that cooling of the ion trap to cryogenic temperatures helps to decrease the heating as well. Since ion trapping experiments in a cryogenic environment have further advantages over experiments at room temperature, this is discussed separately in the section 3.3.

Shielding and filters

Electromagnetic radiation which directly interacts with the ions can be reduced by installing the trap in a shielded environment. The vacuum chamber containing the trap is usually made from metals like stainless steel and hence already provides some shielding.

3.2 Motional heating

The shielding can be further improved by enclosing the trap in a Faraday cage made from a highly conducting metal like copper [79, 80]. To avoid EMR coupling to the wiring of the trap, short and shielded cables should be used. For example, coaxial cables are well suited for that purpose.

In addition, low-pass filters should be installed to filter any noise in the cables. This noise can be created by EMR pickup as well as Johnson noise due to the intrinsic resistance of the cables and the technical noise created by the voltages sources. The filters should be located as close as possible to the trap in order to minimize the length of the unfiltered cables.

Surface cleaning

The in-situ cleaning of the electrode surfaces has proven to be a promising approach to reduce the motional heating of the ions. Adsorbates and contaminants are removed from the electrode surfaces after mounting the trap in the vacuum chamber and evacuating the chamber. Since the trap is under high vacuum for the entire time between cleaning and the ion trapping experiments recontamination of the surfaces can be reduced. One way of in-situ cleaning can be performed by using UV lasers. As shown by Allcock *et al.* [81], the motional heating was halved after illuminating the surfaces with pulsed UV light.

Another way is the implementation of sputter cleaning. This method has been commonly used in surface science research for a long time [82] but was only recently introduced to ion trap preparation. The surface is bombarded by Ar^+ ions to remove the top atomic layers of the electrodes including all contaminants located on the electrodes. The motional heating could be reduced by a factor of about 100 using this technique [79, 83]. Besides the in-situ cleaning, an ex-situ plasma cleaning just before installing the trap can help to decrease the heating. By this method, the measured heating rate has been reduced by an order of magnitude [84].

3.2.3 Heating-rate measurement

There exist several methods to measure the heating rate of trapped ions. For example, using the temperature-dependent variation of the scattering rate on the Doppler-cooling transition it is possible to infer the temperature and subsequently the heating rate of the ion [85, 86]. This method is technically simple but is not suited for measuring the very low heating rates we observe in our experiments. Low heating can be determined by the technically more complex resolved-sideband techniques.

This method investigates the motional sidebands on the quadrupole transitions to determine the motional state of the ion. Changes of the phonon number state can be resolved that are smaller than 0.1 phonons. To execute this method a frequency-stabilized laser (linewidth: ≤ 1 kHz) for the quadrupole transition is necessary and sideband cooling

of the ion close to the ground state is required (see section 2.4.2). The laser-pulse sequence used is shown in fig. 3.6. The ion is first cooled to the Lamb-Dicke regime by Doppler cooling. The phonon number is further decreased by sideband cooling to bring it close to the ground state. The cooling lasers are switched off to let the ion heat up for a certain waiting time. A quadrupole-laser pulse, which is tuned either to the red or the blue sideband of the electronic-qubit transition, is then used to drive sideband Rabi flops. This provides information about the ion's motional state (see section 2.3). Finally, the electronic state of the ion is detected using the shelving technique (see section 2.4.3).

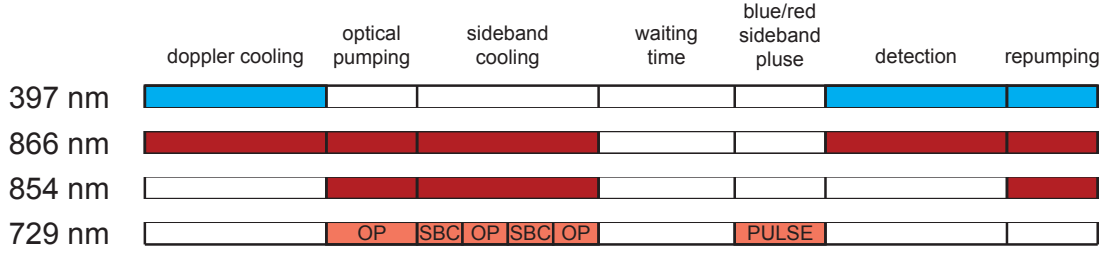


Figure 3.6: Pulse sequence for sideband spectroscopy to measure the phonon number of the trapped ion. The heating rate can be determined by varying the waiting time.

The basic physics of this method is summarized here, and a detailed description can be found elsewhere [30]. Given the randomizing nature of the photon absorption and emission process on the ion's motion, it is reasonable to assume that the motional state of the ion is thermally distributed. The probability of the single phonon states can then be written as follows:

$$P_n = \left(\frac{\bar{n}}{\bar{n} + 1} \right)^n \frac{1}{\bar{n} + 1}, \quad (3.3)$$

with \bar{n} being the mean phonon number of the thermal state.

The Rabi flops driven on the red (blue) sideband of a thermally distributed state are a superposition of the flops on the individual Fock states. The occupation probability of the excited state $|D\rangle$ is then:

$$P_{|D\rangle}^{RSB}(t) = \sum_{n=1}^{\infty} P_n \sin^2 \left(\frac{\Omega_{n,n-1} t}{2} \right) \quad (3.4)$$

$$P_{|D\rangle}^{BSB}(t) = \sum_{n=0}^{\infty} P_n \sin^2 \left(\frac{\Omega_{n,n+1} t}{2} \right). \quad (3.5)$$

$\Omega_{n,n-1}$ and $\Omega_{n,n+1}$ are the coupling strength on the first red and blue sideband, respectively, and are defined in eq. (2.26) and eq. (2.27). t is the length of the laser pulse driving the flops. The temporal evolution of the occupation probabilities for different mean phonon numbers is shown in fig. 3.7. Inserting eq. (3.3) in eq. (3.4) and rearranging the equation

3.3 Traps in a cryogenic environment

gives

$$\begin{aligned}
 P_{|D\rangle}^{RSB}(t) &= \sum_{n=1}^{\infty} \left(\frac{\bar{n}}{\bar{n}+1} \right)^n \frac{1}{\bar{n}+1} \sin^2 \left(\frac{\Omega_{n,n-1} t}{2} \right) \\
 &= \frac{\bar{n}}{\bar{n}+1} \sum_{n=0}^{\infty} \left(\frac{\bar{n}}{\bar{n}+1} \right)^n \frac{1}{\bar{n}+1} \sin^2 \left(\frac{\Omega_{n+1,n} t}{2} \right) \\
 &= \frac{\bar{n}}{\bar{n}+1} P_{|D\rangle}^{BSB}(t).
 \end{aligned}$$

The ratio, R , of the excitation probability on the red and the blue sidebands can be written as

$$R = \frac{P_{|D\rangle}^{RSB}}{P_{|D\rangle}^{BSB}} = \frac{\bar{n}}{\bar{n}+1}. \quad (3.6)$$

Rewriting the last equation provides a way to determine the mean phonon number of the ion by measuring the occupation probabilities for a red and blue sideband pulse, respectively:

$$\bar{n} = \frac{R}{1-R}. \quad (3.7)$$

Note that R does not depend on the pulse length, t . However, to achieve the highest contrast a pulse length is usually chosen which corresponds to the first maximum on the blue sideband transition (see fig. 3.7). Measuring R for different waiting times allows the heating rate to be determined. This method works best for small phonon numbers ($\bar{n} < 1$). For higher phonon numbers the difference between $\Omega_{n,n-1}$ and $\Omega_{n,n+1}$ is reduced, and consequently the accuracy of this method decreases as well. This can be seen in in fig. 3.7 for $\bar{n} = 5$.

3.3 Traps in a cryogenic environment

Since the original work of Deslauriers et al. [87] in 2006 in which the electrode temperature was significantly reduced, numerous groups have implemented traps in cryogenic systems [19, 80, 88–92]. On the one hand, the operation of traps at low temperatures (< 30 K) has several advantages compared to traps running at room temperature (~ 300 K) which are especially important for microtrap testing. These include a reduction in the rate at which trapped ions are heated; the possibility of achieving higher vacuum; enabling vacuum to be achieved faster - and in certain respects more simply; and the possibility of using novel materials which are not otherwise suitable for ion trapping. On the other hand, there are several disadvantages linked to cryogenic setups such as higher running costs; mechanical vibration; the need to consider thermal expansion and thermal connections. Both the advantages and disadvantages are discussed in this section.

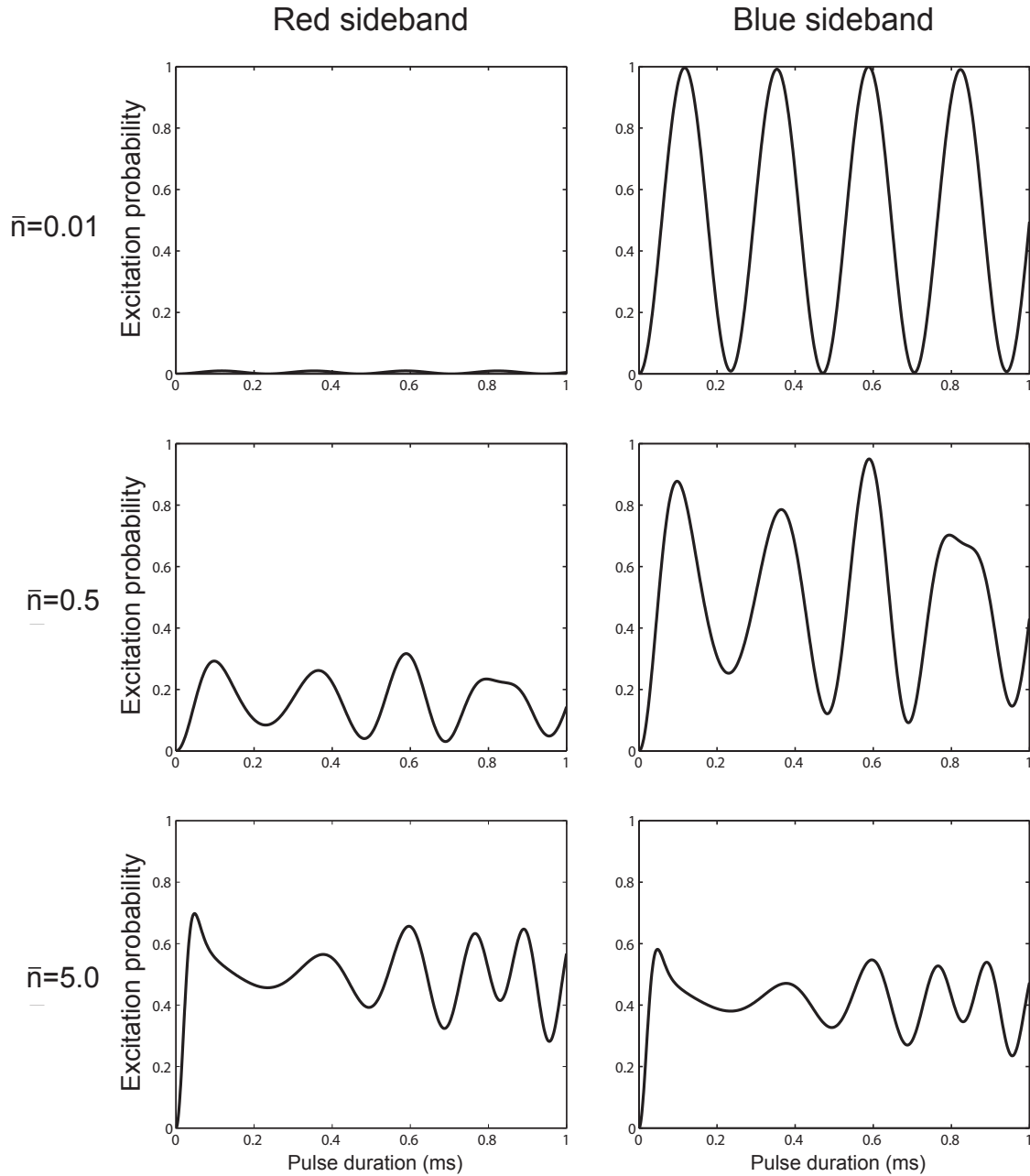


Figure 3.7: Simulation of the excitation probabilities, $P_{|D\rangle}^{RSB}$ and $P_{|D\rangle}^{BSB}$, as a function of the pulse duration for the red and blue sideband transitions based on eq. (3.4) and eq. (3.5), respectively. The motional states used for the simulation were thermally disturbed with an average phonon number \bar{n} . The Lamb-Dicke parameter, η , was taken to be 0.068 which is a typical value for the ion trapping experiments reported in this thesis.

3.3 Traps in a cryogenic environment

3.3.1 Reduced motional heating

The first significant advantage of operating traps at cryogenic temperatures is the reduction in the heating rate. Several experiments have investigated the temperature dependence of motional heating in ion traps [19, 87, 92, 93]. The ion traps, as well as the attendant apparatus used for these measurements, were far from identical and many of the differences were not well controlled. Therefore, it is not surprising that the details of the heating rate behavior as a function of the temperature were qualitatively different in the different experiments. Nevertheless, all experiments showed a significant reduction of the heating rate when the trap temperature was reduced. The heating rate of the traps which already showed a good performance at room temperature could typically be lowered by two orders of magnitude if the trap was cooled from 300 K to < 10 K. For traps with a comparatively high heating rate at room temperature a reduction of up to seven orders of magnitude was reported [19].

Fig. 3.8 shows the spectral densities of the electrical field noise measured in different ion-trap experiments and for different temperatures as a function of the ion-electrode separation. The spectral densities are widely spread over several orders of magnitude but there is a clear trend showing that they are lower at cryogenic temperatures.

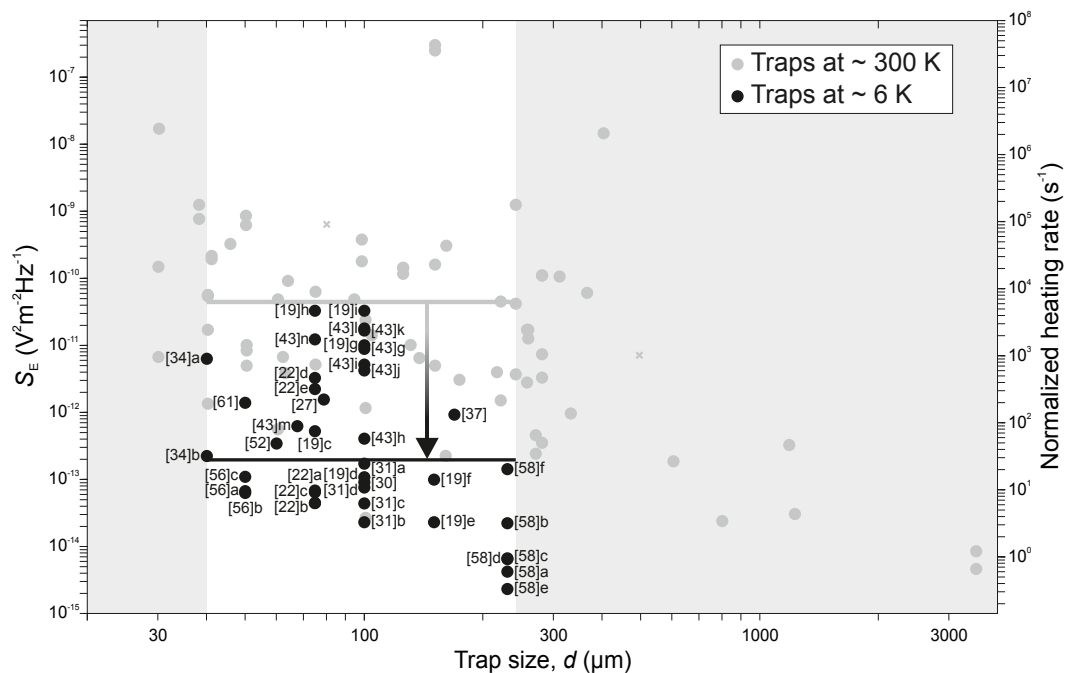


Figure 3.8: Electrical field noise measured in different setups and at different temperatures as a function of ion-electrode separation, d . Taken from [68] and used with permission. The numbers in square brackets refer to references within the original article.

There are several effects that can contribute to the reduction of heating rate. Cryo-

genic setups usually possess black-body shields made from copper or aluminium which enclose the ion trap and are cooled as well. Both metals are good electric conductors at room temperature and their conductivity increases by several orders of magnitude during the cooling [94]. Therefore, these shields provide excellent electric shielding [80] which reduce EMR noise. A second source of noise which is temperature-dependent is Johnson noise. It directly depends on the temperature as shown in eq.(3.2). Furthermore, the resistance of the conductors (wiring, electrodes) causing the Johnson noise typically decreases with decreasing temperature. Both effects cause a reduction of the noise when the trap and wiring (at least partially) are cooled to cryogenic temperatures. Furthermore, it is reasonable to expect that the fluctuating dipoles which were listed as a possible cause of the motional heating in section 3.2.1 are thermally driven. Cooling the surfaces then decreases this component of the total heating rate. The experiments so far do not provide clear evidence to identify which of these three effects (or some other effect) is responsible for the reduction. Nor is it currently possible to exclude any of these effects. Nonetheless, cryogenic temperatures significantly reduce the motional heating.

3.3.2 Vacuum and turnaround time

The background-gas pressure at the trapping site should be as low as possible. Collisions with background-gas molecules can heat up the trapped ions. In the worst case, the ions can even be knocked out of the trap. This is especially relevant for surface microtraps which are very shallow (10-50 meV). There are well established methods of achieving sufficiently high vacuum (i.e. sufficiently low pressure). The ways in which this is done are very different depending on whether the system is to be operated at room temperature (~ 300 K) or at cryogenic temperatures (~ 6 K).

Ion traps at room temperature are typically operated at pressures of $10^{-11} - 10^{-12}$ mbar, which corresponds to ultra high vacuum (UHV). To achieve this vacuum, careful design and construction of the vacuum vessel and its interior are absolutely essential. This includes the sole use of materials with low vapor pressures and small outgassing rates. All in-vacuum parts have to be thoroughly cleaned to remove any residues like greases and adhesives. After assembling the vessel it is connected to a molecular turbo pump and bake-out is done at 100-300 °C for several days. This helps to remove the remaining water from the interior of the chamber and accelerates the outgassing of light-weight molecules like hydrogen which otherwise slowly diffuse into the vacuum and degrade it.

The situation is different for cryogenic setups. An extremely high vacuum (XHV), which corresponds to a pressure $< 10^{-12}$ mbar, can be achieved by cooling the system to low temperatures since most background-gas molecules freeze out at the cold parts of the setup. Table 3.1 shows the vapor pressure of the most common molecules in a vacuum chamber at different temperatures. Besides helium, which condenses only at 4.2 K, the vapor pressure of all other molecules dramatically decreases when cooled below 10 K.

3.3 Traps in a cryogenic environment

Fortunately, the amount of helium in air is rather small (5.240 ppm [95]) and the partial pressure of helium is usually negligibly small in the vacuum chamber.

gas	temperature (K)	pressure (mbar)
H ₂ O	373.15	1013 [95]
	20	$< 10^{-13}$ [96]
N ₂	77.25	1000 [95]
	20	10^{-11} [96]
O ₂	90.05	1000 [95]
	20	10^{-13} [96]
Ne	27.05	1000 [95]
	12.15	0.01 [95]
H ₂	20.35	1000 [95]
	14.55	100 [95]
He	4.25	1000 [95]

Table 3.1: Vapor pressure of the most common gases in ambient air at different temperatures.

To reach XHV in a cryogenic system, a rough vacuum ($< 10^{-4}$ mbar) has to be established in the system first. This can be done by operating a molecular turbo pump connected to the system for several hours. Then the cryostat is switched on and the system is cooled down which takes several more hours. There is no bake-out of the system required, which significantly reduces the turnaround time of the entire trap-changing cycle². For example, a turnaround time shorter than 24 h was achieved in this work. This makes a cryogenic system to be a good environment for testing trap designs and different fabrication parameters. Furthermore, the outgassing of the materials used is suppressed at low temperatures. This allows the use of materials which would otherwise be non-UHV-compatible such as many plastics and adhesives.

3.3.3 Cryogenic systems

There exist several systems which can be used to cool ion traps to low temperatures. For example, there is a bath cryostat which is basically a dewar filled with the cooling medium (e.g. liquid helium or liquid nitrogen). The cold stage is thermally connected to the tank of the dewar, and it is cooled by evaporating the cooling medium. Another type of cryostat is the flow cryostat. In this case, the cooling medium flows through a heat exchanger which is connected to the cold stage of the system. In contrast to a bath cryostat, the cooling power (and thereby the temperature) can be tuned by controlling the rate of cooling-medium flow. A third type of cryostat is the closed-cycle cryostat. This is basically an inverted Stirling engine where work is used to pump heat from one stage to

²Trap-changing cycle in a cryogenic system: Warm up the system, break the vacuum, remove the trap and install a new one, cool down the system and retrap ions.

another, thereby cooling the first stage. This type of cryostat was used in this work and a detailed description of it is given in section 4.1.

As stated above, besides the advantages of cryogenic systems for ion trapping there are also several difficulties and disadvantages. The initial setup costs and running costs of a cryogenic system are significantly higher than those of a standard room-temperature setup used for ion trapping. In particular, the initial costs of a closed-cycle system are, in general, very high due to the complexity of the system. By contrast, the running costs for a bath or flow cryostat are higher because of the continuous consumption of liquid helium.

The cooling process creates mechanical vibrations in the cryogenic system. In particular in a closed-cycle system, the amplitude of these vibrations caused by moving parts and pressure changes is relatively large ($\sim 10 \mu\text{m}$ [97]). These vibrations can cause oscillations of the ions with respect to the laser beams. From the ions' point of view the laser beams are moving which generates intensity fluctuations at the ion's location as it moves through the beam waist. This reduces the fidelity of the quantum gates [29]. Therefore, a special vibration-isolation system must be included to suppress this movement (see section 4.1.2).

Another important point which has to be considered is the thermal coupling. On the one hand, there should be a strong thermal coupling between the sample (ion trap) and the cold stage. On the other hand, the coupling between the cold stage and the hot parts of the cryogenic system should be as small as possible. This can be accomplished by the proper choice of materials (supporting parts and wiring) and a thermal anchoring of the wires (see section 4.1.4).

Furthermore, attention must be paid to the thermal expansion. It can vary significantly for the different materials used and can cause problems during the cool-down [94]. For example, optical feedthroughs and electrical connectors may break when cooled if not properly designed.

Chapter 4

Experimental setup

The experimental setup which was built and used throughout this thesis is described in this chapter. The main components of the setup are shown in fig. 4.1.

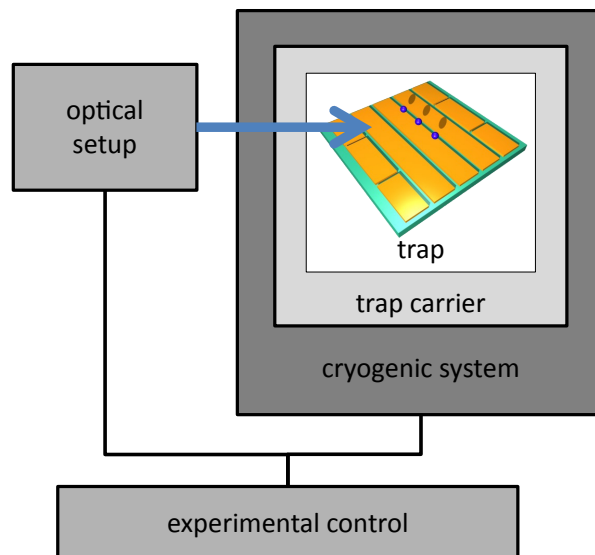


Figure 4.1: Overview of the experimental setup.

The ion traps should be operated in vacuum and at low temperatures (about 10 K). Therefore, they are located in a vacuum chamber which is connected to the cold stage of a cryostat. This entire system is referred to as cryogenic system and is described in section 4.1. The experimental setup should facilitate a simple exchange of the traps in order to enable quick testing of different traps. For this reason, a special trap carrier was designed which is used to mount the trap in the cryogenic system. It is presented in section 4.2. Lasers are used to cool and address the ions, and an optical detection system is needed to detect them. Section 4.3 describes this optical setup. Finally, an experimental control is required to control the different components of the experiment. This is introduced in section 4.4.

4.1 Cryogenic system and vacuum chamber

The different components of the cryogenic setup are presented in this section. Section 4.1.1 introduces the Gifford-McMahon cryostat (closed-cycle cryostat) used to cool the ion traps. The moving parts of the cryostat cause strong vibrations (amplitude 20-30 μm) as mentioned in section 3.3.3. Therefore, a vibration-isolation system is installed. It is described in section 4.1.2. The vacuum chamber and its electric wiring are presented in section 4.1.3 and 4.1.4, respectively. The trapping experiments use calcium ions. These are loaded from a calcium oven which is introduced in section 4.1.5. The magnetic field at the trapping site required to split the degenerate Zeeman sublevels is created by pairs of electromagnetic coils. These are presented in section 4.1.6. Details about the cooling down procedure are given in section 4.1.7.

4.1.1 Gifford McMahon cryostat

The cryostat used is a closed-cycle Gifford-McMahon system (GM). The Gifford-McMahon cryostat was invented by William E. Gifford and Howard O. McMahon in 1957 [98]. Its mode of operation is similar to an inverted Stirling cycle, where mechanical work is supplied and heat is pumped from a cold stage to a hot stage. The main components of the GM cryostat are depicted in fig. 4.2.

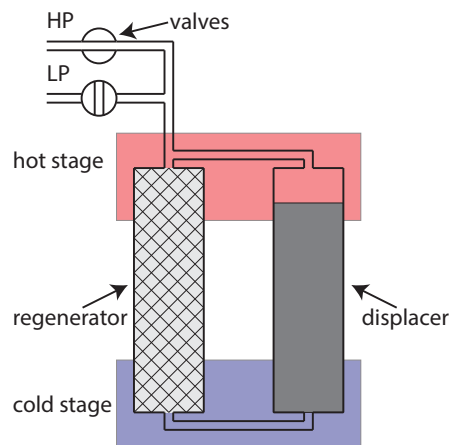


Figure 4.2: Gifford McMahon system. It consists of a hot and a cold stage, connected by a displacer and a regenerator and is filled with a working fluid. Via valves the system can be either connected to a reservoir of working fluid at high (HP) or low (LP) pressure in order to change the pressure in the system.

There is a hot and a cold stage, connected by a displacer and a regenerator¹. The system is filled with a working fluid (e.g. helium). The displacer either pushes the working fluid from the hot stage, through the regenerator to the cold stage or (reversed) pushes

¹Typical regenerator materials are meshes of copper, lead or stainless steel [99].

4.1 Cryogenic system and vacuum chamber

the working fluid from the cold stage through the regenerator to the hot stage. The regenerator precools the working fluid on its way from the hot stage to the cold stage and stores its heat. On the way back from the cold stage to the hot stage the working fluid is heated up again by the stored heat. Furthermore, the pressure of the working fluid in the system can be changed by either connecting it to a reservoir of working fluid at high pressure (HP) or a reservoir of working fluid at low pressure (LP).

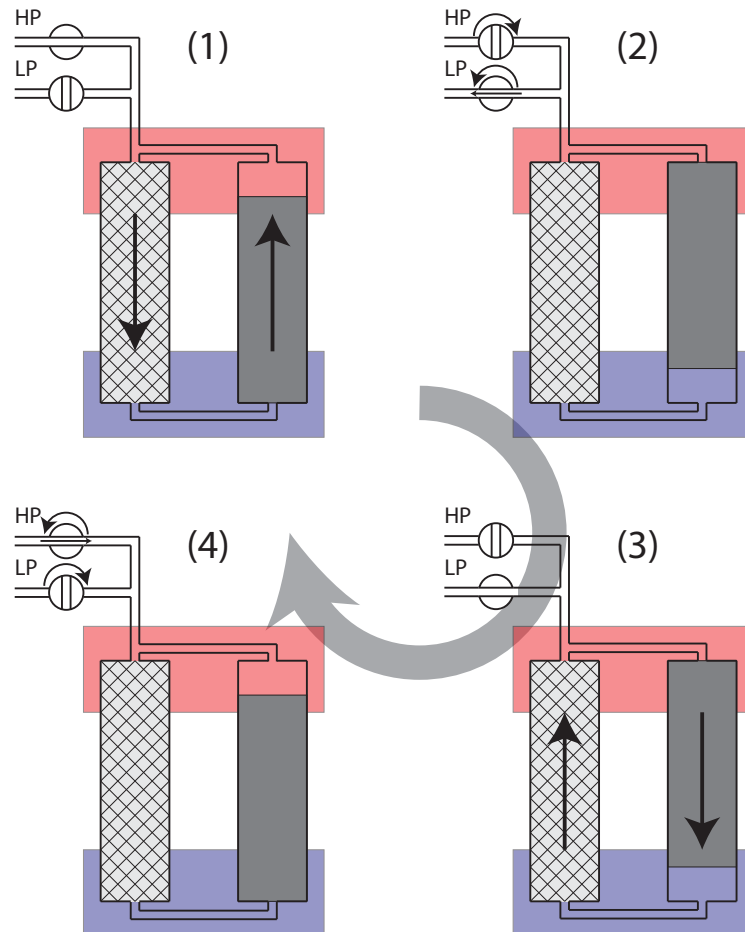


Figure 4.3: Gifford McMahon cycle.

The GM cooling cycle in which heat is pumped from the cold stage to the hot stage, consists of four steps. They are shown in fig. 4.3 and are explained here:

1. The system starts at high pressure (HP valve is open and LP valve is closed). The displacer moves upwards and pushes the working fluid from the hot stage through the regenerator into the cold stage. The regenerator precools the working fluid and stores its heat.
2. The HP valve closes and the LP valve opens. The pressure in the systems drops and

the working fluid isothermally expands. The heat necessary for that expansion is provided by the cold stage. During this step the actual cooling takes place.

3. The displacer moves downwards and pushes the working fluid back to the hot stage via the regenerator. The stored heat is released and heats the working fluid.
4. The LP valve closes and the HP valve opens. This compresses the working fluid in an isothermal way and heats up the hot stage.

Cryostat used in this work

The cryostat used in this work is a two-stage² GM cryostat³ The working fluid is ^4He . A schematic is given in fig. 4.4. The first stage can reach a final temperature of $<50\text{ K}$. It

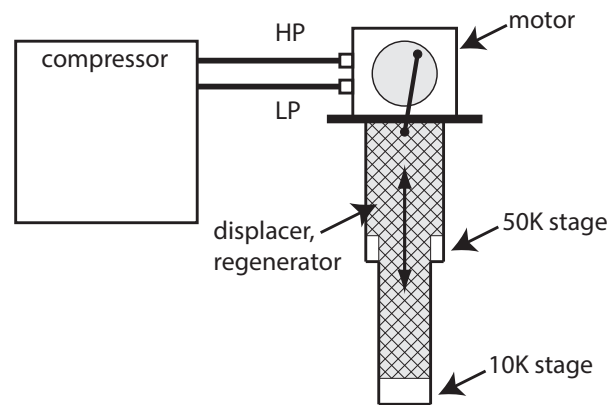


Figure 4.4: Schematic of cryostat used. It consists of two cooling stages to achieve a final temperature $<10\text{ K}$. The displacer and the regenerator are combined. They are moved by a motor located at the top of the cryostat. A compressor provides the high and low pressure reservoirs.

is called the 50 K stage. A temperature of $<4\text{ K}$ can be reached at the second stage if no additional heat load is attached. The cooling power of this stage is 500 mW, according to the manufacturer’s specifications. However, the modifications necessary to mount and operate an ion trap increase the heat load. The temperature measured at the second stage is typically higher by a few degrees. Therefore, this stage is referred to as the 10 K stage. A compressor⁴ provides the low- and high-pressure reservoirs for the GM cycle and is connected to the cryostat via two 3 m long helium gas lines. The cycle frequency is about 2 Hz. The compressor has to be cooled during operation in order to avoid overheating. Therefore, a chiller⁵ was installed.

²Two cooling stages in series are required in order to reach a final temperature $< 10\text{ K}$.

³Advanced Research Systems, DE-210B

⁴Advanced Research Systems, ARS-10HW

⁵KTK, JWA/CL 9 SKP

4.1.2 Vibration isolation

As mentioned in section 3.3.3, vibrations of the ion trap (and the trapped ion) with respect to the laser beams cause intensity fluctuations at ion's location. This decreases the fidelity of the quantum gates and should, therefore, be kept to a minimum. The operation of a GM cryostat, however, creates strong vibrations caused by the moving parts in the cryostat (motor and displacer) and the periodic pressure changes at the second stage due to the cooling cycle.

The vibrations at the second stage of GM cryostat are typically of order 20-30 μm along the axis (axial axis) of the cryostat and about 5 μm perpendicular to this axis (radial axes) [97]. For comparison, the typical width of laser beam used is about $\sim 20 \mu\text{m}$, and the corresponding intensity fluctuations caused by the vibrations of a GM cryostat are then $>50\%$.

There exist different approaches to minimize the vibrations [100]. The vibration isolation of the cryostat used in this work is accomplished by a method which uses helium buffer gas. The buffer gas mechanically decouples the cryostat from the sample, while maintaining a good thermal contact. The principle of the vibration-isolation system is shown in fig. 4.5.

The cryostat (see fig. 4.5a) is equipped with the additional adapter⁶ (*GMX-20*). The adapter, which is slightly larger in diameter, is mounted on the cryostat (see fig. 4.5b). There is a gap of about 5 mm between the cryostat and the adapter, which is filled with helium (see fig. 4.5c). The adapter is flanged to a vacuum shroud (see fig. 4.5d). Together, the shroud and the adapter form the vacuum chamber in which the trap is mounted (see section 4.1.3 for further details). The cryostat is fastened to the ceiling of the laboratory via aluminum profiles, whereas the vacuum chamber is mounted on a floating optical table (see fig. 4.5d). By this means, the vibrations in the vacuum chamber can be significantly reduced. The manufacturer claims that this interface system should reduce the vibrations of the cryostat to an amplitude of 15 nm.

Vibration measurements were performed on the cryogenic system after installation using a laser interferometer⁷. To measure the vibrations of a target with respect to the interferometer, a laser beam provided by the interferometer is directed to a reflecting part of the target. The reflected beam is coupled back in the interferometer where it is merged with a reference beam and directed onto a photodetector. The vibration amplitude and frequency are extracted from the modulation of the interference pattern detected.

To measure the axial vibrations of the second stage (perpendicular to the optical table in fig. 4.5e), the laser beam is coupled into the chamber from below via the CF160 viewport (see section 4.1.3). In this case, the metal electrodes of the surface trap are used as a mirror to reflect the beam. A reference measurement of the axial vibrations with the cryostat

⁶Advanced Research Systems, GMX-20

⁷SIOS SP 2000 DI

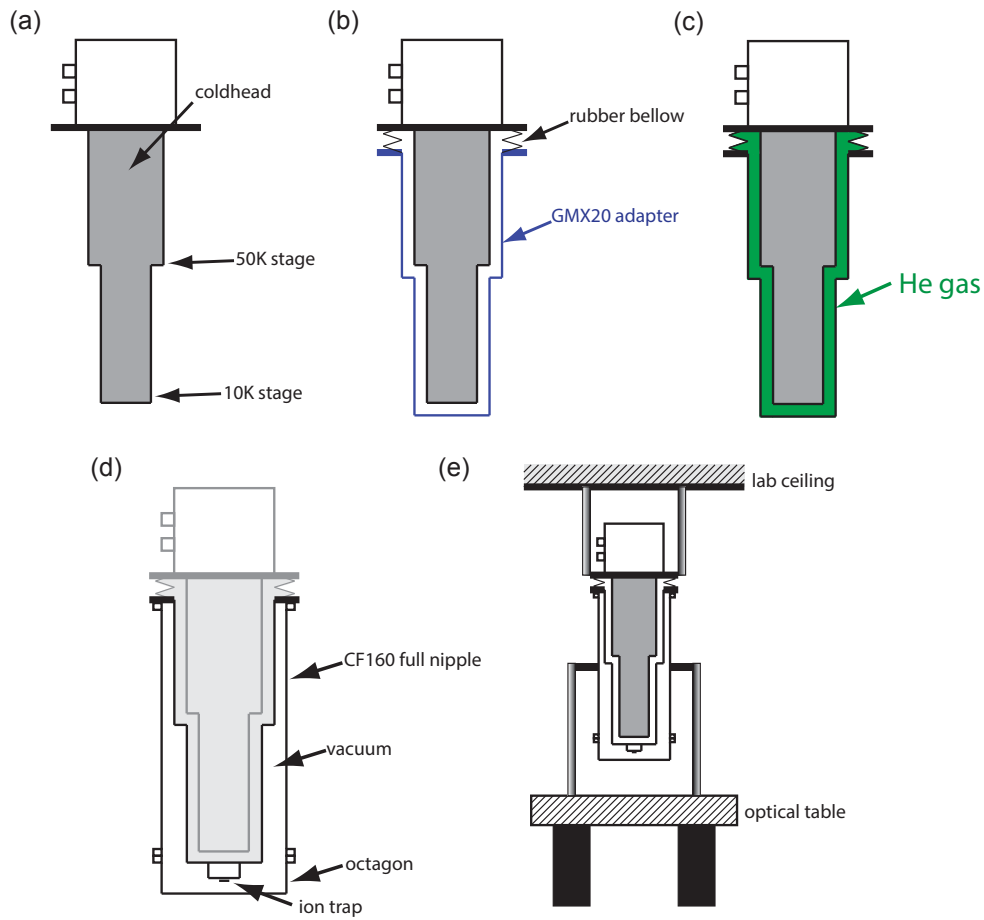


Figure 4.5: Overview of the vibration-isolation system. (a) The GM cryostat. (b) Cryostat and the GMX-20 adapter. (c) The gap between the cryostat and the adapter is filled with helium gas which mechanically decouples the cryostat from the adapter, while maintaining a good thermal contact. (d) The adapter and a vacuum shroud (consisting of a CF160 full nipple and an octagon) form the vacuum chamber, where the ion trap is located. (e) The cryostat is attached to the laboratory ceiling and the vacuum chamber is mounted on a floating optical table in order to mechanically decouple them.

being switched off is shown in fig. 4.6. The distance changes of the target (ion trap) are recorded for 40 s. In order to couple the beam from below into the vacuum chamber several mirrors were required which increased the total path length of the laser beam to about 2 m. The distance fluctuations of several hundred nm at a time scale of seconds in fig. 4.6 are mainly caused by thermally driven drifts of the mirrors, the ion trap and the interferometer with respect to each other. Fig. 4.7 shows the axial vibrations when the cryostat is running and cold (temperature at the 10 K stage: 5.2 K). The total vibrations caused by the cryostat are of order 200-300 nm.

To measure the radial component of the vibrations of cold stage, the laser beam was coupled via viewport (4) into the vacuum chamber (the labeling of the viewports is defined

4.1 Cryogenic system and vacuum chamber

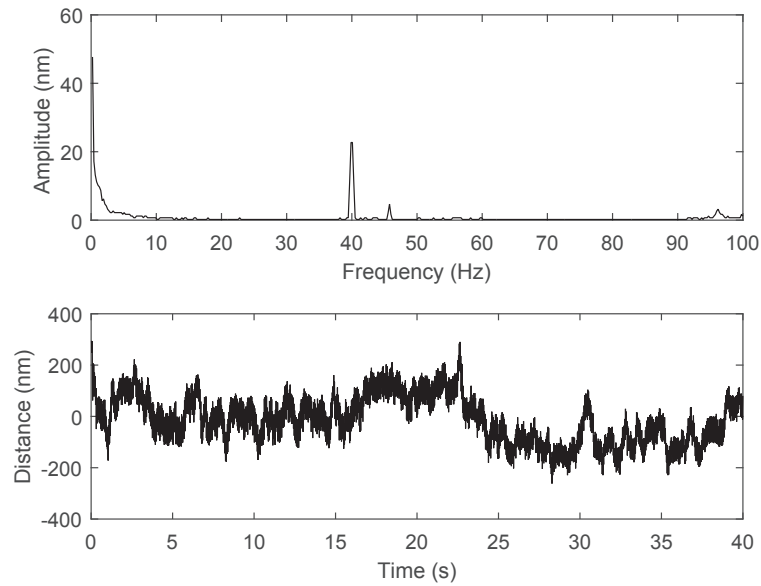


Figure 4.6: Axial vibrations of the cold stage as a function of time with the cryostat being switched off. The bottom plot shows the distance changes of the target with respect to the interferometer. The frequency components of the vibrations are given in the top plot.

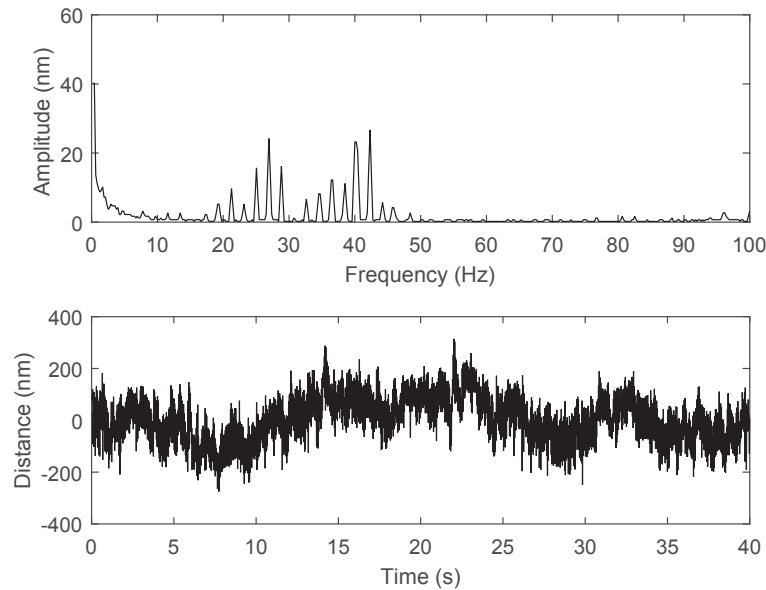


Figure 4.7: Axial vibrations of the cold stage as a function of time with the cryostat being switched on.

in section 4.1.3 and fig.4.9). It was directed onto a mirror which was attached to the cold stage in order to provide a reflecting surface. The radial vibrations are shown in fig. 4.8. These vibrations are significantly stronger than the axial vibrations. In particular, there is a strong vibration at 11.5 Hz with an amplitude of 190 nm. This is caused by the

single sided mounting of the vacuum chamber (see fig. 4.5e). The mounting posts are only attached to the middle of the vacuum chamber and thereby suboptimally suppress radial vibrations at the bottom of the chamber.

However, the intensity fluctuations of the laser beams at the ion's location caused by these vibrations are smaller than 0.5% for the typical beam diameters used throughout this work (see table 4.2). This is negligibly small for the measurements performed in this thesis.

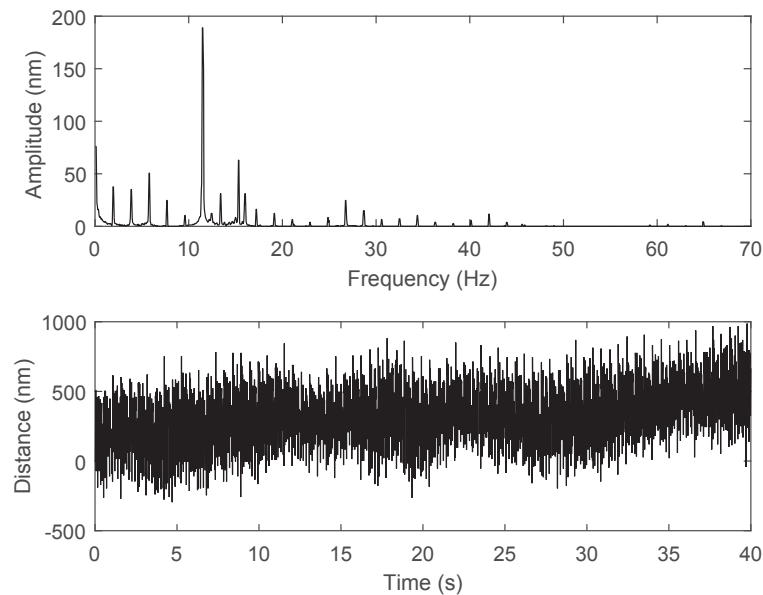


Figure 4.8: Radial vibrations of the cold stage as a function of time with the cryostat being switched on.

4.1.3 Vacuum chamber

The vacuum shroud is illustrated in fig. 4.5d and fig. 4.9. It is built from stainless steel parts (type 304) equipped with CF (ConFlat) flanges. The shroud basically consists of a home-made CF160 full nipple and a CF160 octagon vacuum chamber⁸. It encloses the *GMX-20* adapter, and together they form the vacuum chamber in which the trap is mounted. A pressure gauge⁹ is flanged to the vacuum shroud. There are eight CF40 flanges on the sides of the octagon. The atomic Ca-beam used to load the ion trap is introduced through the CF40 flange labeled (2) in fig. 4.9b (see also section 4.1.5). The other seven CF40 flanges are closed by BK7 viewports¹⁰. Another BK7 viewport¹¹ is flanged to the bottom CF160 flange of the octagon. The CF40 viewports are used to couple the laser beams into the

⁸Kimball Physics Inc., MCF800M-SO2000800 Metric Spherical Octagon

⁹Pfeiffer, PKR 251

¹⁰Vacom, VPZ40

¹¹Vacom, VPZ160

4.1 Cryogenic system and vacuum chamber

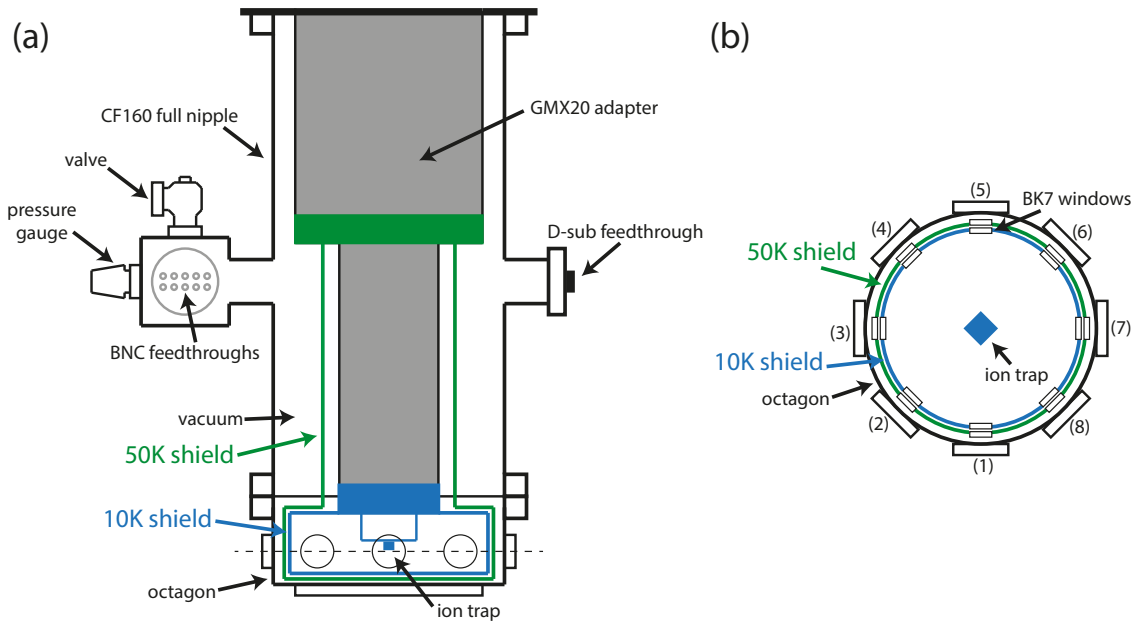


Figure 4.9: (a) Cross-section of the cryogenic system. The vacuum shroud (CF160 full nipple, octagon) and *GMX-20* adapter form the vacuum chamber. Electric feedthroughs on the CF160 full nipple are used to connect the trap electrodes and the temperature sensors with the outside world. The vacuum pump can be connected to the chamber via the valve and the pressure inside is monitored via a pressure gauge. A 50 K and a 10 K heat shield (non vacuum-tight) enclose the ion trap. They are connected to the 50 K (green) and 10 K (blue) stage, respectively. (b) Cross-section of the octagon. There are 8 viewports for optical access and for loading calcium ions labeled (1)-(8).

chamber and the ions' fluorescence light is detected through the CF160 flange. Therefore, they are equipped with a broadband anti-reflection (AR) coating¹² which improves the optical transmission (transmission > 99.5% for all relevant wavelengths).

Two radiation heat shields are installed in the vacuum chamber (see fig. 4.9 and fig. 4.10). The outer one is connected to the 50 K stage of the *GMX-20* adapter whereas the inner one is bolted to the 10 K stage. The purpose of the shields is to reduce the black-body radiation and the number of the background molecules at the ion trapping site, as they freeze out at the shield walls. The shields were made of Oxygen-Free High thermal Conductivity (OFHC) copper which ensures fast cooling of the shields and a small temperature gradient along them. Furthermore, the shields provide adequate shielding against electromagnetic field fluctuations because of the high electrical conductivity at low temperature. The wall thickness of the shield parts is 5 mm. The parts are bolted together by brass screws. The thermal expansion of brass is higher than that of copper. This ensures that screwed joints do not become loose during cool down. The contact surfaces of the parts are covered with Indium foil (thickness: 100 μm), which is a soft and pliable metal at

¹²Tafelmaier Dünnschicht-Technik GmbH

room temperature and fills any imperfections of the copper surfaces. This creates reliable bonds between the mating surfaces with low thermal and electrical resistance. Both shields possess several venting holes which help to shorten the pumping-down time. The holes are drilled at an angle of 45° with respect to the shield surface which prevents molecules from going directly from the room temperature part of the vacuum chamber to the trapping site. Each shield has eight 25 mm holes, aligned with the octagon's viewports. Each hole has a BK7 window¹³ clamped over it. The windows are coated with the same broadband AR coating as the vacuum chamber's viewports.

An open container filled with activated charcoal is located next to the trap and fixed to the 10 K shield (see fig. 4.10). The activated charcoal is a special form of carbon with a high degree of microporosity that significantly increases the surface area available for adsorption of molecules during cool down. The charcoal acts as a cryogenic pump when cooled and helps to improve the vacuum at the trapping site.

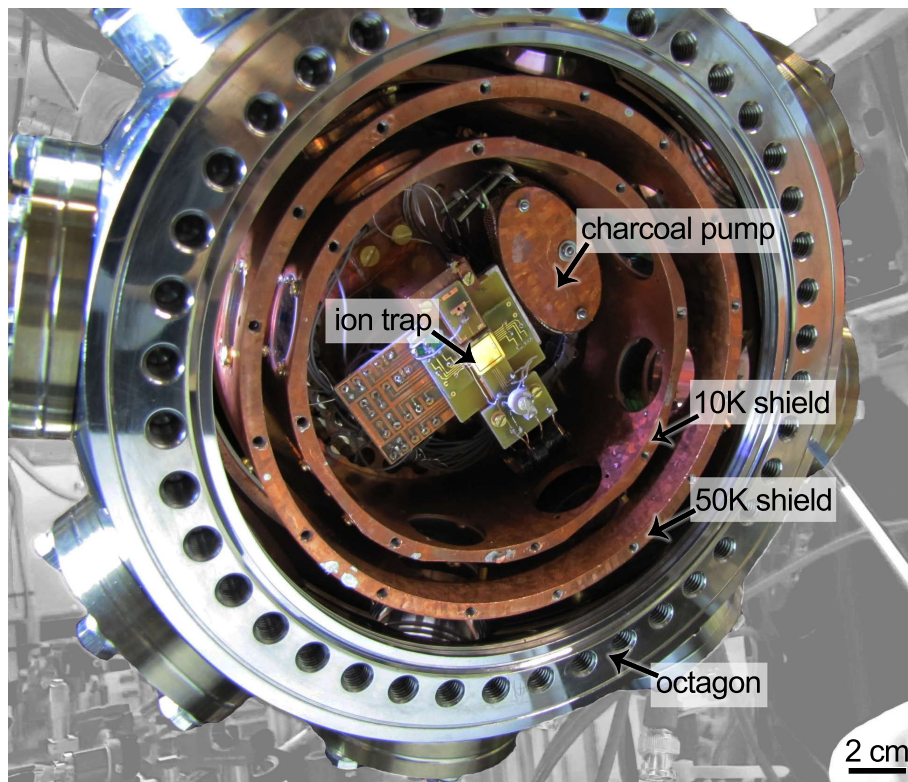


Figure 4.10: The trap located in the vacuum chamber is shown. It is enclosed by the octagon and the two heat shields. The charcoal container is located next to the trap.

¹³Topag Lasertechnik GmbH, BK7 window diameter: 25.0mm, thickness: 3mm, flatness: $\lambda/10$

4.1 Cryogenic system and vacuum chamber

4.1.4 Wiring and heater

There are 20 electrical lines installed in the cryostat to connect the trap's DC and RF electrodes with the outside world. The wiring is illustrated in fig. 4.11a. The vacuum shroud is equipped with two coaxial feedthroughs¹⁴, as shown in fig. 4.9. The in-vacuum wiring between the feedthroughs at 300 K and the 10 K stage uses stainless steel coaxial cables¹⁵ (length ~ 50 cm). These are used because the thermal conductivity of stainless steel is small (2-3 orders of magnitude smaller than copper [94]), which helps to keep the heat load at the 10 K stage to a minimum. Furthermore, the cables are thermally anchored at the 50 K stage via copper clamps (see fig. 4.11b). The steel coaxial cables are terminated with female coaxial connectors¹⁶ at the 10 K stage, which are clamped to the cover of the 10 K shield. In order to ensure electric isolation between the connectors and the copper shield PTFE (Polytetrafluoroethylene) spacers are used. Inside the 10 K shield, the coaxial lines are continued by copper coaxial cables¹⁷. Their ends are directly soldered to a breakout board (see fig. 4.11c). The plug connections at the 10 K stage enable a simple replacement of the final stage without replacing all of the wiring. It should be mentioned that the connectors used are not specified for cryogenic temperatures. However, no connection failures were detected during temperature cycling so far (> 100 cycles). The individual shields of the different coaxial lines are only connected with the common ground at the breakout board. The common ground is provided by the vacuum chamber (including the heat shields) and corresponds to the RF ground of the ion trap. This grounding scheme is used in order to avoid ground loops. To establish separable electric connections between the coaxial lines and the removable trap carrier, pogo pins¹⁸ are used which are soldered to the breakout board. The total resistance of the signal lines measured between the feedthrough and the pogo pins is about 15Ω . This relatively high resistance is caused by the high specific resistance of the steel coaxial cables.

The temperatures inside the cryostat are measured by silicon diode temperature sensors¹⁹. One sensor is attached to the 50 K stage. A second one is placed in the charcoal container and a third one is mounted on the trap carrier next to the trap. Twisted-pair wires²⁰ are used to connect the sensors. In order to keep the heat load small, the wires are made up of phosphor bronze which has a thermal conductivity around one order of magnitude smaller than copper. Furthermore, they are thermally anchored to the 50 K and the 10 K stages. The wires are soldered to a D-sub feedthrough²¹ at the vacuum

¹⁴Both of type Accu-Glass, 25D-5CX2-450

¹⁵Lakeshore, Type SS

¹⁶Microdot, 142-0000-0001

¹⁷They are terminated by male coaxial connectors: Microdot, 142-0000-0002

¹⁸Mill-Max, 0929-0-15-20-75-14-11-0. They contain spring-loaded pins made from a beryllium-copper alloy which also work at cryogenic temperatures [94].

¹⁹Lakeshore, DT-670-SD-1.4L

²⁰Lakeshore, DT-32

²¹Accu-Glass, 25D-450

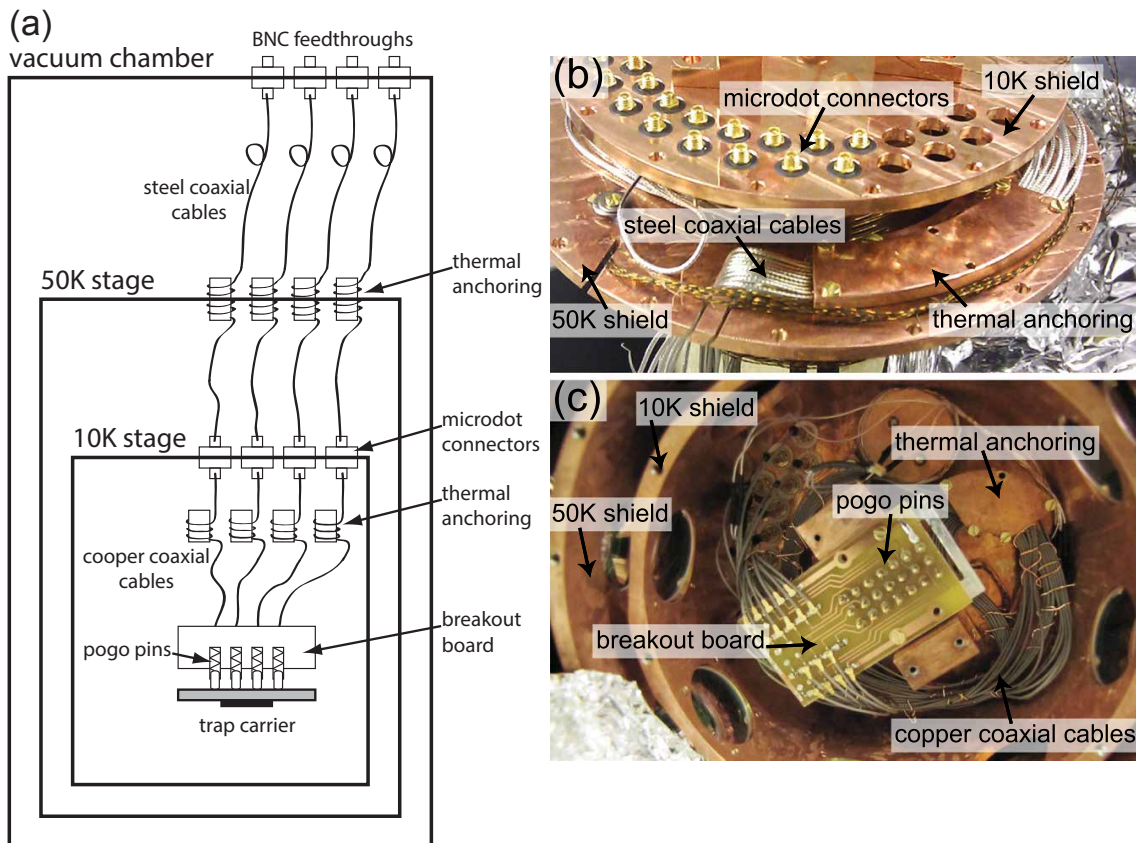


Figure 4.11: (a) Overview of the wiring in the cryogenic setup used to apply the trap voltages. (b) The steel coaxial cables are clamped to the 50 K stage (the lower copper disk shown here) by grooved copper plates to achieve a proper thermal anchoring. Microdot connectors mounted to the 10 K stage are connected to the steel coaxial cables. (c) Breakout board at the 10 K stage connecting the coaxial cables with pogo pins which, in turn, establish a connection between the trap carrier and the coaxial lines.

shroud to establish a connection to the outside world. A temperature controller²² is used to operate the sensors. It runs them at a current of $10 \mu\text{A}$ and measures the voltage drop at the sensors. To increase the measurement accuracy, a four-point configuration is used [94]. This means that two pairs of twisted-pair wires are connected to each sensor. The drive current is sent through one pair and the voltage drop is measured via the second pair. This separation eliminates all voltage drops from the measurement that occur in the wiring and the contacts.

To control the temperature of the 10 K stage, the *GMX-20* adapter is equipped with a resistive heater at the 10 K stage. The heater consists of a coil which is wrapped around the *GMX-20* and has a resistance of 50Ω . It is also connected to the temperature controller via twisted-pair wires and the D-sub feedthrough. The temperature controller can drive the heater to stabilize the temperature at the 10 K stage ($\pm 5 \text{ mK}$) and to heat it up when

²²Cryocon, Model 24 temperature controller

4.1 Cryogenic system and vacuum chamber

thawing the cryostat. Therefore, the temperature measured by the silicon diode on the trap carrier is used as the reference. LabVIEW software was written which allows remote operation of the temperature controller and a logging of the measured temperatures (see section 4.4).

4.1.5 Oven

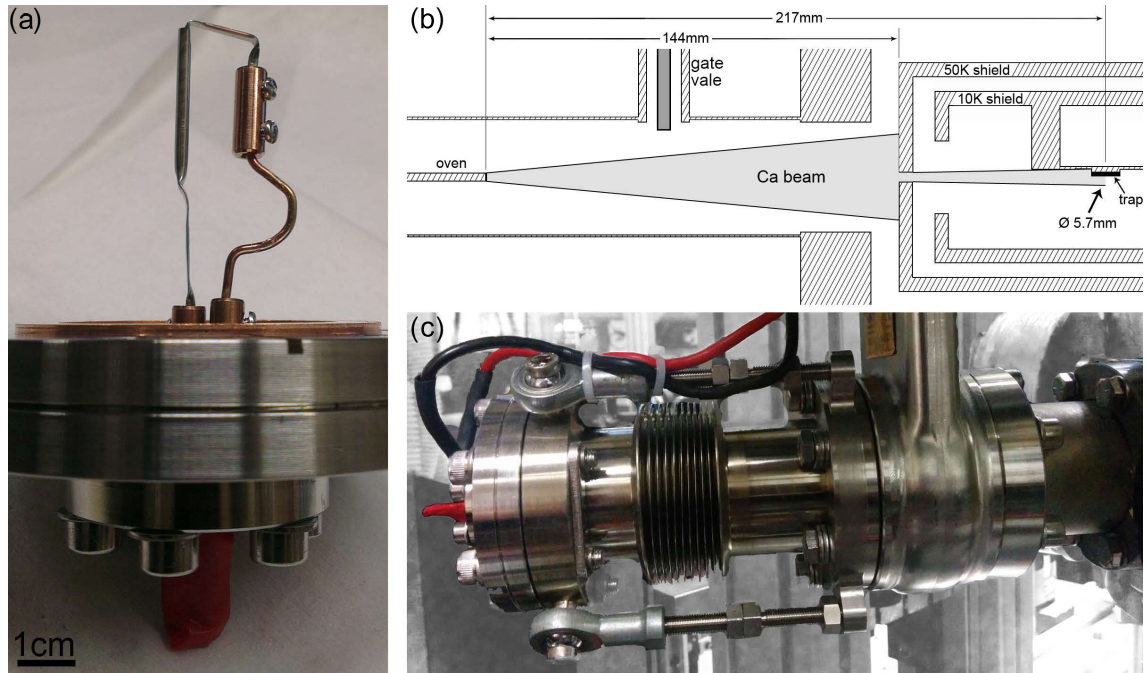


Figure 4.12: (a) ALVASOURCE 3-Ca-150-C oven. (b) Schematic of the oven setup. An aperture at the 50 K shield blocks the larger portion of the calcium beam. Only a small and well collimated part of the beam can enter the 10 K shield. (c) The oven is located in a bellow full nipple flange which allows a fine alignment of the calcium beam. A gate valve is mounted between the bellows flange and the octagon. This allows the separation of the bellow flange (including the oven) and the the main chamber.

$^{40}\text{Ca}^+$ ions are used in the ion trapping experiments in this work. This section explains how they are generated and loaded into the trap. A calcium oven creates a beam of neutral calcium atoms which are then ionized by a two-photon process [101] in the trapping region (see section 4.3.1). The oven²³ consists of a small steel tube which is filled with a calcium powder (see fig. 4.12a). To create a calcium beam a current is sent through the tube. This current heats up the tube until the calcium starts to evaporate. To avoid oxidation of the calcium in air the tube is flushed with Argon gas and sealed with a thin indium layer. The indium layer is only melted away when the oven is in vacuum. The oven is located in the vacuum chamber outside of the heat shields as shown in fig. 4.12b in

²³Alavatec, ALVASOURCE 3-Ca-150-C

order to minimize the heating of the 10 K stage when the oven is running. It is mounted on a electrical feedthrough which is connected to an adjustable bellow full nipple flange (see fig. 4.12c). The bellows which allows a fine alignment of the calcium beam after the chamber is evacuated is flanged to viewport (2) of the octagon (see fig. 4.9b). A gate valve²⁴ can be closed to separate the bellow flange from the main chamber. Thereby, the oven can be kept in vacuum when the main chamber is opened in order to replace the trap. An aperture in the 50 K shield lets a small part of the calcium beam pass through. This helps to reduce the heat load at the 10 K stage caused by the oven and prevents the interior from being covered with calcium. The oven is operated at a current between 4 A and 6 A.

4.1.6 Magnetic fields

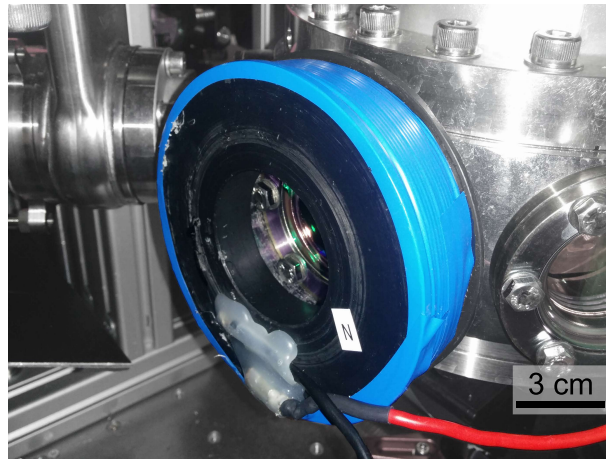


Figure 4.13: A single coil attached to one of the CF40 viewports of the octagon.

A magnetic field at the trapping site is required to split the degenerate Zeeman sublevels and define the quantisation axis of the ion (see section 2.2). This field is generated by two pairs of coils which are attached to opposite CF40 viewports of the octagon. The coil pairs are operated in Helmholtz configuration and are aligned north-south and east-west. This corresponds to the opposed viewports (3)-(7) and (1)-(5) in fig. 4.9, respectively. The coils are home-built with a diameter of 90 mm and 248 windings (see fig. 4.13)). Stable current sources designed and built by the internal electronic workshop are used to drive the coils. The magnetic field created by each pair was measured to follow this relation

$$B = 1.86 \text{ G/A} \times I, \quad (4.1)$$

with B being the magnetic field in gauss and I the current in ampere. It is worth mentioning that in this configuration it is not possible to control the magnetic field in up/down

²⁴VAT, Mini UHV gate valve 01032-CE41

4.1 Cryogenic system and vacuum chamber

direction, nor fully compensate the earth's magnetic field. This was not necessary for the measurements performed in this work. However, if a full control is required for further work an additional pair of coils can be installed.

4.1.7 Cooling down procedure

The cooling down procedure is described in this section. After installing a new trap the vacuum chamber is closed and connected to a turbomolecular pump²⁵ via the chamber valve (see fig. 4.9a). The heater (see section 4.1.4) is used to heat the 10 K stage to 320 K. This helps to remove the water in the system and speeds up the pump-down time. Higher temperatures would significantly enhance these processes but could also damage the varnishes used on the trap carrier (see section 4.2). For this reason they are avoided. At a pressure $< 10^{-4}$ mbar²⁶ the cryostat is switched on. It takes about 4 hours to achieve this pressure. However, the system is typically pumped over night to ensure good vacuum. The heater is kept running after switching on the cryostat till the temperature at the 50 K stage drops below 240 K which takes about 70 min (see fig. 4.14). In this way, water does not freeze out on the trap surface, but rather on the walls of the 50 K stage. It takes 240 min to reach a temperature below 10 K and after about 300 min the 10 K stage is at its final temperature of 6 K. This temperature is about 2 K higher than the final temperature specified by the manufacturer. The difference can be explained by the additional heat load due to the wiring and the optical viewports. The 50 K stage reaches its final temperature of 50 K after around 350 minutes.

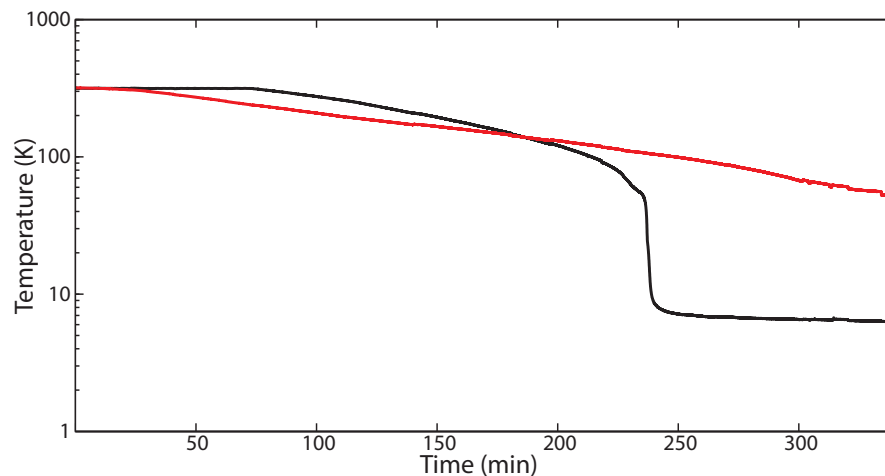


Figure 4.14: Temperature measured at the 50 K stage (red) and the 10 K stage (black) as a function of time during cool down. The heater at the 10 K stage is switched off at 70 min (when the 50 K stage reaches 240 K). The 10 K stage reaches its final temperature of 6 K after about 300 min.

²⁵Pfeiffer, HiCube Classic PM S22-33-100

²⁶This pressure is recommended by the manufacturer of the cryostat.

The pressure measured in the room temperature part of the chamber is between $5 \cdot 10^{-8}$ mbar and $1 \cdot 10^{-8}$ mbar when the cryostat is cold. As this is measured at the room temperature part of the chamber (see fig. 4.9a), it is not an accurate reflection of the pressure at the trapping site. It is complicated to directly measure the pressure inside the 10 K shield. However, due to the cryogenic pumping (see section 3.3.2) it is reasonable to assume that the pressure is lower by 3-4 orders of magnitude.

In order to change the trap, or make other adjustments to the apparatus within the chamber, the system must be brought back up to atmospheric pressure. This requires that it is also heated up to room temperature. To do this, the cryostat is switched off and the temperature controller is set to heat the 10 K stage at a rate of 2 K/min. This rate is a trade-off between a short heat-up time and avoiding damage to the setup due to thermal expansion. It takes about 145 min until the 10 K stage is back at room temperature. However, only this stage is equipped with a heater, and the thermal connection between the 10 K and 50 K stages is - by design - poor. It takes much longer for the 50 K stage to reach room temperature. To speed the thermalization up the vacuum chamber can be disconnected from the turbomolecular pump. This increases the pressure in the chamber and improves the heat transfer between the 10 K and the 50 K stage. The total heat up time of the system is about 8 hours in this case.

4.2 Trap carrier

The trap carrier is a movable and exchangeable H-shaped copper mount for the ion trap. It allows a quick and simple replacement of the traps. The RF resonator and DC filters are located on printed circuit boards (PCBs) glued²⁷ to the trap carrier. A temperature sensor is mounted on the carrier next to the trap in order to measure the temperature as close to the trap as possible. Pogo pins are used to establish a stable electric connection between the coaxial lines and the carrier, (see section 4.1.4 and fig. 4.11a). A schematic of the carrier's components (without temperature sensor) is given in fig. 4.15. Fig. 4.16 shows the trap carrier mounted in the cryostat. The installation of the trap on the carrier, the RF resonator and the DC filters are discussed in detail in the following subsections.

4.2.1 Trap installation

The general installation of the trap and its electric connection are presented in this section. Further aspects which are specific to the mounting of silica traps are discussed in section 6.1.2, while section 7.3.2 describes aspects specific to the mounting of silicon traps.

The trap is directly mounted to the H-shaped piece of copper in order to ensure a high thermal contact between the trap and the cold stage. To connect the trap to the PCBs,

²⁷Stycast 2850-FT

4.2 Trap carrier

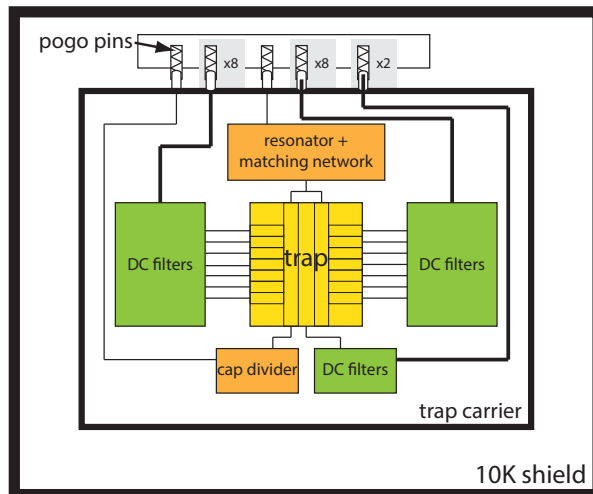


Figure 4.15: Schematic showing the trap carrier. 20 pogo pins establish the electric connections between the coaxial lines and the trap carrier. One line is used to drive the RF resonator and another one is used to measure the RF voltage via a capacitive voltage divider. 18 lines are equipped with filters and can be connected to the DC electrodes.

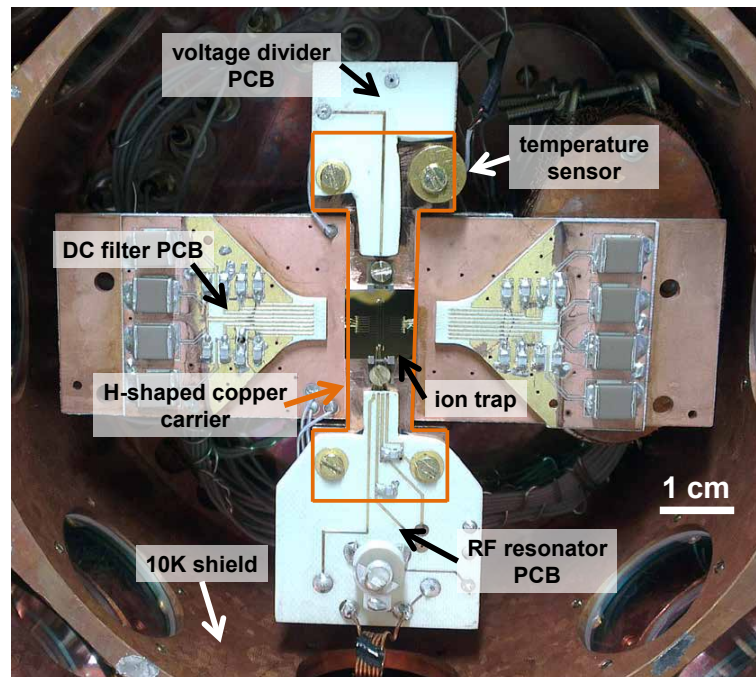


Figure 4.16: Trap carrier mounted at the 10 K stage. It consists of an H-shaped copper support (outlined in orange) and multiple PCBs (DC filters, RF resonator, voltage divider). The trap is located in the middle. The trap electrodes are connected to the PCBs via bonds. To increase the adhesion of the bonds, the PCBs are partially gold-electroplated.

gold wires with a diameter of $25\ \mu\text{m}$ are used. One end of the wires is wedge-bonded to the trap electrodes and the other one is bonded to the traces of the PCBs. It is necessary to gold-plate the traces before bonding in order to improve the adhesion between them and the wires (see fig. 4.16). Otherwise, the copper traces form a native oxide which makes the bonding difficult.

4.2.2 RF Resonator

The RF voltage used to drive the trap is provided to the system by a function generator. It is amplified by an RLC resonator located next to the trap. This allows the operation of the trap with a small RF input power ($< 100\ \text{mW}$). The basic components of the resonator are briefly discussed here. A detailed description is given elsewhere [89]. The complete RF circuit diagram is depicted in fig. 4.17.

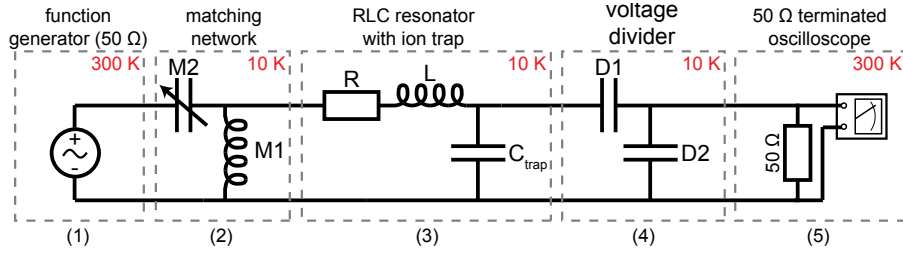


Figure 4.17: Circuit diagram of the RF resonator used to drive the trap.

The function generator located outside of the cryostat generates the RF signal (1) which is fed into the resonator via a coaxial line. The RLC resonator (3) consists of a home-built copper coil with an air (vacuum) core mounted on the resonator PCB and the ion trap. The coil provides the inductive component (L) and the ion trap provides the capacitive component (C) of the resonator. Together, L and C define the resonance frequency

$$f_0 = \frac{1}{2\pi\sqrt{LC}}. \quad (4.2)$$

The quality factor (Q) of the resonator which is a measure used to characterize its performance is defined as

$$Q = \frac{2\pi f_0 L}{R} = \frac{1}{R} \sqrt{\frac{L}{C}}, \quad (4.3)$$

where R is resonator's resistance, which mainly originates from the inductor's resistance. The quality factor is proportional to the voltage gain in the resonator. A capacitive voltage divider (4) is installed next to the trap. It is connected to an oscilloscope (5) by a coaxial line. This voltage divider enables a direct measurement of the RF voltage at the trap without affecting the capacitance of the RLC resonator.

To minimize reflections of the RF signal, it is necessary to match the impedance of the RF circuit to that of the function generator ($50\ \Omega$). This is achieved using a matching

4.2 Trap carrier

network (2) consisting of an inductor $M1$ and a capacitor $M2$. The capacitor $M2$ is tunable and can be used to fine-adjust the total impedance of the RF circuit after installing the trap carrier in the cryostat.

Resonators for resonance frequencies at 8 MHz and 20 MHz were designed and used to operate two different trap designs, called YK-1 and YK-3, respectively (see section 6.2). The resonators are depicted in fig. 4.18, and the values of their components are listed in table 4.1.

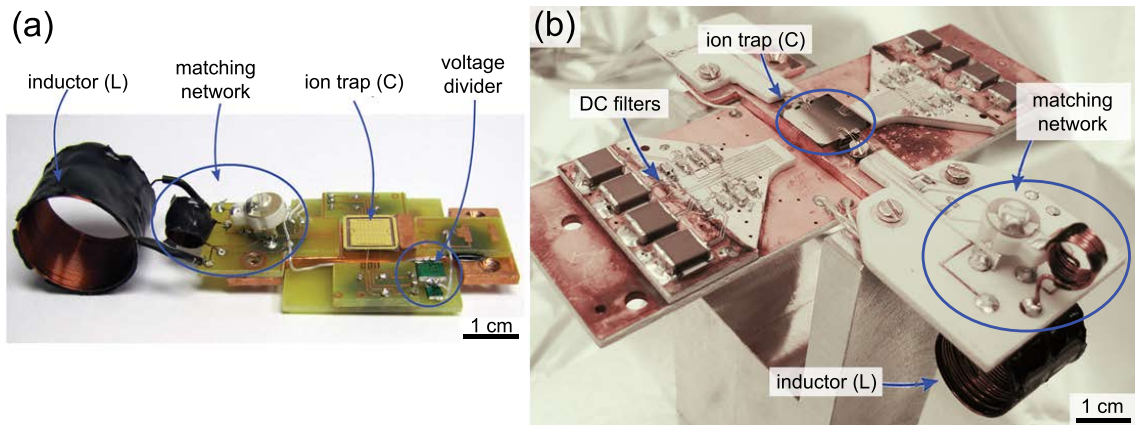


Figure 4.18: Trap carriers used for YK-1 and YK-3 equipped with traps and the RLC resonators. (a) This RLC resonator is operated at 8 MHz. The trap carrier in this design has no DC filters. (b) This RLC resonator is operated at 20 MHz.

	8 MHz resonator	20 MHz resonator
f_0 (MHz)	7.6	~ 20
Q	700	1200
L (μH)	45	6.3
C (pF)	5	7-9.5
$M1$ (pF)	12-100	12-100
$M2$ (μH)	64	168
$D1$ (pF)	5	2.4
$D2$ (pF)	1000	1000

Table 4.1: Component list of the two RLC resonator designs measured at 6 K. Different traps were operated using the 20 MHz resonator. The resonance frequency varied by a few percent for the different traps due to their different capacitances.

4.2.3 DC Filterboards

In order to carry out high-fidelity quantum operations, the ions need to be at (or close to) the motional ground state. Electric-field noise can heat the ions' motion, degrading the fidelity of operations, or making such operations entirely impossible. It is, therefore,

important to filter the DC lines in order to ensure that the ions are not unduly perturbed by noise on these lines (see section 3.2). For this reason, every DC line is equipped with an RC low-pass filter on the trap carrier. In addition, pi filters are installed on the outside of the vacuum chamber. The entire filter circuit of a single DC line is shown in fig. 4.19.

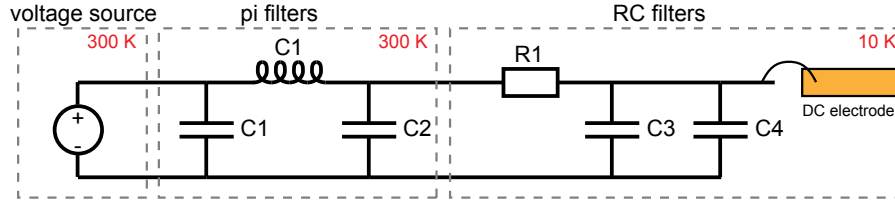


Figure 4.19: Filter circuit of a DC line. There are pi filters located outside of the vacuum chamber and RC filters on the trap carrier.

When designing the trap-carrier filters two things have to be taken into account. First, the components used have to be cryo-compatible and should not significantly change their properties during cool-down. Therefore, thin-film resistors and NP0 capacitors, which were tested to be cryo-compatible, are used. Second, in order to achieve best trapping performance, it is important that all DC electrodes are properly RF-grounded. This can be accomplished by installing capacitors as close as possible to the DC electrodes. For this reason, additional small capacitors (C4) are positioned $\sim 15\text{-}25$ mm from the electrodes. The components of the trap-carrier filters are: R1: $100\ \Omega$ ²⁸, C3: $330\ \text{nF}$ ²⁹, C4: $470\ \text{pF}$ μF ³⁰. The cut-off frequency of these filters is $4.8\ \text{kHz}$.

The components of the pi filters are: C1: $0.1\ \mu\text{F}$, L1: $470\ \mu\text{H}$, C2: $0.68\ \mu\text{F}$. The cut-off frequency of these filters is $17\ \text{kHz}$.

4.3 Optical setup

This section gives an overview of the laser systems used to create, cool and manipulate the ions. Furthermore, the setup to detect the ions and their electronic state is presented.

4.3.1 Lasers systems

There are six lasers used for the experiments with trapped $^{40}\text{Ca}^+$ ions presented in this work. Two lasers are required to ionize the neutral calcium atoms ($422\ \text{nm}$ and $375\ \text{nm}$). Two are used for Doppler cooling and detection ($397\ \text{nm}$ and $866\ \text{nm}$), and two are used in relation to the quadrupole transition ($729\ \text{nm}$ and $854\ \text{nm}$). The level scheme of the $^{40}\text{Ca}^+$ ion is given in fig. 2.2. The laser setups are briefly discussed here as is the alignment of the beams with respect to vacuum chamber (and the ion trap). A detailed description of the

²⁸VPG, Y1625100R000Q9R

²⁹Kemet, C0805C471J1GACTU

³⁰Kemet, C2220C334J1GACTU

4.3 Optical setup

ionization lasers is given in the master's thesis of R. Lechner [102], while the PhD thesis of M. Kumph describes the setups of the 397 nm, 866 nm, 854 nm lasers in detail [45]. The 729 nm laser setup is explained at full length in the PhD thesis of M. Chwalla [104].

Photoionization of calcium (422 nm, 375 nm)

To ionize neutral calcium atoms two lasers are used. The first laser drives the resonant transition $4^1S_0 - 4^1P_1$, and the second laser is required for the transition 4^1P_1 to the continuum [101].

The 422 nm light is generated in a home-built doubling cavity driven by a diode laser³¹ which is grating stabilized and runs at 844 nm. A wave meter³² is used to monitor the wavelength of this laser. The 375 nm light is provided by a free-running diode-laser³³. Both laser beams are coupled via single-mode UV-fibers to the experiment.

Cooling and detection (397 nm, 866 nm)

The dipole transition $4^2S_{1/2} - 4^2P_{1/2}$ at a wavelength of 397 nm is used to cool and detect the ions (see section 2.2). Since the ions can also decay from $4^2P_{1/2}$ into the metastable state $3^2D_{3/2}$, an additional repumping laser is required which runs at 866 nm.

397 nm light is generated in a frequency-doubling system³⁴ which consists of a diode master laser at 794 nm, a high power semiconductor tapered amplifier (TA), and a frequency-doubling stage. The 397 nm light is frequency-locked to an external reference cavity using the Pound-Drever-Hall method [103]. In order to tune the resonance frequency of the cavity, its length can be changed by piezoelectric actuators. The 397 nm light is coupled to the experimental table using a polarization-maintaining (PM) single-mode fiber. There, an acousto-optic modulator³⁵ (AOM) in double-pass configuration is installed which enables adjustment of the intensity and frequency. Furthermore, the AOM also provides a fast way to switch the laser beam on and off. The light is then sent via a PM single-mode fiber to the vacuum chamber. The alignment of the beam with respect to the chamber is described below.

866 nm light is directly created with a diode laser³⁶. The frequency of the 866 nm light is stabilized and adjusted in a manner analogous to the 397 nm light. 866 nm light is stabilized to an external reference cavity by the Pound-Drever-Hall method and a double-pass AOM³⁷ at the experimental table is used to adjust the frequency and intensity of the light. It is subsequently sent to the vacuum chamber via a PM single-mode fiber.

³¹Topitca, DL pro laser series, LD-0850-0300-4

³²High Finesse, WS-7

³³Diode: Topitca, LD-0375-0020-1; Laser mount: Thorlabs, TCLDM9

³⁴Topitca, TA-SHG pro

³⁵Brimrose, QZF-80-20-397; center frequency: 80 MHz

³⁶Topitca, DL100

³⁷Crystal Technology, AOM 3200-124; center frequency: 200 MHz

Quadrupole transition (729 nm and 854 nm)

729 nm light is needed to drive the quadrupole transition $4^2S_{1/2} - 3^2P_{5/2}$. This can be used for coherent manipulations of the ion's quantum state but also for sideband cooling and heating rate measurements (see sections 2.2 and 3.2.3). Furthermore, the repumping light at 854 nm is required for quenching the life time of the metastable $3^2D_{5/2}$ state. It pumps population from the $3^2D_{5/2}$ state to $4^2P_{1/2}$ from where the population rapidly decays to the ground state $4^2S_{1/2}$.

729 nm light used for the experiments presented in this work is provided by the 'main' laboratory³⁸ of Quantum Optics and Spectroscopy group at Innsbruck University and is sent via a 200 m long PM single-mode fiber to the 'cryo' laboratory located on the fourth floor of the same building. In the 'main' laboratory, the 729 nm light is generated by an optically pumped titanium-sapphire laser³⁹. The laser is stabilized to an external high-finesse cavity using the Pound-Drever-Hall method. Thereby, a linewidth <1 Hz on a time scale of 1 s is achieved. The light is amplified in the 'cryo' laboratory by a tapered amplifier diode laser system⁴⁰ generating an output power of up to 400 mW. The linewidth measured in the 'cryo' laboratory was about 1 kHz caused by frequency broadening due to transport in the 200 m-fiber (fiber noise). The amplified light is sent to the experimental table, where an AOM⁴¹ in single-pass configuration is used for intensity stabilization. The frequency and intensity of the beam at the ion are controlled by an AOM⁴² in double-pass configuration (located after the intensity stabilization). The radio-frequency signal used to drive this AOM is generated by the pulse sequencer box (see section 4.4). Thereby, it is possible to create phase-coherent 729 nm pulses.

854 nm light is generated by a diode laser⁴³. The optical setup is similar to the one of the 866 nm laser, including the Pound-Drever-Hall lock and the double-pass AOM configuration⁴⁴ used for controlling the intensity and frequency of the light. The 854 nm beam is overlapped with the 866 nm beam using a polarized beam splitter (PBS) before this beam is coupled to the vacuum chamber via the fiber. The alignment of these beams with respect to the chamber is described below.

Beam overlapping and alignment

The cryogenic setup is designed for rapid testing of new trap designs requiring fast turn-around times. Therefore, the beam alignment with respect to the trap should be as simple as possible. To facilitate this, all lasers beams except for 729 nm (i.e. 422 nm, 375 nm,

³⁸Viktor-Franz-Hess building, ground floor, 0/203

³⁹Coherent, 899 ring laser

⁴⁰Toptica, TA-100

⁴¹Crystal Technologies, 3080-122; center frequency: 80 MHz

⁴²Crystal Technologies, 3270-122; center frequency: 270 MHz

⁴³Toptica, DL100

⁴⁴Crystal Technology, AOM 3200-124; center frequency: 200 MHz

4.3 Optical setup

397 nm, 866 nm and 854 nm) are overlapped before being coupled into vacuum chamber. This is done using a series of notch filters, as shown in fig. 4.20. A single lens is used to focus the overlapped beams into the vacuum chamber via viewport (1). This lens is mounted on an xyz-translation stage⁴⁵ which allows a fine-adjustment of the position and the focus of the beams.

It is possible to trap ions with these overlapped beams, and they are typically used for trapping for the first time in a new trap. However, the proper focusing of the individual beams at the trap is rather challenging due to the overlapping. Poorly focused beams can cause stray light, especially in microtraps with a small ion-electrode separation. In particular, if the 397 nm beam is not well focused, the stray light can make the imaging and detection of the ion difficult. For this reason, an additional 397 nm beam was installed which is coupled via viewport (5) in to the chamber. This individual beam can be optimally focused. A flip mirror is used to switch the 397 nm light between viewport (1) and viewport (5). The 729 nm laser beam is coupled into the chamber via a different viewport (3). The typical beam diameters and powers at the trap are listed in table 4.2.

laser	viewport#	power (μW)	beam diameter FWHM (μm)
422 nm	(1)	<240	80
375 nm	(1)	<100	80
866 nm	(1)	<60	40
854 nm	(1)	<20	100
397 nm	(2)	<160	50
397 nm	(5)	<60	20
729 nm	(3)	<750	20

Table 4.2: Powers and diameters at full width half maximum (FWHM) at the ion's position for the different laser beams and viewports. The powers and spot sizes of the lasers beams were measured with the powermeter Ophir Vega and the beamprofiler Spiricon SP620U, respectively.

4.3.2 Ion detection

The fluorescence light of the ions at 397 nm (see section 2.4.3) is collected by an objective located below the vacuum chamber. The objective is custom-made with a focal length of 58 mm and NA = 0.19 [105]. It is attached to an xyz-translation stage⁴⁶ which allows a simple lateral and axial alignment. The collected light is split by a 50/50 beamsplitter⁴⁷, with one part being sent to a CCD camera⁴⁸, and the second part being detected by a

⁴⁵Laser2000, SIG-123-0144

⁴⁶Laser2000, SIG-123-0144

⁴⁷Thorlabs, BSW20

⁴⁸Andor, iXon+ A-DU897-DCS-BBB

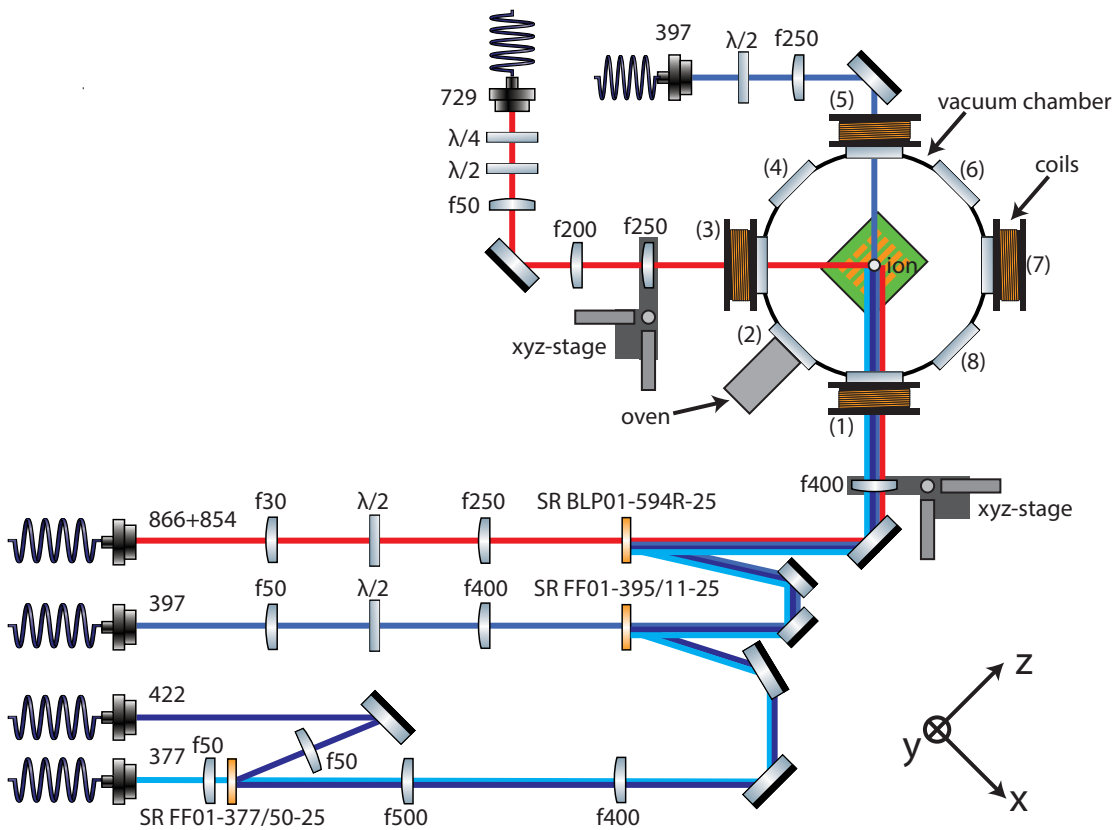


Figure 4.20: Beam alignment with respect to the vacuum chamber (as viewed from above). 422 nm, 375 nm, 397 nm, 866 nm and 854 nm beams are overlapped by Semrock (SR) filters and coupled into the chamber via viewport (1). In addition, a 397 nm beam can be also coupled into chamber via viewport (5). 729 nm light is sent through viewport (3). The coordinate system shown corresponds to the coordinate system of the trap which is mounted trapping side down in the chamber (see fig. 5.2). The calcium oven and the electromagnetic coils are also shown.

photomultiplier tube⁴⁹ (PMT). The camera and the PMT are equipped with filters⁵⁰ to suppress the detection of stray light from the other lasers and the room light. Furthermore, a slit aperture⁵¹ is located in front of the PMT to block lateral stray light. Due to the combination of filters and the aperture, a signal-to-noise ratio of more than 50 can be achieved for the ion detection with the PMT.

⁴⁹Hamamatsu, H7360-02

⁵⁰Semrock, 2x SEM-FF01-395/11-25, 1x SEM-FF01-417/60-25

⁵¹OWIS, SP40

4.4 Experimental control

The main components of the experimental setups can be controlled and operated via two personal computers (PC) which are referred to as PC1 and PC2. An overview of the controlling scheme is shown in fig. 4.21, and a detailed description is given in this section.

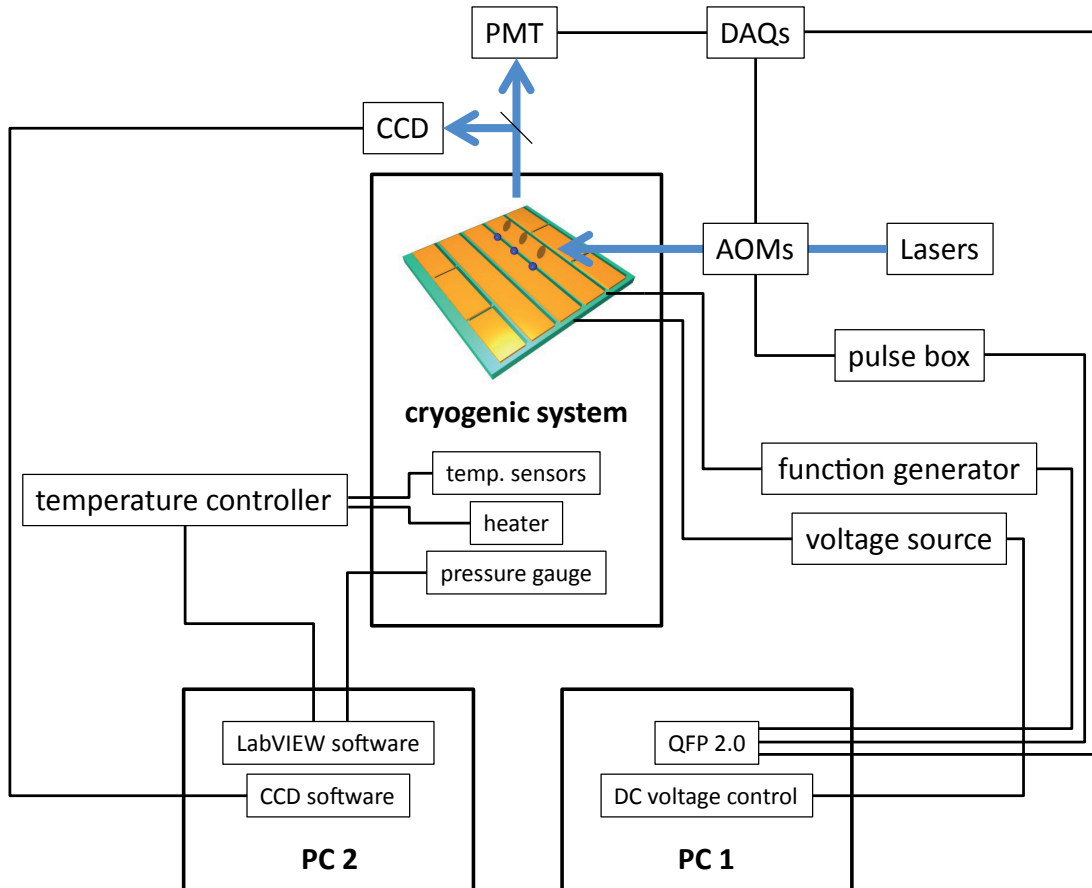


Figure 4.21: Overview of the control scheme used to operate the cryogenic ion-trap experiment.

PC1

PC1 is used to run a LabVIEW program called QFP 2.0. The program was initially written by Timo Körber, a former member of the Quantum Optics and Spectroscopy group at Innsbruck University, and was explicitly designed to control trapped ion experiments and log the experimental data. During the course of the work described in this thesis it was modified to match the special requirements of the cryogenic setup.

Three data acquisition (DAQ) cards⁵² are controlled by QFP 2.0. They provide analog

⁵²National Instruments, 2x PCI-6733, 1x PCI-6711

voltage outputs and input counters. The voltage outputs are connected to the drivers of the double-pass AOMs for the 397 nm, 854 nm, 866 nm lasers. They are used to tune the power and frequency of the laser beams. One of the counters is used to record the count rate of the PMT and forwards this data to QFP 2.0.

QFP 2.0 also controls a pulse sequencer box (pulse box) [106]. This box generates sequences of digital outputs (TTL) and RF pulses. The TTL pulses are passed on to the drivers of the 397 nm, 854 nm, 866 nm AOMs in order to switch them on and off and, thereby, turn on and off the laser beams at the ion. The RF pulses are used to directly control the double-pass AOM of the 729 nm laser. Therefore, it is also possible to change the frequency and power of the 729 nm beam by the pulse sequences. The sequences are used to realize complex measurements such as the heating rate measurement described in section 3.2.3. The sequence corresponding to this measurement is shown in fig. 3.6.

To control the RF voltage applied to the ion trap, a function generator⁵³ is used, which is in turn controlled via QFP 2.0. The voltages applied to the DC electrodes are provided by a low-noise voltage source⁵⁴. This voltage source is controlled by an additional LabVIEW program running on PC1. This software was not integrated into QFP 2.0 in order to keep the software infrastructure simple and modular. However, it communicates with QFP 2.0 and forwards data to it.

PC2

PC2 is used to log the temperature and the pressure in the cryogenic system and to run the CCD camera. A LabVIEW program running on this computer allows the remote operation of the temperature controller and a logging of the measured temperatures (see section 4.1.4). Furthermore, this software also logs the data of the pressure gauge connected to the vacuum shroud (see fig. 4.9a).

To operate the CCD camera, the standard program shipped with the camera is used. It is worth mentioning that this stand-alone program cannot communicate with any of the other control software and its data is not logged during an experiment. However, for single-ion experiments the PMT already provides all necessary data to reconstruct the ion's state and the CCD data is not required. The CCD camera is used for aligning the laser beams and the objective with respect to the trap. Furthermore, the ion and its position in the trap are monitored and a rough micromotion compensation⁵⁵ can be done with the camera (see section 2.1.1). Therefore, the RF driving power is reduced in order to make the radial trapping potential shallower which causes an additional shift of the ion's position if stray DC fields are present. The stray fields can be compensated

⁵³Marconi Instruments, 2022E

⁵⁴ISEG, EHS F205x-F-K1

⁵⁵The micromotion sidebands on the quadrupole transition are used for a more accurate compensation in a subsequent step.

4.4 Experimental control

by applying additional DC offset voltages to the trap electrodes (see section 5.2.2). This method works best for compensation parallel to the trap surface⁵⁶ but also to some extent for compensation perpendicular to it.

⁵⁶The CCD camera images the plane parallel to the trap surface.

Chapter 5

Surface trap ‘Yedikule’

All of the experiments presented in this thesis were performed in surface ion traps at cryogenic temperatures. To facilitate fair comparison of the many tests performed on different trap materials, fabrication processes, drive electronics and so forth, the geometry of the basic trap design was kept constant. This design consisted of a segmented linear surface trap, which is named ‘Yedikule’ (YK). The basic version of this trap has seven segmented DC electrodes on each side¹ and was named after the Turkish fortress and prison Yedikule Hisari which means ‘Fortress of the Seven Towers’. The fortress is located next to Istanbul and was built in 1458 (see fig. 5.1).

This chapter details the general electrode geometry of the YK traps. Furthermore, electrostatic simulations of the trap potentials are presented. The simulations are used to estimate the DC and RF voltages required for stable trapping. The trap was realized using two different fabrication processes. These are described separately in chapters 6 and 7.

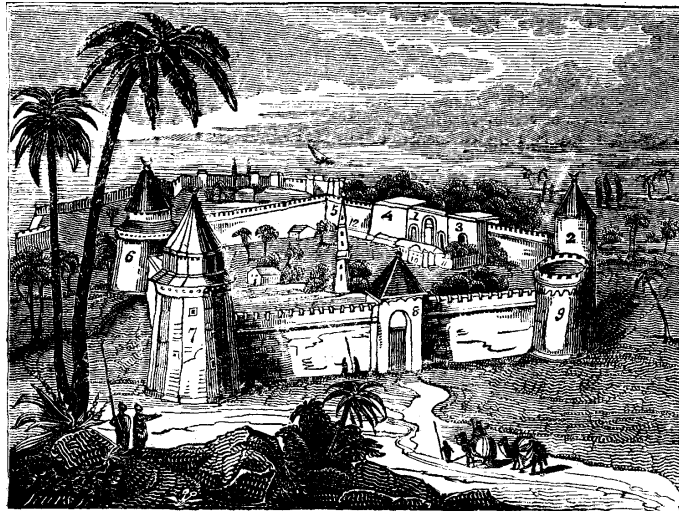


Figure 5.1: Yedikule Hisari - fortress of the seven towers (1827)

¹There also exists one version with nine segmented electrodes (see fig. 5.4)

5.1 Trap geometry

There were four versions of the YK traps, which each were variations on the same basic design. The basic electrode geometry of YK is depicted in fig. 5.2. There is one RF electrode, a center DC electrode labelled C1 and seven segmented DC electrodes on each side. The segmented electrodes on the left (right) hand side next to the RF electrode are called L1-L7 (R1-R7). The coordinate system used is also shown in fig. 5.2. The z axis is along the trap’s axial direction, parallel to the center electrode. The x axis and y axis are called radial axes. The x axis is perpendicular to the z axis and parallel to the trap surface while the y axis is perpendicular to it.

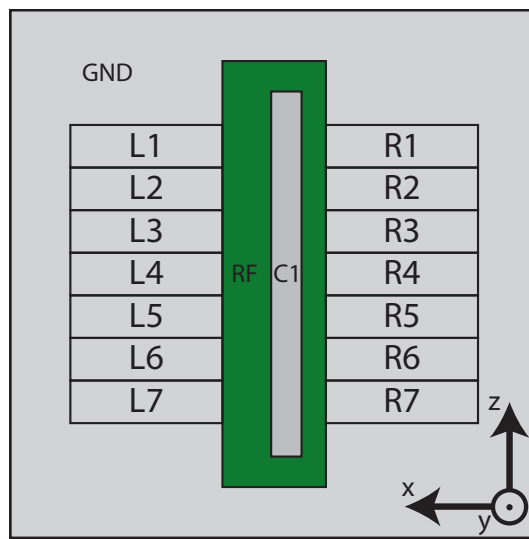


Figure 5.2: Basic electrode geometry of YK. A radial trapping pseudopotential (in the $x - y$ -plane) is set up by the RF voltage applied to the green electrode while the gray electrodes are held at RF ground. The gray electrodes support DC voltages. These DC voltages are used for confinement along the z axis and for micromotion compensation. The trap shown here has asymmetric RF electrodes which means that the radial principal axes are tilted with respect to the x and y directions.

The fact that the RF electrode is of finite length, and has bars connecting the ends of the two RF rails, produces an axial component of the pseudopotential. This leads to weak axial trapping even in the absence of DC voltages, and to a small amount of axial micromotion at most trapping positions. These effects are, however, negligible for all experiments reported in this thesis and the trap can be treated as a linear trap. If the center electrode is aligned exactly in the middle of the trap, the trap is called symmetric. If, however, it is shifted towards the $-x$ direction (as it is in fig. 5.2) the trap is referred to as an asymmetric trap. Due to the asymmetry the principal radial trapping axes are tilted with respect to the x and y directions of the trap. That allows cooling and addressing of all motional axes by laser beams aligned parallel to the surface of the trap, as explained in

5.1 Trap geometry

detail in section 3.1.2. The paths of the laser beams are illustrated in fig. 5.3. The beams are aligned parallel to the trap surface at an angle of $\pm 45^\circ$ with respect to the z axis.

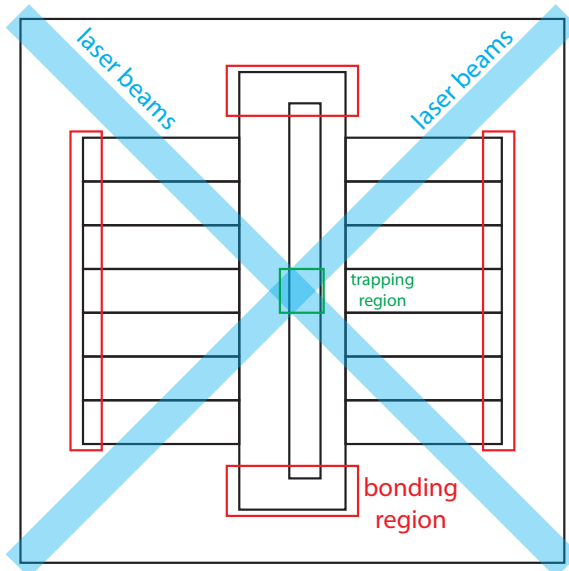


Figure 5.3: Laser paths and bonding regions in the YK traps.

Four different versions of the basic geometry were created which differ in their dimensions and symmetry. They are illustrated in fig. 5.4. The dimensions of the asymmetric trap YK-1 are given, which create a trapping region $450 \mu\text{m}$ above the trap surface. The distance between the electrodes and the trapping region is fixed - to first order - by the widths of the RF and the center electrodes. The width of these electrodes were chosen based on experience of earlier trap geometries which were known to have functioned well [19, 107]. The gap between neighboring electrodes is $20 \mu\text{m}$. YK-2 has the same dimensions, though the center electrode is centered (symmetric trap). To create YK-3 and YK-4 the dimension of YK-1 were scaled down by a factor of 2 and 2.9, respectively. In addition, YK-4 was equipped with four additional segmented electrodes. For YK-3 and YK-4, the gaps between neighboring electrodes are $10 \mu\text{m}$. The key parameters of the different versions are listed in table 5.1.

YK trap version	ion-electrode separation (μm)	# DC segments	RF electrode symmetry
1	450	7	asymmetric
2	450	7	symmetric
3	230	7	asymmetric
4	115	9	asymmetric

Table 5.1: Basic trap parameters of the four YK versions.

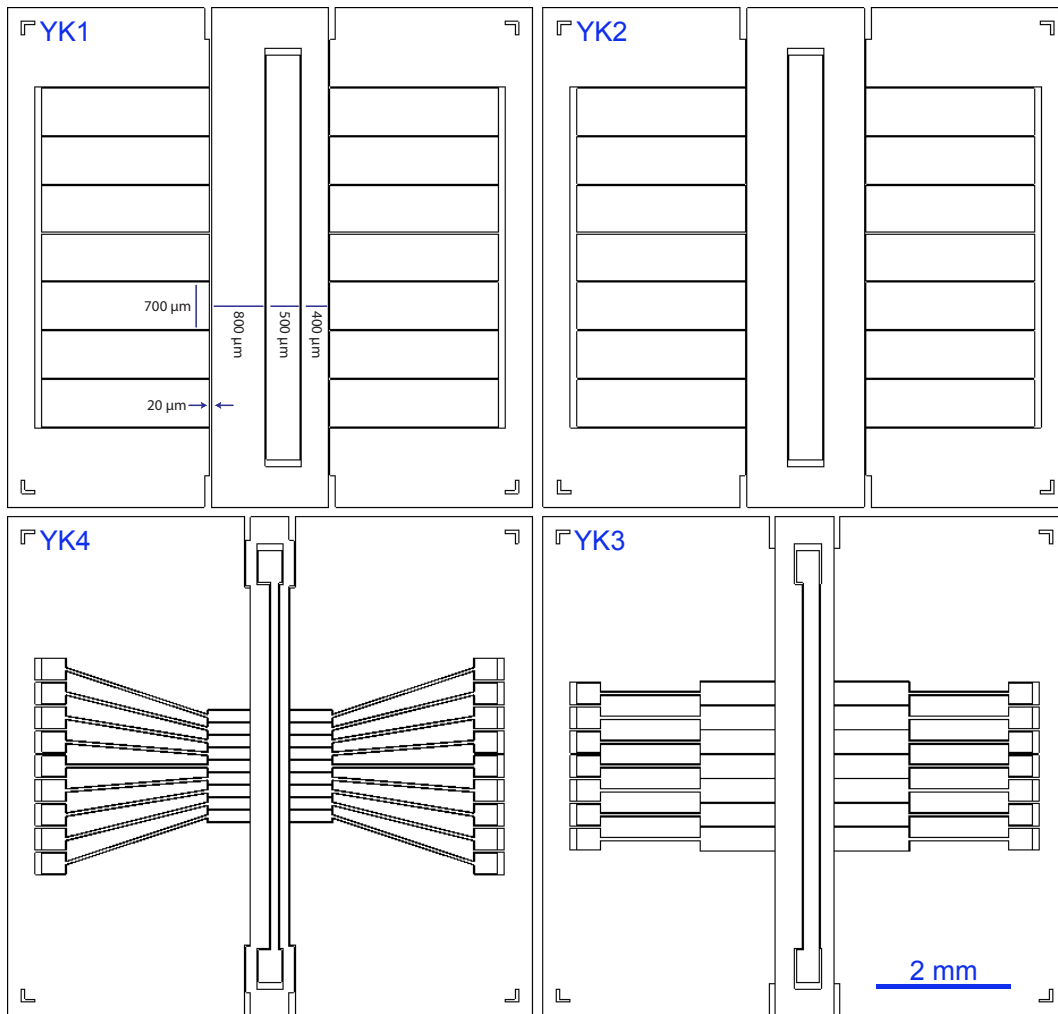


Figure 5.4: CAD drawing of the four different Yedikule designs. YK-1 dimensions are given. The DC electrodes of YK-2 are the same size as in YK-1, though in YK-2 the center electrode C1 is positioned centrally within the RF ring. To obtain YK-3 and YK-4, the width of the electrodes were scaled down by a factor of 2 and 2.9, respectively.

The individual electrodes of the YK traps are electrically connected to the trap carrier by 25 μm-diameter gold wires which are wire bonded to the outer region of the electrodes (see fig. 5.3). The dimensions of the YK-1 electrodes are sufficiently large to allow a direct bonding. The center and the segmented electrodes of YK-3 and YK-4 are equipped with additional bonding pads to facilitate the bonding.

5.2 Trap simulations

In order to operate an ion trap, it is helpful to know in advance a number of trapping parameters. The ion-electrode separation is required for the alignment of the laser beams and the ion detection system. The proper set of DC voltages and a suitable RF voltage

5.2 Trap simulations

(amplitude, V_{RF} , and frequency, Ω_{RF}) have to be applied to the electrodes to create a stable trapping potential. The RF frequency is defined by the resonance of the RF resonator and can be varied by modifying the resonator (see section 4.2.2). However, it should be considered as given for this section. In order to determine the required DC and RF voltage amplitudes the normalized electric potentials at the trapping site have to be determined first. From these potentials the relevant parameters can be deduced. There exists an analytic approach to calculate the potentials of a two-dimensional electrode configuration such as a surface trap [108]. It requires, however, some approximations: the electrodes have to fully cover an infinite plane and the gaps between the electrodes have to be zero. A more general approach to retrieve the potential is by numerical electrostatic simulations. This latter method is used in this thesis and is presented in section 5.2.1. Section 5.2.2 shows, then, how to determine the trapping parameters from the simulated potentials.

5.2.1 Electrostatic simulations

To determine the trapping parameters, the normalized electric potentials, $\Theta_i(x, y, z)$, at the trapping site created by the individual electrodes are required. The normalized potential of one electrode corresponds to the potential generated if the voltage applied to this electrode is one volt and all other electrodes are grounded. The total trapping potential can be obtained by the following equation:

$$V_{\text{total}}(x, y, z) = \sum_i \Theta_i(x, y, z)V_i + \Theta_{\text{pseudo}}(x, y, z)V_{\text{RF}}, \quad (5.1)$$

where V_i and V_{RF} are the DC and RF voltages applied to the DC and RF electrodes, respectively. The normalized potential can be directly simulated with electrostatic simulation for all DC electrodes.

To determine the normalized pseudopotential a short detour is necessary. According to eq. (2.11), the pseudopotential is proportional to the square of the electric field generated by the RF electrodes. This equation can be rewritten for the normalized pseudopotential:

$$\Theta_{\text{pseudo}}(x, y, z) = \frac{Q^2}{4m\Omega_{\text{RF}}^2} |E_{\text{RF}}(x, y, z)|^2, \quad (5.2)$$

where $E_{\text{RF}}(x, y, z)$ is the normalized electric field generated when the RF electrodes are at one volt and all DC electrodes are at zero volts. Q and m are the charge and the mass of the ion, respectively. Ω_{RF} is the RF frequency.

There exist several software packages to carry out such a simulation. The simulation software used in this thesis was COMSOL Multiphysics 3.4 in combination with MATLAB. COMSOL uses the finite element method (FEM) for obtaining approximate solutions for various physics and engineering problems. To simulate a potential, the trap electrodes are drawn in COMSOL (see fig. 5.5a) and the desired voltages are applied to them. To simulate

the normalized potentials, this is either one or zero volts. The electrodes are located inside a boundary cuboid. The potential of the cuboid’s side walls is set to zero and provides the far-off ground for the electrostatic simulations. During a real ion trapping experiment this ground is typically defined by the vacuum chamber. The space inside the cuboid is divided by a mesh, as shown in fig. 5.5b. The simulation time can be dramatically reduced without significantly decreasing the accuracy of the simulation by adjusting the meshing parameters appropriately. A fine meshing should be chosen for the region around the trapping site and the trap electrodes, whereas a coarse mesh is sufficient for the remaining part of the space. The potential at each node of the mesh is then calculated, taking into account the potential at the electrodes and the boundary cuboid. An $x - y$ -cut of the normalized pseudopotential produced by applying 1 V to the RF electrode is shown in fig. 5.5c.

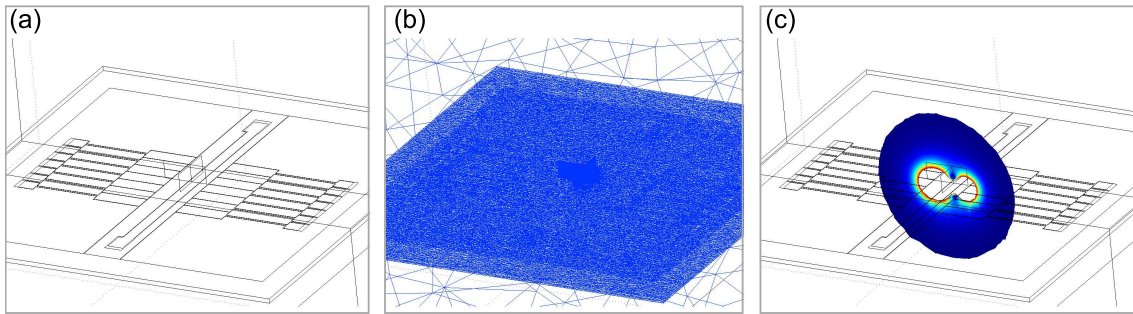


Figure 5.5: Simulation of YK-3 trap using COMSOL. (a) Geometry of the trap, (b) mesh and (c) slice through the simulated pseudopotential.

5.2.2 Trapping parameters

To calculate the trapping parameters (ion-electrode separation, efficiency parameter, RF and DC voltages, trap depth and frequencies), the simulated potentials have to be analyzed. The ion-electrode separation and the trap efficiency parameter are obtained from the normalized pseudopotential. The required RF voltage can be calculated using the ion-electrode separation and the efficiency parameters. The axial confinement of the ions is generated by the voltages applied to the DC electrodes. Furthermore, offset voltages on those electrodes are used for micromotion compensation (see section 2.1). Both can be determined from the simulated DC potentials. If all electrode voltages are identified, the total potential can be calculated using eq. (5.1). The trap frequencies and the trap depth can then be calculated from this. The procedure to extract the parameters from the simulations are explained in detail below. This can be done by a numerical computing software. MATLAB was used for that purpose in this thesis. The results of the simulation can be found in table 5.2 and table 5.3.

5.2 Trap simulations

Ion-electrode separation

The (average) position of the trapped ion is at the pseudopotential minimum if micromotion is minimised. The distance of this point to the nearest electrode is the ion-electrode separation, R_0 . The position of this minimum and thereby the value of R_0 can be determined from the simulated pseudopotential as shown in in fig. 5.6.

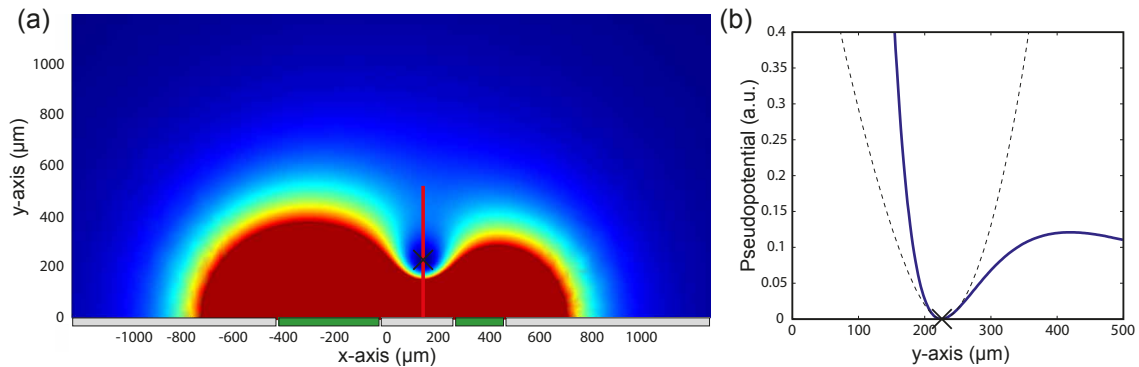


Figure 5.6: (a) Normalized pseudopotential of YK-3 simulated in COMSOL. (b) Pseudopotential along the red line. The ion-electrode separation corresponds to the distance between the electrodes at 0 and the potential minimum at $230 \mu\text{m}$ which is marked with a cross. The dashed line represents the expansion of the harmonic potential at the pseudopotential minimum. Its curvature is used to calculate the efficiency parameter.

Efficiency parameter

The efficiency parameter was introduced in section 2.1.2. It compares the trap frequency, ω'_{Ti} , of the trap being analysed with the one of the hyperbolic trap. This is indicated by eq. (2.15) which can be simplified for the normalized pseudopotential ($V_{\text{RF}} = 1$) to:

$$\epsilon_i = \sqrt{2k'_{\text{Ti}} m \frac{\Omega_{\text{RF}} R_0^2}{Q}}, \quad (5.3)$$

where $k'_{\text{Ti}} = m\omega_{\text{Ti}}^2$ [see eq. (2.2)]. k'_{Ti} is the curvature of pseudopotential in the i th direction. To determine the curvatures - and thereby the efficiency parameters - a second degree polynomial curve fitting can be performed on the simulated pseudopotential at the trapping site.

RF voltage

Stable trapping of ions in a trap is only possible for a particular range of RF voltages. To calculate the proper RF voltage eq. (2.9) can be used, which connects the RF voltage with the stability parameter, q . For any non-hyperbolic trap the efficiency parameter has to be taken into account as well. This means that q is replaced by $q' = q\epsilon$ [see eq. (2.14)]

and eq. (2.9) is rewritten to

$$V_{\text{RF}} = \frac{q\epsilon m R_0^2 \Omega_{\text{RF}}^2}{2Q}. \quad (5.4)$$

As mentioned in section 2.1.1, the stability parameter q has to be $0 < q < 0.908$. However, for the operation of the YK surface traps the best performance was obtained at values of around 0.2.

DC voltages

The DC voltages applied to the segmented electrodes provide a confinement along the z axis, and they define the radial principal axes. The pseudopotential created by the RF voltage is symmetric around its minimum in the $x - y$ plane and, therefore, the motional modes are degenerate. The symmetry is only broken by the DC potentials. Due to Laplace’s equation, eq. (2.4), the DC voltages create an anti-confinement in at least one direction in the $x - y$ plane. Typically, a static saddle potential is formed, as shown in fig. 5.7b. The DC saddle point has to overlap with the pseudopotential minimum in order to minimize the micromotion. In case the electric DC field is non-zero at the pseudopotential minimum a force is affecting the ion which moves it out of the minimum. This increases the micromotion of the ion. The DC saddle potential defines then the orientation of the radial motional axes. For asymmetric traps it is possible to rotate the DC saddle by changing DC voltages. Thereby, the radial modes can be rotated out of the trap plane which allows for a cooling and addressing of all motional modes by a laser beam parallel to the trap surface.

In order to determine the DC voltages, the DC potentials of the individual electrodes are combined in such a way to ensure an overlapping of the DC saddle with the pseudopotential minimum and an axial confinement.

DC offset voltages for micromotion compensation

Stray charges on the trap surface can cause electric fields at the trapping site. As described above, these fields shift the ion out of the pseudopotential minimum which increases the ion’s micromotion. That effect usually requires an additional DC voltage fine tuning to compensate for the stray fields and minimize the micromotion. This is done by applying offset voltages to the DC electrodes. The low symmetry of asymmetric surface traps makes this micromotion compensation rather tedious if the single voltages are iteratively changed. Instead, it would be desirable to have sets of DC voltages which provide an overall electric field with only a single, specified component (e.g. E_x) at the position of the ion.

Such sets can be calculated from the simulated DC potentials. Therefore, a multipole expansion is performed. Based on the dipole components of this expansion the required

5.2 Trap simulations

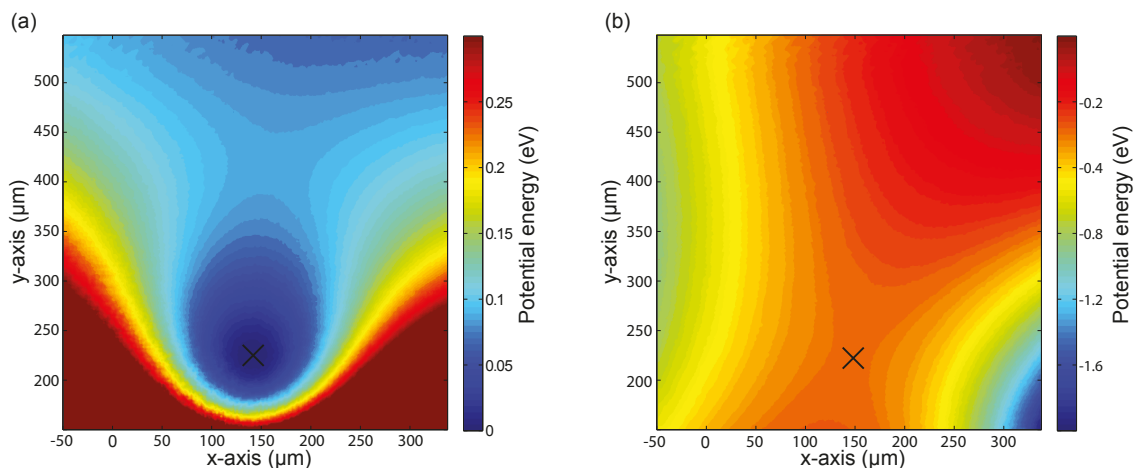


Figure 5.7: Energy potentials at the trapping region of YK-3 design in the $x - y$ plane. (a) Pseudopotential created by a RF voltage with $V_{\text{RF}} = 140 \text{ V}$ and $\Omega_{\text{RF}} = 2\pi \times 20.6 \text{ MHz}$ for a $^{40}\text{Ca}^+$ ion. (b) Saddle potential generated by the DC voltages listed in table 5.3. The DC and the RF saddle points are at the same position, marked with a cross.

voltage sets can be determined. This process is explained in detail in the master’s thesis of A. Pauli [65]. The dipole components of the YK design are listed in appendix A.1.

Trap depth and trap frequencies

After determining the DC and RF voltages applied to the electrodes, the total potential at the trapping site can be created using eq. (5.1). An example of the total potential (made from the sum of the potentials shown in fig. 5.7 is shown in fig. 5.8. The trap depth and the trap frequencies can be obtained by analyzing this potential. The trap depth is defined as the minimum energy which the ion requires to exit the trap. It corresponds to the potential energy difference between the saddle point (marked with a circle in fig. 5.8) and the pseudopotential minimum (marked with a cross in fig. 5.8). In a manner similar to the determination of the efficiency parameters, the trap frequencies can be deduced by identifying the curvatures, k'_{T_i} , of the total potential along the trap axes. Again a second degree polynomial curve fitting is used to find the curvatures. The trap frequencies can then be calculated using the equation $\omega'_{\text{T}_i} = \sqrt{k'_i/m}$.

YK trap #	drive freq. $\Omega_{\text{RF}}/2\pi$ (MHz)	ion-electrode separation (μm)	trap freq. $\omega_{\text{T}_i}/2\pi$ (MHz)	ϵ_y	RF ampl. V_{RF} (V)	trap depth (meV)
1	7.6	452	0.27	0.19	89	46
3	20.6	230	1.01	0.21	166	35

Table 5.2: Simulated trapping parameters of YK-1 and YK-3 which were used in the experiments presented in chapter 6 and chapter 7. The drive frequencies chosen correspond to the drive frequencies in the experiments.

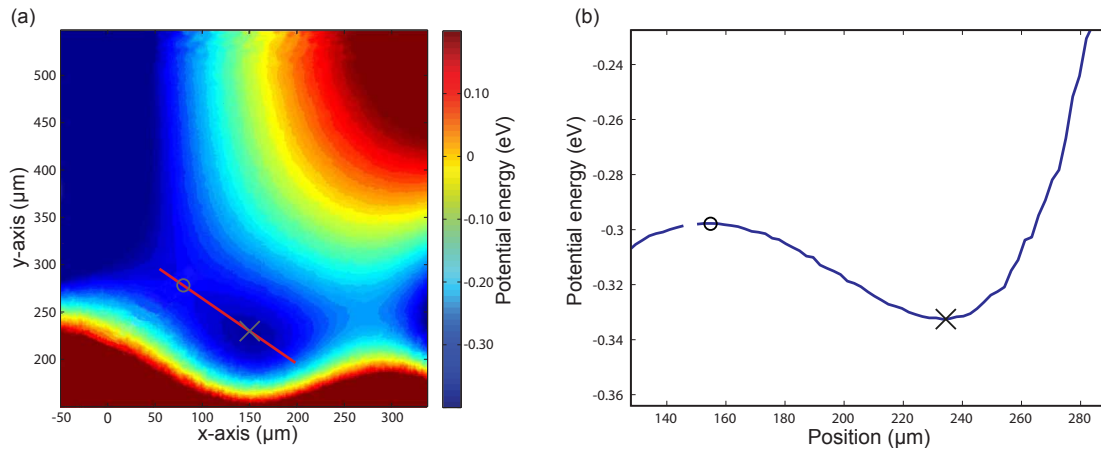


Figure 5.8: (a) Total effective potential of YK-3 in the $x - y$ plane. The potential is a combination of the RF pseudopotential and the DC potential shown in fig. 5.7. (b) Energy potential along the red line drawn in (a). The trap depth of 35 meV is the potential energy difference between the saddle point (marked with a circle) and the minimum (marked with a cross).

	DC voltage (V)	
	YK-1	YK-3
L3	0	5.4
L4	-7.6	-38
L5	0	5.4
R3	7	25.5
R4	-8.134	-29.3
R5	7	25.5
C1	-2.39	-1

Table 5.3: Simulated DC voltages. The labelling of the electrodes is defined in fig. 5.2.

Chapter 6

Silica traps

The cryogenic ion-trapping system was set up from scratch as part of the work described in this thesis. Naturally, extended testing and calibrating of the different components of the system (e.g. wiring and RF resonator, vacuum chamber and cryostat, beam alignment and detection) were necessary prior to testing new trap designs. One way to test the entire system is by the operation of a simple and known trap, for which the functionality has been previously demonstrated. Therefore, surface traps based on an established fabrication procedure [18, 19] were chosen for the first experiments. To simplify the operation, the traps had a larger ion-electrode separation than usual for cryogenic traps in other groups. The traps consisted of gold electrodes on a fused-silica substrate and were fabricated by a lift-off process. These traps are referred to throughout this thesis as *silica traps*. The geometry used for all of the traps was the Yedikule design, which was discussed in chapter 5. The fabrication of the traps is described in section 6.1. The first ion trapping experiments and trap characterizations are presented in section 6.2.

6.1 Manufacturing traps

Due to the simple fabrication of the silica traps, they could be produced in-house in our cleanroom¹ which was built as part of the work described in this thesis. This fact, and the short fabrication time of about one day for the lift-off process, made these traps especially convenient for testing the system. Both the microfabrication and the packaging were done in the cleanroom and are presented in this section.

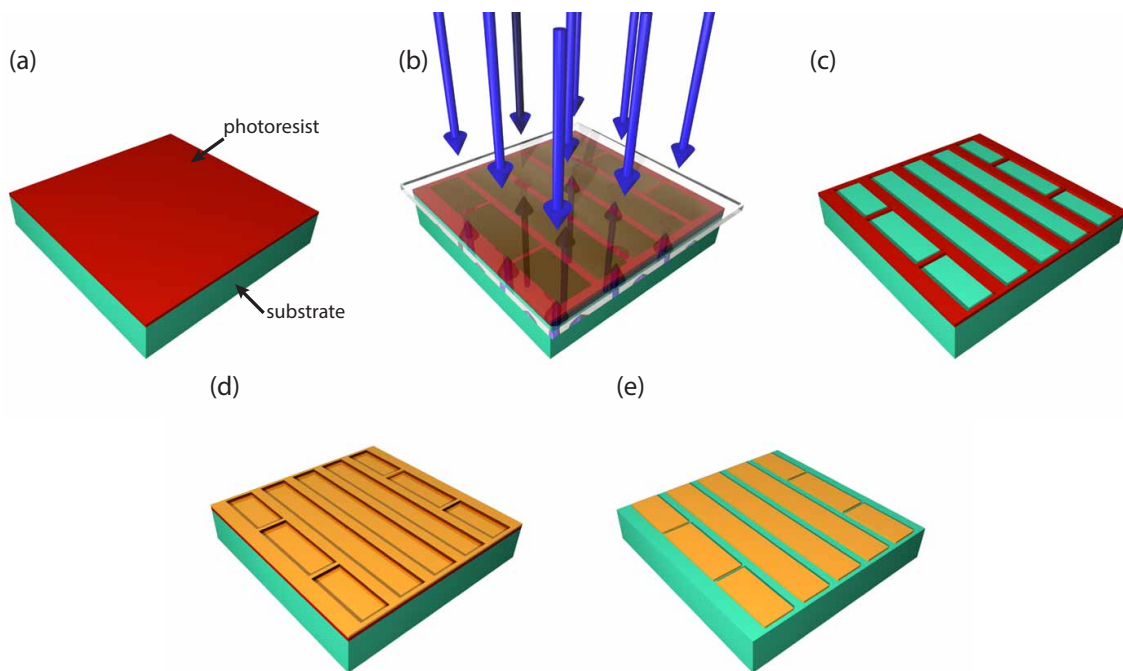


Figure 6.1: Lift-off process. (a) Spin coating, (b) UV-exposure, (c) development, (d) metal deposition, (e) lift-off.

6.1.1 Microfabrication

The main steps of the fabrication are shown in fig. 6.1. A detailed list of all steps is given in appendix B.1. The fused silica substrates² had the dimensions $10\text{ mm} \times 10\text{ mm} \times 0.5\text{ mm}$. To fabricate a trap, a single substrate is coated³ with a positive photoresist⁴ (fig. 6.1a). Using a mask aligner⁵, the trap structure is lithographically transferred from a mask⁶ to the photoresist by exposing the masked resist to UV light (fig. 6.1b). Afterwards, the photoresist is put in a developer which dissolves the exposed parts of the resist (fig. 6.1c). Titanium and gold layers are deposited by thermal evaporation onto the parts of the substrate surface which are not covered by photoresist (fig. 6.1d). The titanium layer is only a few nm thick and serves as an adhesion layer. The gold layer is typically about 500 nm thick and forms the trap electrodes. The final step is the lift-off in which the remaining photoresist and the metals on it are removed by a solvent (fig. 6.1e).

¹Viktor-Franz-Hess building, 4th floor, room 4/17; cleanroom class: ISO 4 (ISO 14644-1 cleanroom standards).

²CrysTec GmbH

³Suss, Delta 6 RC

⁴AZ 6632

⁵Suss, MJB3

⁶Compugraphics Jena GmbH

Edge bead removal

The UV exposure in the mask aligner is a contact lithography, which means that the mask is in direct contact with the photoresist. Hence, the mask structure is transferred to the photoresist with a ratio of 1:1. To achieve the best resolution in the lithography process there should be no gap between the mask and the photoresist. However, the photoresist film created by the spin coating is not completely even. Due to the squared shape of the substrates, air turbulences are created at the edges of the substrates during spin coating. These generate photoresist bumps close to the edges, as shown in fig. 6.2a.

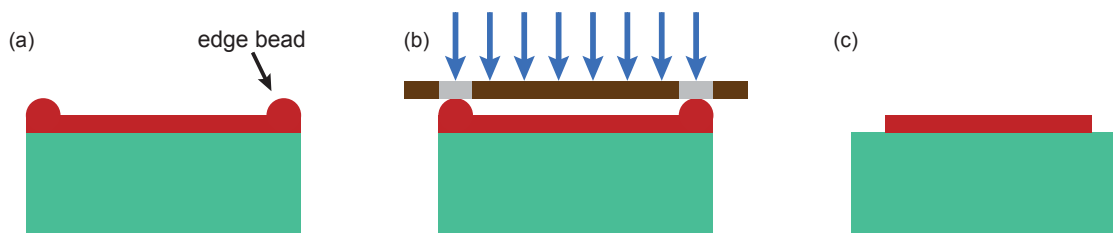


Figure 6.2: Edge bead removal. (a) Edge beads are formed close to the edges of the substrate due to effects like air turbulences during the spin coating. (b) In order to remove the edge beads, they are exposed to UV light and dissolved in a developer bath. (c) The remaining photoresist is sufficiently even for high resolution contact lithography.

The bumps are typically called edge beads. They cause a gap between mask and photoresist during the contact lithography which, in turn, leads to reduced resolution. Therefore, they have to be removed before the actual lithography step for the trap electrodes can be carried out. This is done by an additional lithography. A special mask is used which only exposes the edge beads to UV light (fig. 6.2b). The edge beads are then removed by putting the substrate in a developer bath. The remaining photoresist forms a sufficiently even film to allow contact lithography with high resolution (fig. 6.2c). Resolution tests show that structures with a width of $2\ \mu\text{m}$ can be generated after the edge bead removal (fig. 6.3).

6.1.2 Mounting and wire bonding

The silica traps are mounted on the trap carrier, as discussed in section 4.2.1. The traps are glued to the H-shaped copper mount by a varnish⁷ designed for cryogenic applications. The trap electrodes are electrically connected to the resonator and filter PCBs by $25\ \mu\text{m}$ thick gold wire-bonds. The wiring scheme is depicted in fig. 6.4.

Only three out of the seven segmented DC electrodes on each side are connected to the DC channels of the filter boards. This is sufficient for stable trapping. The other segmented electrodes are wire-bonded to the ground electrode. The reduced number of electrodes used

⁷Lakeshore, VGE-7031

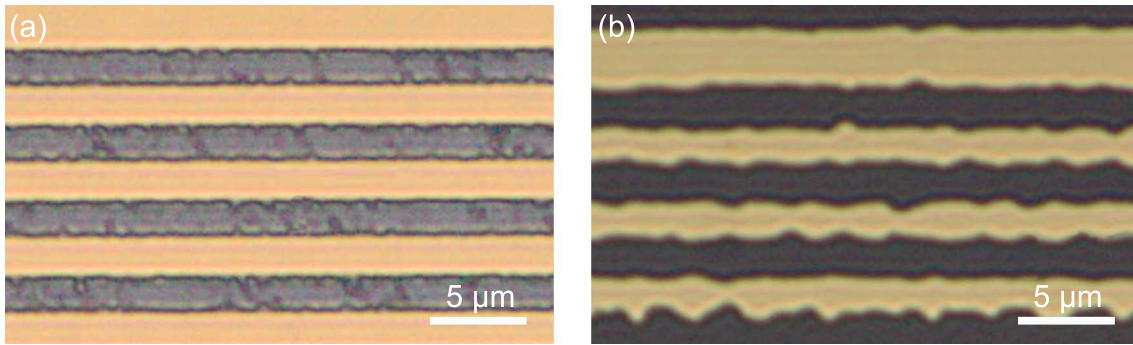


Figure 6.3: Resolution test of the optical lithography combined with edge bead removal. (a) Test mask for resolution tests consisting of $2\ \mu\text{m}$ -stripe patterns. (b) Gold structure formed on a fused silica substrate using the test mask.

allows each DC electrode in use to be connected to two DC channels. Thereby, resistivity measurements from outside the vacuum apparatus can be performed during operation in order to ensure that all lines are working faultlessly. That is especially important in cryogenic setups where different thermal expansions in the connector components used can cause open contacts on the electrical lines following cooling. The RF electrode is connected to the resonator on one side and to the voltage divider on the other side. The voltage divider provides a simple way to read out the voltage on the RF electrode without interfering with the resonator. Furthermore, it enables a way to monitor the RF line for breaks and the performance of the resonator. The voltage divider only delivers the proper signal when all connectors, wire-bonds and the resonator are working properly.

6.2 Trap performance

Two different silica trap designs (YK-1, YK-3) were tested in the cryogenic setup. The results are presented here.

6.2.1 Yedikule-1

The first trap design tested was YK-1. The ion-trap distance is rather large for a surface trap (see table 5.1 and [68]). However, this is beneficial for the initial trapping. Due to the large distance, a rather small heating rate is expected, which facilitates trapping. Furthermore, in such a large trap, stray light due to laser beams clipping the trap surface is typically negligibly small. This relaxes the requirement of tightly focused laser beams and increases the volume over which cooling can be achieved.

One disadvantage connected with larger traps is the fact that higher RF voltages are necessary to operate them. As shown in eq. (5.4), the amplitude of the RF voltage scales with the ion-electrode separation squared. An alternative to higher voltages is the use of

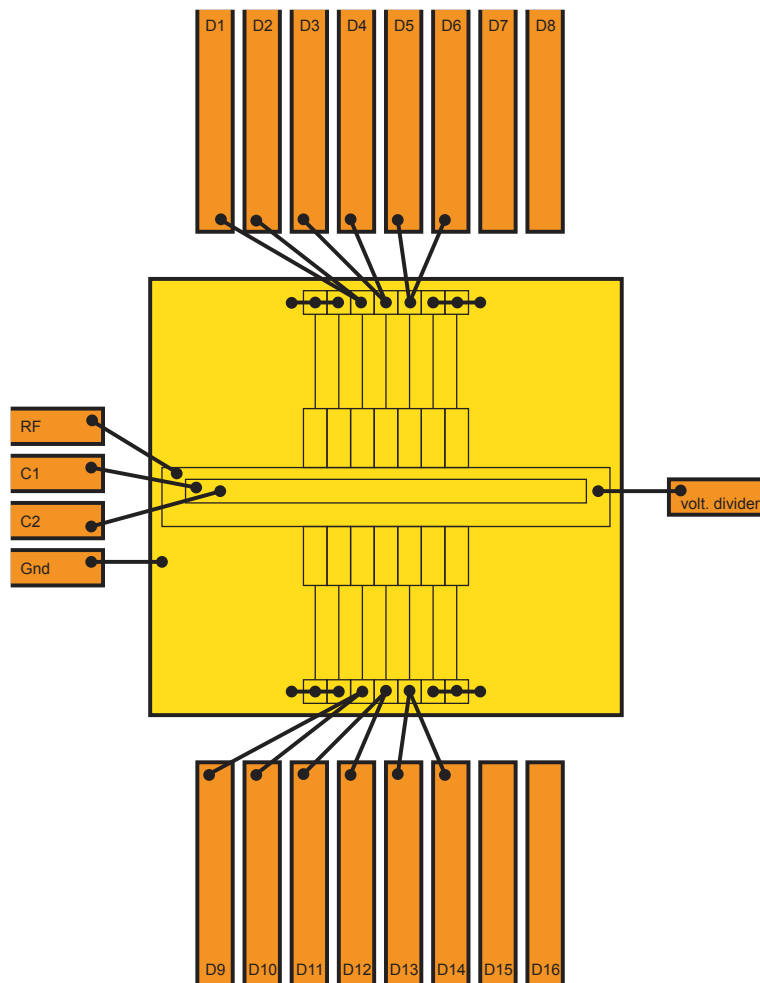


Figure 6.4: Wiring-bonding scheme. Only three segmented electrodes on each side are used for trapping. Every DC electrode (except for the ones that are shorted to ground) is connected to two lines on the PCB board. This allows testing of the DC connections by simply measuring the resistivity between the two lines.

lower RF drive frequencies. Therefore, the trap was initially driven at a RF frequency of about 8 MHz. The components of the RLC resonator are listed in table 4.1. The exact resonance frequency is 7.614 MHz. The trap can be operated at an RF voltage of about 90 V amplitude (see table 5.2). The DC voltages used are in the range $-9\text{ V} < V < +7\text{ V}$, and are listed in table 5.3.

The trap YK259 (YK-1) enabled the first successful trapping of ions in the cryogenic setup. The trap mounted on the trap carrier is shown in fig. 6.5a. Close-ups of the trap are presented in fig. 6.5b-c. $^{40}\text{Ca}^+$ ions trapped in this trap are shown in fig. 6.6.

For a more detailed characterization of the trap (e.g. spectroscopy, motional heating rate) it was necessary to individually address the quadrupole transitions. This was, however, not possible due to the low drive frequency. At a frequency of 8 MHz the side-

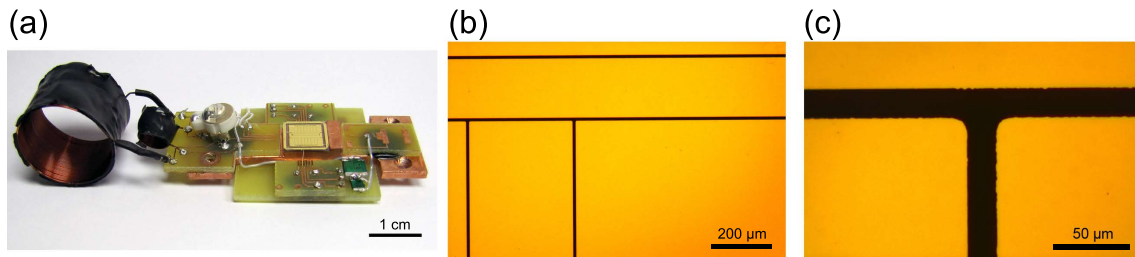


Figure 6.5: YK259 trap (YK-1) used to trap ions for the first time in the cryogenic setup. (a) The trap mounted on the trap carrier. There are no DC filters installed. A detailed description of the individual components is given in fig. 4.18a. (b)-(c) Close-up images of the trap electrodes. The yellow parts are the gold electrodes and the black stripes the silica substrate underneath.

bands caused by the micromotion overlapped significantly with the carrier transitions and precluded a proper addressing. Therefore, the resonator coil was replaced by one with a smaller inductance to increase the resonance frequency (drive frequency) to 20 MHz which provided a sufficiently large separation between the carrier transitions and their micromotion sidebands. However, the RF voltage of 650 V which was required to operate the trap was too high and damaged the electrodes. For this reason, a trap based on the YK-3 design (ion-electrode separation: 230 μm) was installed for further tests.

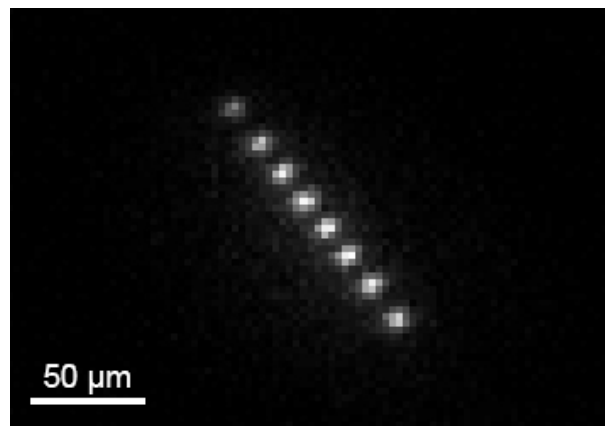


Figure 6.6: CCD images of 8 $^{40}\text{Ca}^+$ ions trapped in YK259.

6.2.2 Yedikule-3

The ion-electrode separation of the YK-3 design was 230 μm. Therefore, the RF voltage of 140-170 V required for trapping at a drive frequency of 20 MHz was sufficiently small to not damage the electrodes during operation (compare section 6.2.1). To this end, a new trap carrier was built. The components of the resonator are listed in table 4.1. Furthermore, the trap carrier was equipped with the DC filters described in section 4.2.3.

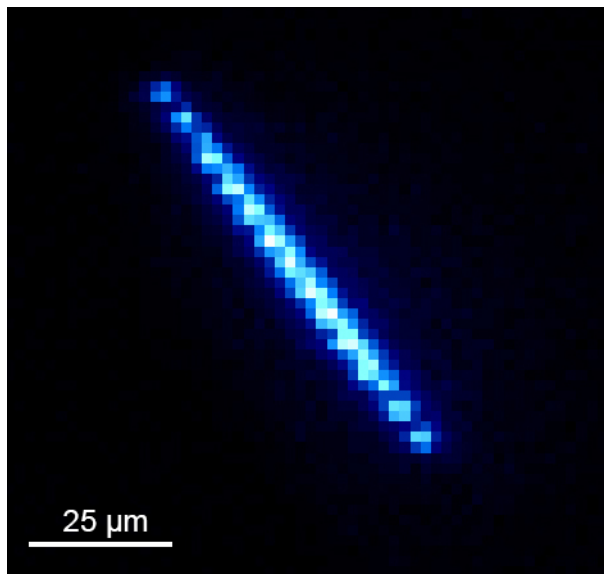


Figure 6.7: CCD images of 14 $^{40}\text{Ca}^+$ ions trapped in YK331 (YK-3).

The trap YK331 (YK-3) was successfully characterized in this setup. The exact resonance frequency of the resonator in combination with this trap was 21.451 MHz. It was operated at an RF voltage of about 140 V amplitude. The DC voltages used were in the range $-38\text{ V} < V < +26\text{ V}$, and are listed in table 5.3. A string of 14 ions held in this trap is shown in fig. 6.7. Due to the higher trap drive frequency the carrier transitions and the micromotion sidebands were well separated. This enabled the realization of heating-rate measurements based on sideband spectroscopy, as described in section 3.2.3. The motional heating of the axial mode of a single ion was investigated. The frequency of this mode was 1.069 MHz. Fig. 6.8 shows the first measurement. In total, the heating rate of this traps was measured over a period of 17 days. The results are listed in table 6.1. The trap's average heating rate is $\dot{n} = 41(5)$ phonons/s which falls well within the range of heating rates observed in other cryogenic ion traps (see fig. 3.8).

Date	Heating rate (phonons/s)
8.5.2013	39(5)
14.5.2013	37(6)
24.5.2013	47(6)

Table 6.1: Heating rates of YK331 (YK-3).

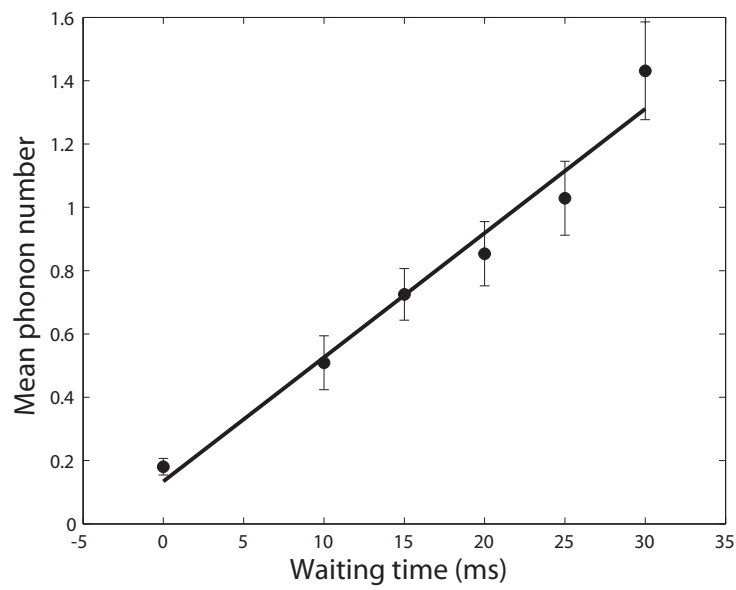


Figure 6.8: Heating-rate measurement performed on 8.5.2013. Mean phonon number \bar{n} of the axial mode ($\omega_z/2\pi = 1.069$ MHz) as a function of the waiting time after ground state cooling. \bar{n} was determined by measuring the Rabi flops on the blue sideband. In this instance the heating rate, taken to be the gradient of a linear fit to the data, was $\dot{\bar{n}} = 39(5)$ phonons/s.

Chapter 7

Silicon traps

A novel trap concept based on intrinsic (undoped) silicon is presented in this chapter. It was developed for cryogenic applications with a special focus on a very simple and reliable fabrication scheme. Section 7.1 describes the advantages of an ion trap based on a silicon substrate. It then lays out the advantages afforded by use of silicon at cryogenic temperatures, compared to room-temperature silicon traps. Trap design and manufacturing are described in sections 7.2 and 7.3, respectively. The performance of the RF resonator in combination with silicon traps is shown in section 7.4. The characterization of the trap is given in section 7.5, and possible improvements are discussed in section 7.6. The main results reported in this chapter have been published in [109].

7.1 Silicon ion traps

In principle, arrays with hundreds or thousands of surface traps could be built on a single chip [111]. However, to realize such traps, more complicated trap designs have to be developed than the one described in chapter 6. To individually address all necessary electrodes, three-dimensional interconnections consisting of multilayer structures and vias are essential. In particular, a structure is preferable where the trapping electrodes are located on the top side of the substrate and the interconnections are on the bottom side connected by through-wafer vias [110]. The well-separated conductor paths help to reduce the total capacitance of the trap. This, in turn, is important in order to achieve a high quality factor of the resonator, as well as keeping RF-induced heating to a minimum. A further aspect of realizing large trap arrays is the optical addressing of the individual ions. This can be facilitated by laser beams aligned perpendicular to the trap surface, guided through holes and slots located underneath the trapping sites.

The precise patterning of dielectric substrates like SiO_2 and sapphire is rather complicated and, consequently, these substrates are not suitable for more complex ion trap designs [111]. There exist, however, many standard fabrication technologies for silicon

patterning, which were developed by the computer and communication industries. They are called very-large-scale integration (VLSI) technologies and contain methods like optical lithography and etching. These techniques provide a fast and reproducible way of silicon patterning with sub- μm -precision. Furthermore, they facilitate a simple realization of complex ion-trap designs containing through-wafer-vias, holes for optical access and integrated electronics.

Unfortunately, there is also a drawback to using silicon as a substrate instead of dielectrics: the RF loss. It is essential that ion trap substrates have low RF losses: if the losses are too high the RF power applied in order to trap will be dissipated in the chip. This heats up the chip on the one hand and reduce the RF resonator's quality factor and gain on the other hand. The lower gain, in turn, necessitates that the RF input power has to be increased in order to achieve a sufficiently deep trapping potential. However, the higher input power heats up the trap even further.

The RF loss can be parametrized in terms of the loss tangent, $\tan \delta$. Low RF loss materials have $\tan \delta \ll 1$. For a capacitor it can be defined as the inverse of its quality factor, Q_C :

$$\tan \delta = \frac{1}{Q_C}. \quad (7.1)$$

The loss tangent of dielectrics is usually rather small. For example in the frequency range of interest for ion trap applications, the loss tangent of fused silica is around 10^{-4} and frequency-independent [112]. The consequent RF losses of an ion trap based on fused silica are sufficiently small that they can be neglected.

The RF losses of silicon are strongly frequency-dependent and orders of magnitude higher than the losses in silica at the typical drive frequencies used in ion trapping experiments. Krupka *et al.* [113] describe the physics behind loss tangents in silicon in detail. The salient points are summarized here. The loss tangent of silicon can be written as

$$\tan \delta = \tan \delta_d + \frac{\sigma}{\Omega_{\text{RF}} \epsilon_0 \epsilon_r}, \quad (7.2)$$

where Ω_{RF} is the angular RF frequency, ϵ_0 is the permittivity of the vacuum, ϵ_r and σ are the relative permittivity and the electric conductivity of silicon, respectively. $\tan \delta_d$ is the dielectric loss tangent caused by pure dielectric loss mechanisms like ionic and electronic polarization. At RF frequencies, the dominant loss mechanism of intrinsic silicon is linked to its electric conductivity, and $\tan \delta$ is mainly given by the second term of eq.(7.2). Therefore, the electric resistivity should be as large as possible (i.e. the conductivity, σ , should be as low as possible) in order to minimize the RF losses. However, even for undoped silicon with a specific resistivity larger than $5000 \Omega\text{cm}$, the loss tangent at a typical trap drive frequency of 20 MHz is still 1.5. This is far too large for a reasonable operation of the RF resonator and, therefore, precludes the direct replacement of dielectric substrates by silicon.

7.2 Silicon trap design

Despite the fact that simple, direct substitution is not possible, there exist already two different approaches that enable the use of silicon as a trap substrate. In the first approach, the issue of RF losses is mitigated by using highly doped silicon for the trap electrodes [54, 59, 114] or substrate [53]. This method is limited to room-temperature applications and would not work in a cryogenic environment because of the silicon's low electrical conductivity at low temperatures. In the second approach, an additional ground electrode is used, which shields the silicon from the trapping RF voltage [61, 81, 115, 116]. This type of trap can also be operated at cryogenic temperatures [90], though its trap design necessitates a more complicated fabrication process and precludes vias for RF electrodes. The silicon trap design presented here adopts a different approach and is especially built for low-temperature applications. Below 25 K, the charge carriers in intrinsic silicon freeze out, leaving the substrate as a good insulator with low RF losses [113]. This obviates the need for a shielding electrode, which in turn reduces the trap capacitance and the power dissipation, as well as permitting the use of a range of new fabrication techniques.

7.2 Silicon trap design

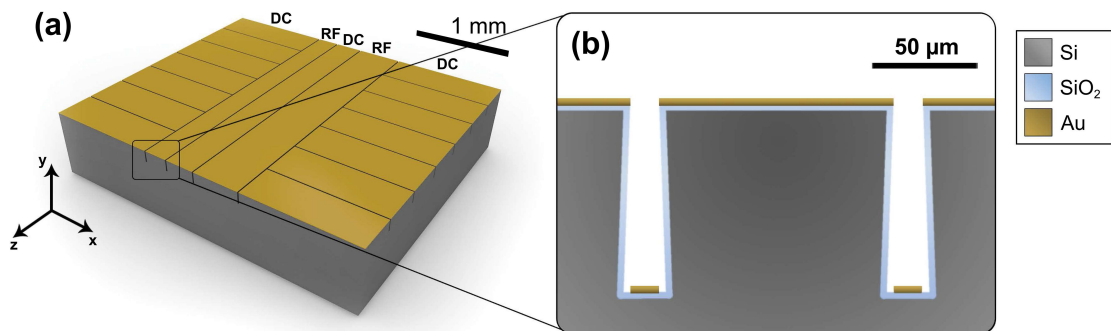


Figure 7.1: Silicon trap design. (a) Schematic showing the surface-trap design based on YK-3. This geometry allows strings of ions to be trapped $230 \mu\text{m}$ above the surface. (b) Cross section through the trap. Trenches etched to a depth of $\sim 100 \mu\text{m}$ separate the individual electrodes. The entire silicon surface is covered by a thermally grown SiO_2 layer which prevents metals from diffusing into the silicon.

A number of considerations were taken into account for developing the silicon trap design. The trap design should be suitable to scale up the number of trapped ions so that hundreds or thousands of ions can be finally trapped on a single chip. The fabrication should be simple, fast and reliable. Furthermore, any surface contamination of the electrodes induced by the fabrication should be avoided, since such contamination may cause stray electric fields which can increase the motional heating of the trapped ions (see section 3.2.1).

Based on these considerations the design shown in fig. 7.1 was developed. The electrode structure of the silicon trap is based on the YK-3 design introduced in fig. 5.4. The electrodes are made of gold. They are located on top of the silicon substrate and are separated by trenches with a width of $10\ \mu\text{m}$, a depth of $\sim 100\ \mu\text{m}$ and a slight undercut. On the one hand, the undercut trenches are necessary for the fabrication process, which is explained in section 7.3. On the other hand, the trenches help to reduce stray fields at the trapping site caused by any charges which may accumulate on the silicon surface.

A thermally grown SiO_2 layer is located between the silicon substrate and the gold electrodes. This prevents diffusion of gold into the silicon which is, anyway, assumed to be negligibly small even at the highest temperature the trap is heated to (320 K). The ground plane between the silicon substrate and the electrodes - which would be necessary for operation at room temperature - can be omitted.

7.3 Manufacturing traps

The silicon ion traps were produced in collaboration with the team of Dr. Edlinger at the advanced technical college Vorarlberg (FH Vorarlberg) in Dornbirn. Edlinger's team specializes in patterning of silicon and has the infrastructure and know-how necessary for the fabrication of complex silicon ion-trap designs. Structuring and dicing of the silicon substrates was performed at the FH Vorarlberg. Creation of the metal electrodes and packing of the trap was done in our cleanroom in Innsbruck.

7.3.1 Microfabrication

This section describes the fabrication process for the silicon traps. Further details are given in appendix B.1. Float-zone silicon wafers¹ with a diameter of 100 mm, and a thickness of $525\ \mu\text{m}$ are used. The float-zone fabrication method delivers silicon wafers with the highest purity available and, consequently, the smallest conductivity. According to the manufacturer's specification the silicon has a specific resistivity larger than $5000\ \Omega\text{cm}$. The microfabrication procedure consisting of optical lithography, etching and metal deposition is outlined in fig. 7.2. Steps (a)-(f) are performed at the FH Vorarlberg. Step (g) is done in our cleanroom.

The wafers are spin-coated to create a positive photoresist² layer with a thickness of $2.4\ \mu\text{m}$ (fig. 7.2a). The resist is exposed by UV light through a photomask to transfer the trap pattern from the mask to the resist (fig. 7.2b). Subsequently, the resist is developed to remove its exposed parts (fig. 7.2c). Deep reactive ion etching (DRIE)[117] is used to etch the trenches with slight undercuts into the silicon substrate (fig. 7.2d). The $10\ \mu\text{m}$ gaps between the electrodes are etched to a depth of $\sim 100\ \mu\text{m}$ with an undercut of $\sim 1\ \mu\text{m}$.

¹Topsil

²AZ 1518

7.3 Manufacturing traps

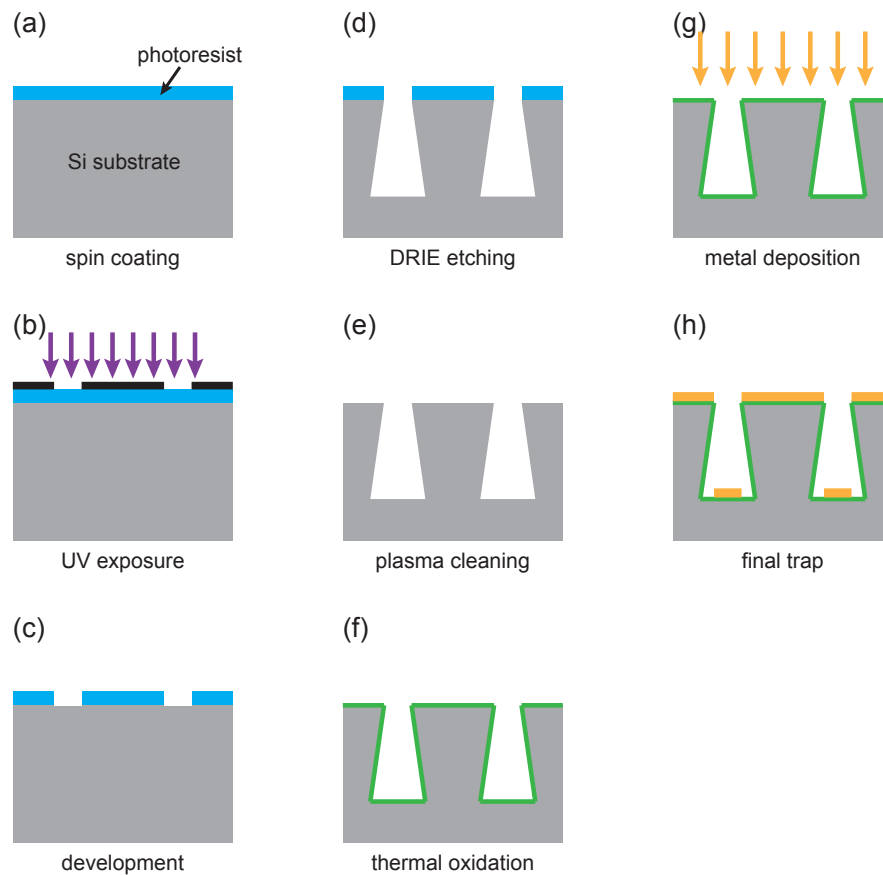


Figure 7.2: Microfabrication of the silicon trap. Steps (a)-(f) are performed at the FH Vorarlberg. Metal deposition is carried out in our cleanroom. See the main text for detailed description of the individual steps.

Details of the DRIE process are given below. The next fabrication steps are the removal of the photoresist by O₂ plasma cleaning (fig. 7.2e) and thermal oxidation of the silicon surface to grow a 2 μm thick SiO₂ layer (fig. 7.2f). The wafers, each containing 52 traps, are cut by laser scribing to separate the individual chips. The chips are then sent to Innsbruck. The actual trap electrodes are formed by metal deposition in our cleanroom (fig. 7.2g). Titanium and gold layers of a thickness of 2 nm and 500 nm respectively are deposited on the substrate surface by electron-beam evaporation. The titanium layer is necessary as an adhesion layer to avoid the gold peeling away from the silicon. The etched undercuts ensure that no electrical connections between the different electrodes are formed during the metal deposition.

Many other standard methods used to fabricate ion traps need lift-off processes [19, 47] which can potentially degrade the surface. Unlike such processes, this fabrication method does not require lift off and so does not damage the surface. There is no chemical cleaning performed after the metal deposition, and in order to avoid contamination of the surface,

the gold electrodes are never brought into contact with liquids.

Details of the DRIE process

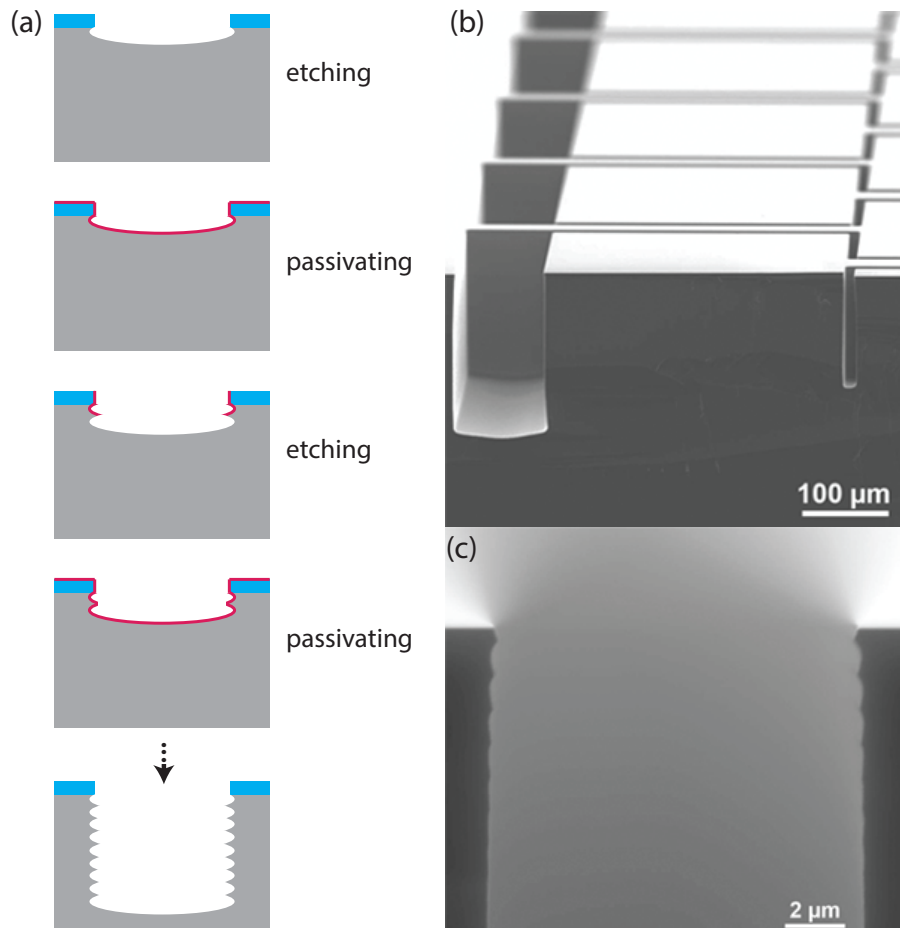


Figure 7.3: Deep reactive ion etching (DRIE). (a) The DRIE process consists of alternating etching and passivating steps. (b) SEM image of the etched silicon substrate. The bonding pads of the YK-3 design are shown. (c) SEM image of an etched trench. The undulating sidewalls are caused by the alternating etching and passivating steps of the DRIE.

The dry etching method is highly anisotropic and allows the creation of grooves and holes with high aspect ratios up to 160 [118]. It alternates between etching and passivating phases, each of which last for a few seconds (see fig. 7.3a). During the etching phase the exposed silicon is isotropically etched by an SF_6 plasma created in the DRIE machine. The SF_6 is then replaced by C_4F_8 and the second phase starts. A passivation layer is deposited from the C_4F_8 which protects the silicon surface from further etching. Directional ions are created in the plasma during the etching phase with enough energy to sputter off the passivation layers parallel to the substrate surface. This enables further etching

7.3 Manufacturing traps

perpendicular to the substrate surface and accomplishes the anisotropic component in the DRIE process. By tuning the process parameters, the side walls can either be tapered inwards, parallel or undercut. For the ion-trap fabrication undercuts are required to prevent electrical connections between the individual electrodes following the metal deposition.

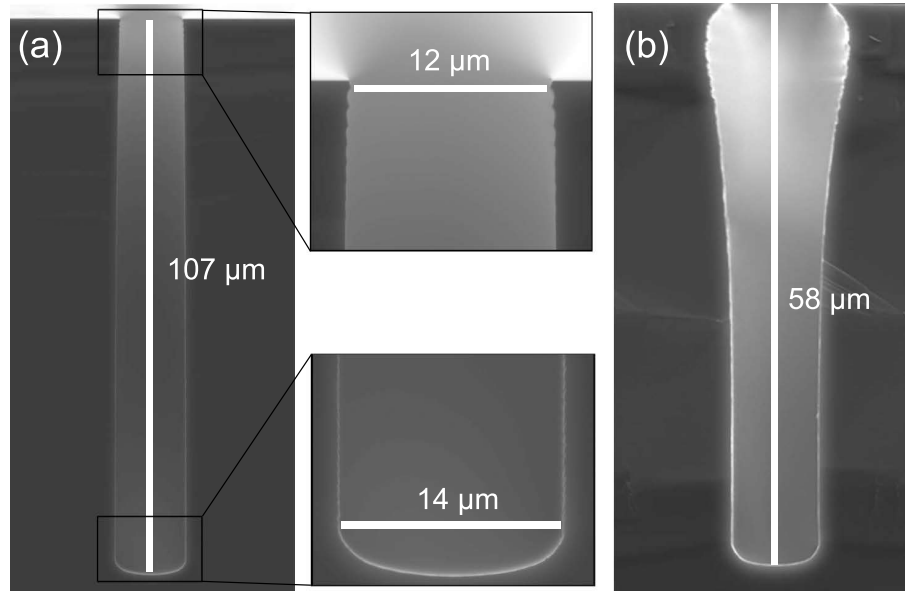


Figure 7.4: SEM images of the etched trenches. (a) Cross-section of a trench from wafer #1. The sidewalls of trench are etched with a with 1 μm -undercut. (b) The trenches of wafer #2 have a pear-shaped profile to reduce the effects caused by stray charges which can accumulate on the silicon surface.

Fig. 7.3b-c show the silicon substrate after etching. The bonding pads of the Yedikule-3 DC electrodes are shown in fig. 7.3b. The etched trenches separate the single electrodes. The etching rate depends on the width of the trenches and increases with increasing trench width. A single 10 μm -trench is displayed in fig. 7.3c. The undulating sidewalls of the trench are a typical feature of the DRIE process caused by the alternating etching and passivating steps. The ripples can be decreased at the expense of the etching rate. For the parameters used to create the trap shown here the etch rate is around 10 $\mu\text{m}/\text{min}$.

Two wafers with different etching parameters were produced at the FH Vorarlberg. The etched trench profiles of wafer #1 and #2 are illustrated in fig. 7.4a and fig. 7.4b, respectively. The trench sidewalls in wafer #1 were straight and slightly inclined forming an undercut of 1 μm for each sidewall. This ensures that no electrical shorts between two electrodes can be formed during metal deposition. The trenches of wafer #2 had an inverted pear-shaped profile. This was intended to provide better shielding of stray charges located on the trench sidewalls.

7.3.2 Mounting and wire bonding

Similarly to the SiO₂ traps, the silicon traps are mounted on the H-shaped copper carrier (see section 4.2.1). The bonding scheme discussed in section 6.1.2 is applied to these traps as well. However, gluing the trap to the copper using a varnish does not create a stable bond for the silicon substrate, due to the different coefficients of thermal expansion between copper and silicon. The relative contractions from room temperature to 4 K are 0.324% for copper and 0.022% for silicon [94]. This difference in contraction creates tension between trap and copper and finally causes the bond to break.

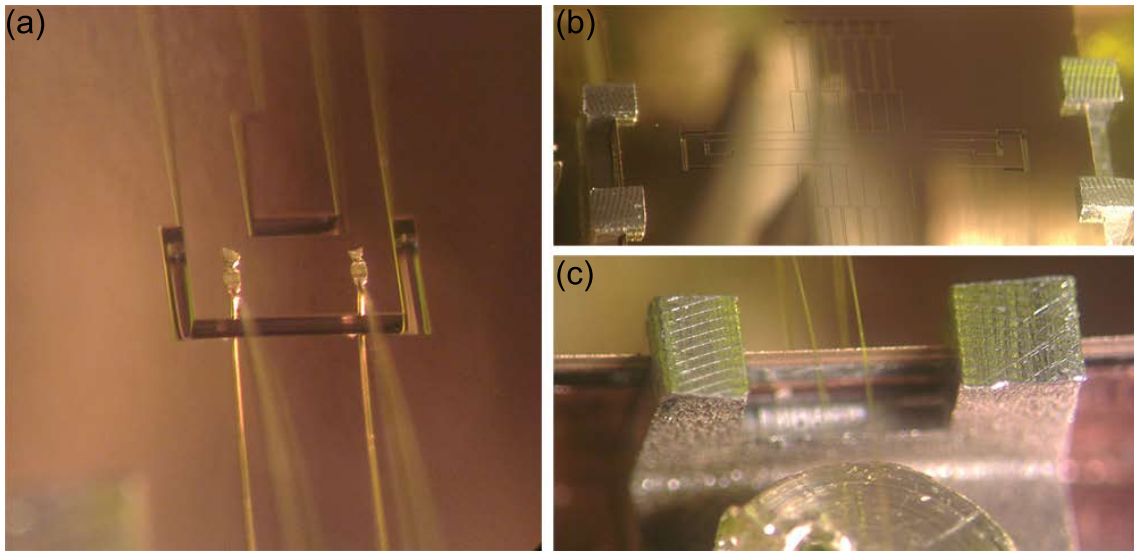


Figure 7.5: Wire-bonding of the silicon trap. (a) Image of the wire-bonded trap showing two bonds going to the RF electrode. (b) Two steel clamps are used to fix the trap to the copper carrier. (c) Detail of the clamp on the edge of the trap, with two wire bonds from the RF electrode passing between the fork of the clamp.

A more stable connection can be established by using stainless steel clamps to fix the traps (see fig. 7.5). The clamps are bolted down to the copper carrier by brass screws, thereby clamping the silicon trap. This provides a reliable mounting of the trap even over several cooling cycles. The clamping method offers further advantages over the gluing. The installation is faster, since the glue drying time of several hours is omitted. Furthermore, it is cleaner and reversible. The varnish contaminated the trap surface sometimes during the gluing and the glued bond can only be removed in an acetone bath which contaminated the trap surface. A disadvantage of the clamping is, however, that overtightening the screws can break the trap. To ensure good thermal contact between the trap and the copper carrier, the traps are coated on the backside with a thin layer of the heat-conducting grease³ before clamping.

³Apiezon N

7.4 RF Resonator performance

The performance of the RF resonator in combination with silicon traps is presented in this section. As mentioned in section 2.1.1, trapping is, in principle, possible even for a stability parameter, q , close to zero. The only limitation given by the Mathieu's differential equation is $0 < q < 0.908$. According to eq. (2.9), the RF voltage could be, therefore, close to zero as well. However, it turns out that traps, in reality, become unstable for too small q . For example, the most stable trapping in the YK traps could be achieved for q to be around 0.2 (see section 5.2.2). Furthermore, the trapping voltage is quadratically proportional to the trap depth [see eq. (2.11)]. Both aspects set a lower limit for the RF voltage which is of the order 100 V for the YK-3 design. The RF voltage provided by a function generator is typically < 10 V. Therefore, the RF resonator is used to generate the necessary voltage step-up. Consequently, the quality of the resonator is essential for the operation of the traps. If the voltage step-up of the resonator is too small, it is not possible to provide sufficient voltage to the RF electrodes, and trapping is not possible.

The resonator used in this setup is a lumped circuit RLC resonator and is described in detail in section 4.2.2. The step-up of the resonator, also called gain, G , linearly depends on the resonator's quality factor, Q , and can be written as [89]

$$G = \sqrt{\frac{R}{Z_s}} Q, \quad (7.3)$$

where R is the resistance of the inductor and Z_s is the impedance of the matched resonator, which is 50Ω in our case. The quality factor of the resonator follows the relation

$$\frac{1}{Q} = \frac{1}{Q_L} + \frac{1}{Q_C}, \quad (7.4)$$

where Q_L and Q_C are the quality factors of the inductor and the capacitor of the RLC resonator, respectively. Since the resonator's capacitance is mainly provided by the capacitance of the trap's RF electrodes, large RF losses in the silicon substrate reduce the quality factor, Q_C . This, in turn, limits Q and G .

The resonator's quality factor when used with a silicon trap was measured as a function of the temperature using an impedance analyser⁴. The resonance frequency was $\omega_0/2\pi = 20.6$ MHz. The result is shown in fig. 7.6. For this measurement, the trap temperature was slowly increased using a temperature controller and was recorded by the silicon diode mounted on the copper carrier next to the trap (see section 4.1.4). The same characteristic behavior could be observed during cool down. At room temperature the silicon substrate, which supports the RF electrodes, has a very high loss tangent of 1.5 at the resonator's resonance frequency of $\omega_0/2\pi = 20.6$ MHz [compare eq. (7.2)]. Due to the high loss tangent,

⁴AEA Technology, VIA Bravo

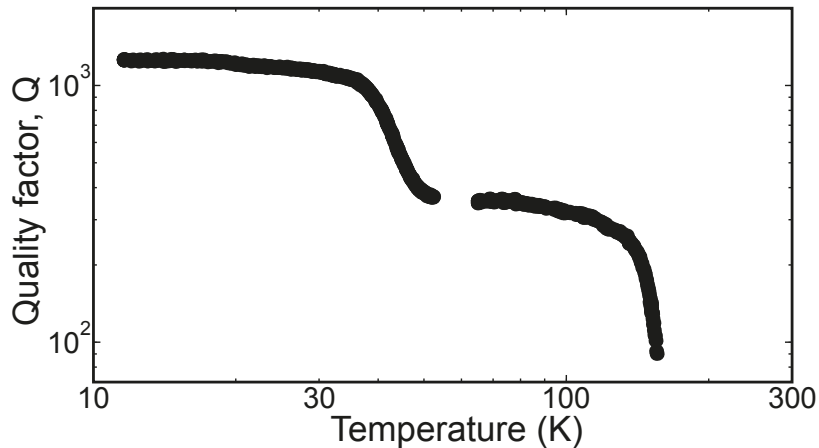


Figure 7.6: Resonator quality factor with a silicon trap attached as a function of temperature (resonance frequency of $\omega_0/2\pi = 20.6$ MHz). The inductive and capacitive parts of the resonator are predominantly provided by a copper air-coil and the trap RF electrodes, respectively. At room temperature, all of the RF driving power is absorbed by the silicon substrate and there is no measurable resonance. On cooling, the conductivity of the inductor increases (thereby increasing its quality factor, Q_L). Cooling also reduces the charge-carrier concentration in the silicon and, below 100 K, causes a step decrease of its electrical conductivity and loss tangent (thereby increasing the capacitive quality factor, Q_C). These effects all serve to increase the overall Q , with the plateau around 100 K being due to the non-linear response of the material properties. Below 20 K, the quality factor is comparable to that measured with a fused-silica trap, meaning that Q is limited by Q_L and that $Q_C \gg Q_L$. The data shown were measured in trap #1 (see table 7.1).

at room temperature all of the RF driving power is absorbed by the silicon substrate. There is no measurable resonance: the resonator Q was indistinguishable from zero. In contrast, a quality factor of 400 was measured in a similar trap fabricated on a fused-silica substrate and operated at room temperature. Cooling leads to a reduction of the charge-carrier concentration in the silicon and, below 100 K, to a steep decrease of the electrical conductivity and loss tangent. Ultimately, electron-hole pairs freeze out at ~ 25 K and the silicon becomes an insulator [113]. In addition to these changes in the silicon, the electrical conductivity of the inductor (copper coil) increases with decreasing temperature, and therefore the inductor quality factor, Q_L , goes up [89]. Increasing Q_C and Q_L leads to an increasing overall resonator quality factor, Q , with decreasing temperature. Below 20 K the value of $Q > 1200$ is comparable to that measured with a fused-silica trap at the same temperature, indicating that Q is then only limited by Q_L and not by RF absorption in the silicon.

7.5 Trap performance

To characterize the trap performance of the silicon trap design presented in this chapter the trapped ion life time and the motional heating of the trapped ions were measured. In total, six different traps from two different wafers were investigated (see table 7.1). The traps are labelled #1-6. The fabrication of the two wafers slightly differs, as discussed in section 7.3.1 and illustrated in fig. 7.4. The operation of trap #1 was characterised in detail over a period of 8 weeks. To demonstrate the reproducibility of the results, the other 5 traps were tested for shorter periods.

7.5.1 Trapped ion lifetime

A trapping parameter which becomes especially important with a large number of trapped ions is the length of time for which an ion can be trapped, sometimes called the trapped-ion lifetime. For example, assuming a mean lifetime of 1 hour which follows an exponential decay, a trap array holding 1000 ions would lose ions at a rate of around one per second.

Cooled and uncooled ion lifetimes were investigated using trap #1. With laser cooling, no ion losses were recorded over a total experimental period of more than 50 h with a single ion. To investigate uncooled lifetimes, the lasers were turned off and, after some waiting time, turned back on to see if the ion was still trapped. Waiting times of up to 9 h were used, and the ions were never lost. The trap is therefore suitable for scaling up to hundreds of ions without the need for continuous reloading. The five further traps were tested for shorter periods and the results from these traps were consistent with the more extended observations made with trap #1.

7.5.2 Heating rates

To measure the heating rate, the resolved-sideband-cooling method described in section 2.4.2 was used. Over a period of six weeks, the heating rate in trap #1 was measured several times. Fig. 7.7 shows one of those measurements. The measured heating rate were found to be constant, within the error bars, at $\dot{n} = 0.6(2)$ phonons/s. The electric-field noise inferred to underlie this heating is $S_E = 4.4 \times 10^{-15} \text{V}^2\text{m}^{-2}\text{Hz}^{-1}$ [see eq. (3.1)].

Heating rates were measured in five further traps, with the results given in table 7.1. Trap #4 exhibits a heating rate of 0.33(4) phonons/s, which is the lowest rate ever reported: the lowest previously-reported heating rates are 0.83(10) phonons/s at room temperature, in a trap with a 3.5 mm ion-electrode separation [119], and 2.1(3) phonons/s at cryogenic temperatures in an trap with a 100 μm ion-electrode separation [58]. It is worth mentioning that the traps characterized in this chapter were operated under cryogenic conditions, and $\geq 35\%$ larger than any previously fabricated cryogenic traps. When the difference in size and temperature is taken into account, the heating observed here is comparable with the best results reported elsewhere [68].

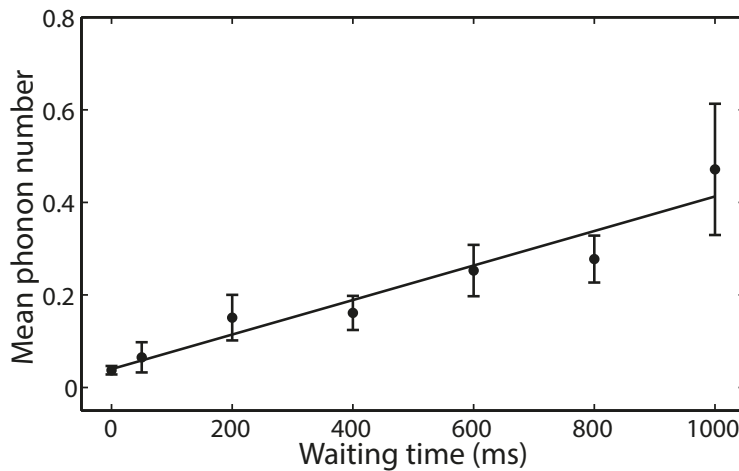


Figure 7.7: Heating-rate measurement of trap #1. Mean phonon number, \bar{n} , of the axial mode ($\omega_z/2\pi = 1.069$ MHz) as a function of the waiting time after ground state cooling. \bar{n} was determined by measuring the Rabi flops on the blue sideband. In this instance the heating rate, taken to be the gradient of a linear fit to the data, was $\dot{\bar{n}} = 0.37(6)$ phonons/s. Taking data on different days over a period of six weeks the trap exhibited a heating rate of $\dot{\bar{n}} = 0.6(2)$ phonons/s.

Trap #	Wafer #	Heating rate (phonons/s)	Axial freq. (MHz)
1	1	0.6(2)	1.069
2	1	3.3(2)	1.059
3	1	0.96(7)	1.069
4	1	0.95(7)	1.045
5	1	0.33(4)	1.066
6	2	21.5(8)	1.073

Table 7.1: Heating rates of six traps, all of the same design, with an ion-electrode separation of $230 \mu\text{m}$. Measurements were made over 84 days. Traps #1-5 were taken from wafer #1, with trap #6 being from wafer #2 (see section 7.3.1). Is it worth mentioning that the error bars given for trap #1 indicate the spread over six weeks of measurements, while the error bars for traps #2-6 indicate the uncertainty in a single heating-rate measurement.

Trap #6 exhibits a heating rate of $21.5(8)$ phonons/s. This falls well within the range of heating rates observed in other cryogenic ion traps [19, 93], but is significantly higher than the other five traps tested here. The second wafer, from which trap #6 was taken, was patterned separately from the first, using slightly modified etch parameters. It is conjectured that this may be the reason for the higher heating rate.

7.6 Trap improvements

In this section, possible improvements of the silicon trap design are presented. Light-induced charging in silicon is addressed and a possible solution is given. Furthermore, visions of the future such as the integration of optics or electronics are discussed.

7.6.1 Light-induced charging

The ion-electrode separation of the silicon traps can be, in principle, reduced without qualitative changes to the design and continuing experiments will investigate the performance of these scaled-down traps. Reducing the distance between ions and trap electrodes also means that laser beams have to be brought closer to the surface too which increases the amount of scattered light. One problem that can occur if photons hit the silicon is the creation of light-induced electron-holes [120]. The top surface area of the silicon substrate is shielded by the gold electrodes. However, the sidewalls of the trenches are uncoated and scattered light, especially of lasers close to the surface, can hit the silicon. The band-gap of silicon is 1.17 eV at 10 K which corresponds to light with a wavelength 1061 nm [121]. All lasers used in our experiments have shorter wavelengths and are, therefore, capable of creating electron-hole pairs in silicon. These pairs can have detrimental effects on the trap performance. For example, they locally increase the electrical conductivity of the silicon and consequently the RF losses. No charging effects were observed during the measurements reported in this thesis. However, later experiments in traps with a smaller ion-electrode separation (150 μm) indicated such effects may occur, though further investigation is necessary.

To avoid this effect, the sidewalls can be equipped with a protection layer of gold too. Additional, tilted gold deposition steps before or after the main deposition can partially cover the sidewalls and protect the silicon underneath (see fig. 7.8). Several tilted deposition steps at different orientations are necessary to cover all sidewalls. A rotating disc for this purpose has already been installed into the evaporation chamber. Experiments to investigate the effectiveness of such procedures are currently underway, but are beyond the scope of this thesis.

7.6.2 Visions of the future

One approach to scale up the quantum system based on ion traps is the use of a two-dimensional array of surface traps where the ions trapped in the neighboring trapping sites can interact with each other [42, 45, 122]. To generate a 2D array of trapping sites, a more complex electrode configuration is needed than the one described in this chapter. Island electrodes are usually required and vias are necessary to connect them with the bonding pads or connector interfaces. As discussed in section 7.1, through-wafer vias are particularly suitable for this purpose.

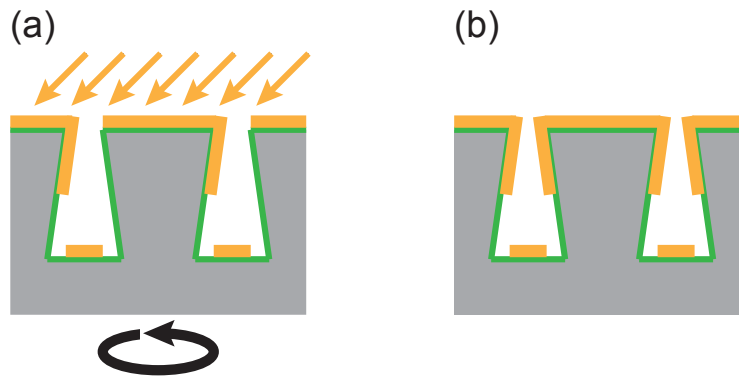


Figure 7.8: Coating the sidewalls of the trenches. (a) Tilted gold deposition is performed. (b) Tilted deposition partially covers the sideswalls with an additional gold layer which protects the silicon from scattered light.

These through-wafer-vias can be, in principle, obtained by modifying the silicon trap design based on trenches. The combination of standard fabrication processes like double-side lithography and etching or laser scribing [123] enables the creation of through-holes. The tilted metal deposition described earlier can be used to coat the sidewalls of these holes and, thereby, to establish an electric connection between the topside and backside of the trap (see fig. 7.9). This allows for connecting the traps via their backside to the outside world. In turn, bonding wires will no longer be required on the topside, where they partially block the laser access in the current designs.

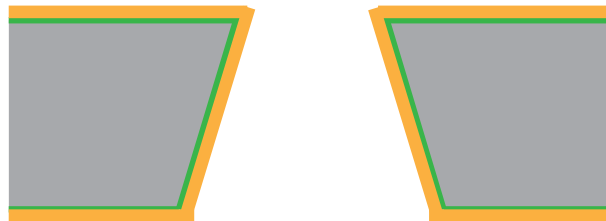


Figure 7.9: Through-wafer-vias used to connect the trap electrodes located on the topside with the bonding pads on the backside. They can be created by a combination of double-side lithography, etching and tilted metal deposition.

Furthermore, the holes can be used for single addressing of individual ions. The addressing beam can be aligned perpendicular to the surface and be directed through the holes. This technique combined with micro-lens arrays [124] would allow the addressing of hundreds or thousands of ions trapped in a 2D array.

Another aspect of the silicon substrate is the possible on-chip integration of silicon-based technologies including CMOS electronics [62]. This will enable the implementation of active electronics such as active filters and switches for the DC voltages [91]. This could, for example, help to reduce the complexity of the wiring in a cryogenic setup. At

7.6 Trap improvements

the moment, the DC voltages are generated by an external power supply (see section 4.1.4). Each DC electrode used has to be connected to this power supply by a different wire. This makes the wiring of complex traps with tens or hundreds of electrodes both tedious and challenging. However, active on-chip electronics could generate the voltages next to the electrodes and can be controlled by a single digital channel. In particular for large 2D-trap arrays, this is could be of significant benefit in controlling the individual electrodes.

Chapter 8

Conclusion

Surface traps are a promising architecture to realize a scalable quantum computer with trapped ions. In this work, a novel surface-trap design based on a silicon substrate was developed for cryogenic applications. The well-developed microfabrication and patterning methods of silicon are utilized to create a simple and reproducible ion trap with superior trapping properties.

A cryogenic apparatus was designed and built to allow trap testing at low temperatures. The system consists of a Gifford McMahon cryostat coupled to a vacuum chamber. The traps mounted in the vacuum chamber can be cooled to temperatures around 6 K. The system was designed to enable a fast exchange of surface traps and support the testing of different traps in a short amount of time. Specifically, it is possible to remove a trap, mount a new one, achieve low temperature (<6 K) and ultra-high vacuum, and trap ions in the new trap within 24 hours. In total, more than 20 traps were successfully operated in the cryogenic setup during the course of this work.

Additionally, a cleanroom was built to enable the in-house fabrication of surface ion traps. The necessary devices and machines for simple microfabrication techniques such as optical lithography and electroplating were installed and put into service. A recipe was developed to fabricate surface traps with the lift-off method.

The electrode geometry of a linear surface trap called ‘Yedikule’ was designed and simulations were performed to characterize it. There exist four different versions of the basic geometry which mainly differ in the ion-electrode separation (ranging from $115\ \mu\text{m}$ to $450\ \mu\text{m}$). Traps of the Yedikule design were fabricated in two separate ways: one based on silica, and the other based on silicon substrates.

The fabrication of the silica trap is based on a standard procedure [18, 19]. These traps were entirely fabricated in our cleanroom by means of the lift-off method and were used to test and calibrate the cryogenic setup. It was using these traps that the apparatus described in this thesis first trapped ions. Furthermore, sideband cooling of the trapped ions could be implemented and heating-rate experiments were performed. The motional

heating measured in the silica traps falls well within the range of heating rates observed in other cryogenic ion traps.

The silicon traps are fabricated using intrinsic silicon as a substrate. This has never been done with ion traps before. The use of silicon as a trap substrate at room temperature is limited due to its high RF losses. Additional ground electrodes are necessary to shield the silicon against the trap drive voltage. At cryogenic temperatures however, the RF losses in silicon are reduced and no shielding is required. In this case, silicon can be used in a similar way to dielectrics such as silica. To fabricate the traps the silicon substrate is patterned by optical lithography and deep reactive ion etching. Undercut trenches are etched in the substrate and mark the gaps between the individual electrodes. The electrodes are then formed by evaporation of gold perpendicular to the surface. Due to the undercuts, there are no electrical connections between the electrodes, and no further lift-off or etching steps - which could contaminate the electrode surface - are necessary. The traps were fabricated in a collaboration with the team of Dr. Edlinger at the FH Vorarlberg in Dornbirn which has the infrastructure and know-how required to create the undercut trenches. The silicon traps were tested and characterized in the cryogenic setup. Ions could be trapped and their life time and motional heating were investigated. Life times >9 h without lasers cooling were recorded. The measured heating rates were reproducibly low at around 1 phonon per second at a trap frequency of 1 MHz. This is the lowest heating rate ever recorded in an ion trap system.

In the future, the fabrication could be extended to include slots for increased optical access and through-wafer vias. One may ultimately envision such traps integrated with a wide variety of other silicon-based technologies including CMOS electronics, micro-optics, micro-mechanical systems, and sensors. This would ultimately mean that the entire science package including optical, mechanical, and electronic functions could be integrated on a single substrate to provide a quantum lab on a chip.

Appendix A

Trapping parameters

A.1 Multipole expansion

The micromotion compensation used is based on the multipole expansion explained in section 5.2.2 and [65]. The dipole components of the multipole expansion are used to calculate the required offset voltages in order to move an ion independently along the x , y and z axes of the trap. The definition of the axes is given in fig. 5.2. The dipole moments are obtained from analyzing the simulated potentials of the individual DC electrodes. The equation used to obtain the voltages for a movement in a certain direction is

$$\mathbf{V} = \mathbf{M} \cdot \begin{pmatrix} x \\ y \\ z \end{pmatrix}. \quad (\text{A.1})$$

\mathbf{V} is a vector describing the set of voltages to create a dipole moment along $(x, y, z)^\top$ which, in turn, moves the ions in this direction. Based on the labeling in fig. 5.2 \mathbf{V} is defined as

$$\mathbf{V} = \begin{pmatrix} C1 \\ L5 \\ L4 \\ L3 \\ R5 \\ R4 \\ R3 \end{pmatrix} \quad (\text{A.2})$$

\mathbf{M} is the matrix containing the dipole moments. It was simulated for the YK-3 design and found to be:

$$\mathbf{M}_{\text{YK-3}} = 10^{-4} \cdot \begin{pmatrix} 3.23 & 9.58 & 0.03 \\ -8.10 & -2.65 & -16.70 \\ -11.45 & -3.67 & -0.03 \\ -8.11 & -2.65 & 16.70 \\ 13.11 & 3.16 & -75.51 \\ 34.03 & 9.11 & -0.02 \\ 13.11 & 3.16 & 75.56 \end{pmatrix} \quad (\text{A.3})$$

Appendix B

Recipes for trap fabrication

B.1 Silica traps

Recipe used to fabricate the silica traps.

1. Substrate cleaning

- (a) Acetone cleaning in ultrasonic bath, 5 min.
- (b) Methanol cleaning in ultrasonic bath, 5 min.
- (c) Remove remaining contamination with cleanroom-compatible swabs and acetone.
- (d) Acetone cleaning in ultrasonic bath, 5 min.
- (e) Methanol cleaning in ultrasonic bath, 5 min.
- (f) Blow dry with N₂.
- (g) Check surface of the substrate under microscope for contamination.
- (h) Remove remaining contamination with cleanroom-compatible swabs and methanol.
- (i) Methanol cleaning in ultrasonic bath, 5 min.
- (j) Blow dry with N₂.

If necessary repeat steps g-j.

2. Spin cleaning

Further cleaning step for improved cleanliness

- (a) Do spin coating and prebake (see next step: *Spin coating*).
- (b) Rinse substrate with acetone.
- (c) Acetone cleaning in ultrasonic bath, 5 min.
- (d) Methanol cleaning in ultrasonic bath, 5 min.

3. Spin coating

- (a) Switch on vacuum pump.
- (b) Use *Suss Delta 6 RC* spin coater.
- (c) Fill a 1 ml syringe (without a needle) with ~ 0.5 ml of photoresist *AZ 6632*, very slowly. Close the photoresist bottle.
- (d) Place the syringe over a tissue and carefully drop the first 2 drops of photoresist.
- (e) Place substrate centered on the chuck of the spin coater. Close spin coater cover.
- (f) Open vacuum valve of the spin coater.
- (g) Check spin-coater pressure gauge. Pressure should go down to about -0.8 bar.
- (h) Set spin-coater parameters to 4000 rpm, 60 s, ramp: 8.
- (i) Place syringe exactly over the center of the substrate. The distance between the syringe and the substrate should be smaller than 5 mm.
- (j) Push the syringe until $3/4$ of the substrate is covered. (Never store photoresist in the syringe for more than 5 min. Always use a new one.)
- (k) Turn the spin coater on instantly.
- (l) Prebake the substrate on a hotplate set to 110°C for 50 s.
- (m) Check the resist under the microscope. If there are still lots of bubbles or parts of the substrate not covered with resist, go back to step 2b.

4. Edge bead removal

- (a) Use the mask aligner *MJB3* and the edge-bead-removal mask.
- (b) Before using the mask, clean it with a tissue and acetone.
- (c) Align the substrate centered with respect to the mask.
- (d) Expose photoresist for 90 s.
- (e) Develop photoresist for 30 s in developer *AZ 726MIF*. (Shake the substrate vigorously during the development.)
- (f) Rinse the substrate instantly with water in water bath for 20 s.
- (g) Immediately after rinsing blow dry with N_2 . (If you wait too long contaminants remain on the surface.)

5. Exposure

- (a) Use the mask aligner *MJB3* and the trap-design mask of your choice.
- (b) Before using the mask, clean it with a tissue and acetone.

B.1 Silica traps

- (c) Align the substrate centered with respect to the mask.
- (d) Develop photoresist for 30 s in developer *AZ 726MIF*. (Shake the substrate vigorously during the development.)
- (e) Rinse the substrate instantly with water in water bath for 20 s.
- (f) Immediately after rinsing blow dry with N₂. (If you wait too long contaminants remain on the surface.)
- (g) Postbake the substrate on a hotplate set to 110 °C for 50 s.

6. Evaporation

- (a) Mount substrates on substrate holder.
- (b) Blow off the contaminants from the substrates with N₂ to remove contaminations.
- (c) Install the substrate holder in the evaporation chamber.
- (d) Close the chamber and switch on the pumps.
- (e) Wait for a pressure $< 2 \cdot 10^{-6}$ mbar. (It takes about 2 h.)
- (f) Evaporate Ti (thickness: 2 nm, rate: 1 Å/s).
- (g) Wait 1 min.
- (h) Evaporate Au (thickness: 50-500 nm, rate: 1 Å/s).
- (i) Wait 15 min.
- (j) Switch off the pumps and wait till the chamber opens.
- (k) Demount the substrates.

7. Lift-off

- (a) Cup used for the lift off has to be cleaned every time before lift off (rinse with water, acetone in ultrasonic bath).
- (b) Lift off in acetone (ultrasonic bath, 100 s).
- (c) Rinse the substrate instantly with water in water bath for > 30 s.
- (d) Immediately after rinsing blow dry with N₂. If you wait too long contaminants or gold particles remain on the surface.)
- (e) Methanol cleaning in ultrasonic bath, 5 min.
- (f) Blow dry with N₂.

B.2 Silicon traps

Recipe used to fabricate the silicon traps. The fabrication was partly done in Vorarlberg and partly Innsbruck. The Vorarlberg part is explained in section 7.3. Here, the fabrication performed in Innsbruck is listed in detail including the metal deposition.

1. Substrate cleaning
 - (a) Substrates are delivered covered with a protection foil. Carefully remove the foil with tweezers.
 - (b) Acetone cleaning in ultrasonic bath, 5 min.
 - (c) Methanol cleaning in ultrasonic bath, 5 min.
 - (d) Blow dry with N₂.

2. Evaporation
 - (a) Mount substrates on substrate holder.
 - (b) Blow off contaminants from the substrates with N₂ to remove contaminations.
 - (c) Install the substrate holder in the evaporation chamber.
 - (d) Close the chamber and switch on the pumps.
 - (e) Wait for a pressure $< 2 \cdot 10^{-6}$ mbar. (It takes about 2 h.)
 - (f) Evaporate Ti (thickness: 2 nm, rate: 1 Å/s).
 - (g) Wait 1 min.
 - (h) Evaporate Au (thickness: 50-500 nm, rate: 1 Å/s).
 - (i) Wait 15 min.
 - (j) Switch off the pumps and wait till the chamber opens.
 - (k) Demount the substrates.

Bibliography

- [1] Lilienfeld, J. E. Method and apparatus for controlling electric currents. Patent US 1745175 (1930).
- [2] Heil, O. Improvements in or relating to electrical amplifiers and other control arrangements and devices. Patent GB 439457 (1935).
- [3] Bardeen, J. & Brattain, W. H. - The transistor, a semi-conductor triode. *Phys. Rev.* **74**, 230–231 (1948).
- [4] Achuthan, M. K. & Bhat, K. N. - *Fundamentals of Semiconductor Devices* (Tata McGraw-Hill, 2007).
- [5] Moore, G. - *Understanding Moore's Law: Four Decades of Innovation* (Chemical Heritage Foundation, 2006), 1. edn.
- [6] Intel. - Newest Microarchitecture and 14 Nanometer Manufacturing Process Technical Details. *Intel newsroom* (2014).
- [7] Ross, R. J. - *Microelectronics Failure Analysis* (ASM International, 2011).
- [8] Feynman, R. P. - Simulating physics with computers. *International Journal of Theoretical Physics* **21**, 467–488 (1982).
- [9] Benioff, P. - Quantum mechanical models of turing machines that dissipate no energy. *Phys. Rev. Lett.* **48**, 1581–1585 (1982).
- [10] Nielsen, M. A. & Chuang, I. L. - *Quantum Computation and Quantum Information* (Cambridge University Press, 2000).
- [11] Shor, P. - Algorithms for quantum computation: discrete logarithms and factoring. In *Foundations of Computer Science, 1994 Proceedings., 35th Annual Symposium on*, 124–134 (1994).
- [12] Grover, L. K. - A fast quantum mechanical algorithm for database search. In *Proceedings of the Twenty-eighth Annual ACM Symposium on Theory of Computing*, STOC '96, 212–219 (ACM, New York, NY, USA, 1996).

-
- [13] DiVincenzo, D. P. - The Physical Implementation of Quantum Computation. *Fortschritte der Physik* **48**, 771–783 (2000).
- [14] Ladd, T. D. *et al.* - Quantum computers. *Nature* **464**, 45–53 (2010).
- [15] Zoller, P. *et al.* - Quantum information processing and communication. *The European Physical Journal D* **36**, 203–228 (2005).
- [16] Major, F. G., Gheorghe, V. N. & Werth, G. - *Charged Particle Traps* (Springer-Verlag, 2005).
- [17] Blatt, R. & Wineland, D. - Entangled states of trapped atomic ions. *Nature* **453**, 1008–15 (2008).
- [18] Seidelin, S. *et al.* - Microfabricated Surface-Electrode Ion Trap for Scalable Quantum Information Processing. *Phys. Rev. Lett.* **96**, 253003 (2006).
- [19] Labaziewicz, J. *et al.* - Suppression of Heating Rates in Cryogenic Surface-Electrode Ion Traps. *Phys. Rev. Lett.* **100**, 013001 (2008).
- [20] Paul, W., Osberghaus, O. & Fischer, E. - *Ein Ionenkäfig*, vol. 415 (Forschungsberichte des Wirtschafts- und Verkehrsministeriums Nordrhein-Westfalen, 1958).
- [21] Paul, W. - Electromagnetic traps for charged and neutral particles. *Rev. Mod. Phys.* **62**, 531–540 (1990).
- [22] Ghosh, P. K. - *Ion traps* (Oxford University Press, 1995).
- [23] Berkeland, D. J., Miller, J. D., Bergquist, J. C., Itano, W. M. & Wineland, D. J. - Minimization of ion micromotion in a paul trap. *Journal of Applied Physics* **83**, 5025–5033 (1998).
- [24] Gulde, S. - *Experimental realization of quantum gates and the Deutsch-Josza algorithm with trapped $^{40}\text{Ca}^+$ ions*. Ph.D. thesis, University of Innsbruck (2003).
- [25] Lucas, D. M. *et al.* - Oxford ion-trap quantum computing project. *Philosophical Transactions of the Royal Society of London A: Mathematical, Physical and Engineering Sciences* **361**, 1401–1408 (2003).
- [26] Jin, J. & Church, D. A. - Precision lifetimes for the Ca^+ $4p^2P$ levels. *Phys. Rev. Lett.* **70**, 3213–3216 (1993).
- [27] James, D. - Quantum dynamics of cold trapped ions with application to quantum computation. *Applied Physics B* **66**, 181–190 (1998).
- [28] Barton, P. A. *et al.* - Measurement of the lifetime of the $3d^2D_{5/2}$ state in $^{40}\text{Ca}^+$. *Phys. Rev. A* **62**, 032503 (2000).

BIBLIOGRAPHY

- [29] Roos, C. F. - *Controlling the quantum state of trapped ions*. Ph.D. thesis, University of Innsbruck (2000).
- [30] Leibfried, D., Blatt, R., Monroe, C. & Wineland, D. - Quantum dynamics of single trapped ions. *Rev. Mod. Phys.* **75**, 281–324 (2003).
- [31] Schmidt-Kaler, F. *et al.* - Ground state cooling, quantum state engineering and study of decoherence of ions in paul traps. *Journal of Modern Optics* **47**, 2573–2582 (2000).
- [32] Wineland, D. J. & Itano, W. M. - Laser cooling of atoms. *Phys. Rev. A* **20**, 1521–1540 (1979).
- [33] Home, J. P. *et al.* - Complete methods set for scalable ion trap quantum information processing. *Science* **325**, 1227 (2009).
- [34] Monroe, C. & Kim, J. - Scaling the ion trap quantum processor. *Science* **339**, 1164–1170 (2013).
- [35] Monz, T. *et al.* - 14-Qubit Entanglement: Creation and Coherence. *Phys. Rev. Lett.* **106**, 130506 (2011).
- [36] Jurcevic, P. *et al.* - Quasiparticle engineering and entanglement propagation in a quantum many-body system. *Nature* **511**, 202–205 (2014).
- [37] Schinarakis, K. Press release Jülich. http://www.fz-juelich.de/SharedDocs/Pressemitteilungen/UK/DE/2010/index7d86_hm.html (2010).
- [38] Kielpinski, D., Monroe, C. & Wineland, D. J. - Architecture for a large-scale ion-trap quantum computer. *Nature* **417**, 709–11 (2002).
- [39] Amini, J. M. *et al.* - Toward scalable ion traps for quantum information processing. *New Journal of Physics* **12**, 033031 (2010).
- [40] Lin, G.-D. *et al.* - Large-scale quantum computation in an anharmonic linear ion trap. *EPL (Europhysics Letters)* **86**, 60004 (2009).
- [41] Islam, R. *et al.* - Emergence and frustration of magnetism with variable-range interactions in a quantum simulator. *Science* **340**, 583–7 (2013).
- [42] Cirac, J. & Zoller, P. - A scalable quantum computer with ions in an array of microtraps. *Nature* **404**, 579–81 (2000).
- [43] Chiaverini, J. & Lybarger, W. - Laserless trapped-ion quantum simulations without spontaneous scattering using microtrap arrays. *Phys. Rev. A* **77**, 022324 (2008).

- [44] Wilson, C. *et al.* - Tunable spin-spin interactions and entanglement of ions in separate potential wells. *Nature* **512**, 57–60 (2014).
- [45] Kumph, M. *et al.* - Operation of a planar-electrode ion trap array with adjustable RF electrodes. *arXiv:1402.0791v1* (2014).
- [46] Monroe, C. *et al.* - Large-scale modular quantum-computer architecture with atomic memory and photonic interconnects. *Phys. Rev. A* **89**, 022317 (2014).
- [47] Chiaverini, J. *et al.* - Surface-electrode architecture for ion trap quantum information processing. *Quantum Inf. Comput.* **5**, 419 (2005).
- [48] Schulz, S., Poschinger, U., Ziesel, F. & Schmidt-Kaler, F. - Sideband cooling and coherent dynamics in a microchip multi-segmented ion trap. *New Journal of Physics* **10**, 045007 (2008).
- [49] Harlander, M., Lechner, R., Brownnutt, M., Blatt, R. & Hänsel, W. - Trapped-ion antennae for the transmission of quantum information. *Nature* **471**, 200–3 (2011).
- [50] Hensinger, W. K. *et al.* - T-junction ion trap array for two-dimensional ion shuttling, storage, and manipulation. *Applied Physics Letters* **88**, 034101 (2006).
- [51] Hughes, M. D., Lekitsch, B., Broersma, J. A. & Hensinger, W. K. - Microfabricated ion traps. *Contemporary Physics* **52**, 505–529 (2011).
- [52] Brama, E., Mortensen, A., Keller, M. & Lange, W. - Heating rates in a thin ion trap for microcavity experiments. *Applied Physics B* **107**, 945–954 (2012).
- [53] Wilpers, G., See, P., Gill, P. & Sinclair, A. G. - A monolithic array of three-dimensional ion traps fabricated with conventional semiconductor technology. *Nature Nanotechnology* **7**, 572–6 (2012).
- [54] Stick, D. *et al.* - Ion trap in a semiconductor chip. *Nature Physics* **2**, 36–39 (2005).
- [55] Blakestad, R. *et al.* - High-Fidelity Transport of Trapped-Ion Qubits through an X-Junction Trap Array. *Phys. Rev. Lett.* **102**, 153002 (2009).
- [56] Ruster, T. *et al.* - Experimental realization of fast ion separation in segmented Paul traps. *arXiv:1405.5046v1* (2014).
- [57] Daniilidis, N. *et al.* - Corrigendum: Fabrication and heating rate study of microscopic surface electrode ion traps. *New Journal of Physics* **14**, 079504 (2012).
- [58] Wang, S. X. *et al.* - Superconducting microfabricated ion traps. *Applied Physics Letters* **97**, 244102 (2010).

BIBLIOGRAPHY

- [59] Britton, J. *et al.* - Scalable arrays of rf Paul traps in degenerate Si. *Applied Physics Letters* **95**, 173102 (2009).
- [60] Allcock, D. T. C. *et al.* - Heating rate and electrode charging measurements in a scalable, microfabricated, surface-electrode ion trap. *Applied Physics B* **107**, 913–919 (2011).
- [61] Doret, S. C. *et al.* - Controlling trapping potentials and stray electric fields in a microfabricated ion trap through design and compensation. *New Journal of Physics* **14**, 073012 (2012).
- [62] Mehta, K. K. *et al.* - Ion traps fabricated in a CMOS foundry. *Applied Physics Letters* **105**, – (2014).
- [63] Moehring, D. L. *et al.* - Design, fabrication and experimental demonstration of junction surface ion traps. *New Journal of Physics* **13**, 075018 (2011).
- [64] Brown, K. R. *et al.* - Coupled quantized mechanical oscillators. *Nature* **471**, 196–9 (2011).
- [65] Pauli, A. - *Classical control of an ion in a surface trap*. Master's thesis, University of Innsbruck (2011).
- [66] Shaikh, F. A. & Ozakin, A. - Stability analysis of ion motion in asymmetric planar ion traps. *Journal of Applied Physics* **112**, 074904 (2012).
- [67] Allcock, D. T. C. *et al.* - Implementation of a symmetric surface-electrode ion trap with field compensation using a modulated Raman effect. *New Journal of Physics* **12**, 053026 (2010).
- [68] Brownnutt, M., Kumph, M., Rabl, P. & Blatt, R. - Ion-trap measurements of electric-field noise near surfaces. *arXiv:1409.6572* (2014).
- [69] Sørensen, A. & Mølmer, K. - Quantum computation with ions in thermal motion. *Phys. Rev. Lett.* **82**, 1971–1974 (1999).
- [70] Benhelm, J., Kirchmair, G., Roos, C. F. & Blatt, R. - Towards fault-tolerant quantum computing with trapped ions. *Nature Physics* **4**, 463–466 (2008).
- [71] Wineland, D. *et al.* - Experimental Primer on the Trapped Ion Quantum Computer. *Fortschritte der Physik* **46**, 363–390 (1998).
- [72] Parrot, M., Inan, U. S., Lehtinen, N. G. & Pinçon, J. L. - Penetration of lightning MF signals to the upper ionosphere over VLF ground-based transmitters. *Journal of Geophysical Research* **114**, A12318 (2009).

- [73] Hansen, D. - Review of EMC main aspects in fast PLC including some history. *IEEE International Symposium on Electromagnetic Compatibility* **1**, 184–192 (2003).
- [74] Fernandez, I. *et al.* - Indoor noise measurements in medium wave band. *Electronics Letters* **46**, 1162 (2010).
- [75] Johnson, J. B. - Thermal agitation of electricity in conductors. *Phys. Rev.* **32**, 97–109 (1928).
- [76] Nyquist, H. - Thermal agitation of electric charge in conductors. *Phys. Rev.* **32**, 110–113 (1928).
- [77] Herring, C. & Nichols, M. H. - Thermionic emission. *Rev. Mod. Phys.* **21**, 185–270 (1949).
- [78] Turchette, Q. A. *et al.* - Heating of trapped ions from the quantum ground state. *Phys. Rev. A* **61**, 063418 (2000).
- [79] Daniilidis, N. *et al.* - Surface noise analysis using a single-ion sensor. *Phys. Rev. B* **89**, 245435 (2014).
- [80] Brown, K. R. *et al.* - Single-qubit-gate error below $10E-4$ in a trapped ion. *Phys. Rev. A* **84**, 030303 (2011).
- [81] Allcock, D. T. C. *et al.* - Reduction of heating rate in a microfabricated ion trap by pulsed-laser cleaning. *New Journal of Physics* **13**, 123023 (2011).
- [82] Lüth, H. - *Surfaces and Interfaces of Solid Materials* (Springer-Verlag, 3rd Edition, 1995).
- [83] Hite, D. A. *et al.* - 100-Fold Reduction of Electric-Field Noise in an Ion Trap Cleaned with In Situ Argon-Ion-Beam Bombardment. *Phys. Rev. Lett.* **109**, 103001 (2012).
- [84] McKay, K. S. *et al.* - Ion-trap electrode preparation with Ne^+ bombardment. *arXiv:1406.1778* (2014).
- [85] Epstein, R. *et al.* - Simplified motional heating rate measurements of trapped ions. *Phys. Rev. A* **76**, 033411 (2007).
- [86] Wesenberg, J. *et al.* - Fluorescence during Doppler cooling of a single trapped atom. *Phys. Rev. A* **76**, 053416 (2007).
- [87] Deslauriers, L. *et al.* - Scaling and Suppression of Anomalous Heating in Ion Traps. *Phys. Rev. Lett.* **97**, 103007 (2006).
- [88] Antohi, P. B. *et al.* - Cryogenic ion trapping systems with surface-electrode traps. *The Review of Scientific Instruments* **80**, 013103 (2009).

BIBLIOGRAPHY

- [89] Gandolfi, D., Niedermayr, M., Kumph, M., Brownutt, M. & Blatt, R. - Compact radio-frequency resonator for cryogenic ion traps. *The Review of Scientific Instruments* **83**, 084705 (2012).
- [90] Vittorini, G., Wright, K., Brown, K. R., Harter, A. W. & Doret, S. C. - Modular cryostat for ion trapping with surface-electrode ion traps. *The Review of Scientific Instruments* **84**, 043112 (2013).
- [91] Alonso, J., Leupold, F. M., Keitch, B. C. & Home, J. P. - Quantum control of the motional states of trapped ions through fast switching of trapping potentials. *New Journal of Physics* **15**, 023001 (2013).
- [92] Chiaverini, J. & Sage, J. M. - Insensitivity of the rate of ion motional heating to trap-electrode material over a large temperature range. *Phys. Rev. A* **89**, 012318 (2014).
- [93] Labaziewicz, J. *et al.* - Temperature Dependence of Electric Field Noise above Gold Surfaces. *Phys. Rev. Lett.* **101**, 180602 (2008).
- [94] Ekin, J. W. - *Experimental Techniques for Low-Temperature Measurements* (Oxford University Press, 2007), 2nd edn.
- [95] Lide, D. R. (ed.) - *CRC Handbook of Chemistry and Physics, 78. Edition* (CRC Press, 1998).
- [96] Nunn, D. Lakeshore Appendix I: Cryogenic Reference Tables. http://www.lakeshore.com/Documents/LSTC_appendixI_1.pdf (2014).
- [97] Tomaru, T. *et al.* - Vibration analysis of cryocoolers. *Cryogenics* **44**, 309–317 (2004).
- [98] Gifford, W. E. & McMahon, H. O. Fluid expansion refrigeration method and apparatus. Patent US 2906101 (1959).
- [99] Masuyama, S., Fukuda, Y., Imazu, T. & Numazawa, T. - Characteristics of a 4K Gifford–McMahon cryocooler using the Gd₂O₂S regenerator material. *Cryogenics* **51**, 337–340 (2011).
- [100] Ikushima, Y. *et al.* - Ultra-low-vibration pulse-tube cryocooler system – cooling capacity and vibration. *Cryogenics* **48**, 406–412 (2008).
- [101] Gulde, S. *et al.* - Simple and efficient photo-ionization loading of ions for precision ion-trapping experiments. *Applied Physics B* **73**, 861–863 (2001).
- [102] Lechner, F. - *Photoionisation of ⁴⁰Ca with a frequency-doubled 422 nm laser and a 377 nm laser diode*. Master’s thesis, University of Innsbruck (2010).

-
- [103] Drever, R. *et al.* - Laser phase and frequency stabilization using an optical resonator. *Applied Physics B* **31**, 97–105 (1983).
- [104] Chwalla, M. - *Precision spectroscopy with $^{40}\text{Ca}^+$ ions in a Paul trap*. Ph.D. thesis, University of Innsbruck (2009).
- [105] Benhelm, J. - *Precision Spectroscopy and Quantum Information Processing with Trapped Calcium Ions*. Ph.D. thesis, University of Innsbruck (2008).
- [106] Schindler, P. - *Frequency synthesis and pulse shaping for quantum information processing with trapped ions*. Master's thesis, University of Innsbruck (2008).
- [107] Pearson, C. *et al.* - Experimental investigation of planar ion traps. *Phys. Rev. A* **73**, 032307 (2006).
- [108] Wesenberg, J. - Electrostatics of surface-electrode ion traps. *Phys. Rev. A* **78**, 063410 (2008).
- [109] Niedermayr, M. *et al.* - Cryogenic surface ion trap based on intrinsic silicon. *New Journal of Physics* **16**, 113068 (2014).
- [110] Motoyoshi, M. - Through-Silicon Via (TSV). *Proceedings of the IEEE* **97**, 43–48 (2009).
- [111] Kim, J. *et al.* - System design for large-scale ion trap quantum information processor. *Quantum Info. Comput.* **5**, 515–537 (2005).
- [112] Kaye, G. W. C. & Laby, T. - *Tables of Physical and Chemical Constants* (Longman, 1995), 16. edn.
- [113] Krupka, J. *et al.* - Measurements of permittivity, dielectric loss tangent, and resistivity of float-zone silicon at microwave frequencies. *Microwave Theory and Techniques, IEEE Transactions* **54**, 3995–4001 (2006).
- [114] Sterling, R. C. *et al.* - Fabrication and operation of a two-dimensional ion-trap lattice on a high-voltage microchip. *Nature Communications* **5**, 3637 (2014).
- [115] True Merrill, J. *et al.* - Demonstration of integrated microscale optics in surface-electrode ion traps. *New Journal of Physics* **13**, 103005 (2011).
- [116] Wright, K. *et al.* - Reliable transport through a microfabricated X-junction surface-electrode ion trap. *New Journal of Physics* **15**, 033004 (2013).
- [117] Laermer, F. & Schilp, A. Method of anisotropically etching silicon. Patent US 5501893 A (1994).

BIBLIOGRAPHY

- [118] Parasuraman, J. *et al.* - Deep reactive ion etching of sub-micrometer trenches with ultra high aspect ratio. *Microelectronic Engineering* **113**, 35–39 (2014).
- [119] Poulsen, G., Miroschnyenko, Y. & Drewsen, M. - Efficient ground-state cooling of an ion in a large room-temperature linear Paul trap with a sub-Hertz heating rate. *Phys. Rev. A* **86**, 051402 (2012).
- [120] Reed, G. T. - *Silicon Photonics: The State of the Art* (Wiley, 2008).
- [121] Shimura, F. - *Semiconductor Silicon Crystal Technology* (Elsevier, 1989).
- [122] Kumph, M., Brownnutt, M. & Blatt, R. - Two-dimensional arrays of radio-frequency ion traps with addressable interactions. *New Journal of Physics* **13**, 073043 (2011).
- [123] Klotzbach, U., Lasagni, A. F. & Panzner, M. - Fabrication and Characterization in the Micro-Nano Range. *Advanced Structured Materials* **10**, 29–47 (2011).
- [124] Streed, E. W., Norton, B. G., Jechow, A., Weinhold, T. J. & Kielpinski, D. - Imaging of Trapped Ions with a Microfabricated Optic for Quantum Information Processing. *Phys. Rev. Lett.* **106**, 010502 (2011).